OPTICAL CHARACTERIZATION OF SAMARIUM-DOPED FLUOROPHOSPHATE GLASS FOR X-RAY DOSIMETRY FOR MICROBEAM RADIATION THERAPY AT THE CANADIAN LIGHT SOURCE

A Thesis Submitted
to the College of Graduate Studies and Research
in Partial Fulfillment of the Requirements
for the Degree of Master of Science
in the Division of Biomedical Engineering
University of Saskatchewan

by

Brian Morrell

Saskatoon, Saskatchewan, Canada

Permission to Use

In presenting this thesis in partial fulfillment of the requirements for a Postgraduate degree from the University of Saskatchewan, it is agreed that the Libraries of this University may make it freely available for inspection. Permission for copying of this thesis in any manner, in whole or in part, for scholarly purposes may be granted by the professors who supervised this thesis work or, in their absence, by the Head of the Division of Biomedical Engineering or the Dean of the College of Graduate Studies and Research at the University of Saskatchewan. Any copying, publication, or use of this thesis, or parts thereof, for financial gain without the written permission of the author is strictly prohibited. Proper recognition shall be given to the author and to the University of Saskatchewan in any scholarly use which may be made of any material in this thesis.

Request for permission to copy or to make any other use of material in this thesis in whole or in part should be addressed to:

Head of the Division of Biomedical Engineering
57 Campus Drive
University of Saskatchewan
Saskatoon, Saskatchewan, Canada
S7N 5A9

Acknowledgments

I extend my sincerest gratitude to my supervisor, Dr. S. O. Kasap for his leadership, patience, and encouragement throughout the course of this research as well as his invaluable assistance in finalizing this thesis. I would also like to thank my co-supervisor Dr. Dean Chapman for all of his support, my mentor Dr. K. Koughia for his guidance, assistance and humour throughout the experimental process, my colleague G. Okada for his experimental assistance and friendship, Dr. G. Belev for all of his help at the Canadian Light Source and equipment fixing wizardry, Dr. R. Sammynaiken for his guidance regarding electron paramagnetic resonance and Dr. A. Edgar and Chris Varoy for preparing the samples. I would also like to thank my parents for their support, encouragement and patience.

Abstract

Microbeam Radiation Therapy (MRT) is an experimental form of radiation treatment which has the potential to improve the treatment of many types of cancer. In MRT, the radiation is applied as a grid by passing the collimated X-ray beam from a synchrotron through a microplane collimator, which is a stack of parallel plates of two materials with dramatically different X-ray transparencies. The peak-to-valley dose ratio (PVDR) is the difference between the dose in the microbeams and the dose delivered between the beams. It is the PVDR that is of biological importance in MRT. Therefore a dosimeter for MRT requires a combination of a large dynamic range for dose response into the kilo-Gray regime, and high spatial resolution on the micron scale. This project characterizes fluorophosphate glasses doped with trivalent samarium ions as a potential valency conversion dosimeter for MRT using the conversion of $Sm^{3+} \rightarrow Sm^{2+}$to measure the delivered dose. Samples irradiated at the Canadian Light Source synchrotron showed X-ray induced conversion that could be optically characterized by changes in the photoluminescence emission spectra to obtain irradiation dose. The conversion efficiency depends almost linearly on the irradiation dose up to $\sim$150 Gy and saturates at doses exceeding $\sim$ 1500 Gy. The conversion shows a strong correlation with an observed increase in absorbance of the glass in the range of 200-750 nm. The absorbance increases with X-ray dose and is related to the formation of phosphorous-oxygen hole centers (POHC) and PO_n electron centers. The presence of these defects within the irradiated glass was determined by examination of the induced optical absorbance and electron paramagnetic resonance (EPR) spectra. The formation of these hole centers along with the conversion of $Sm^{3+} \rightarrow Sm^{2+}$under X-ray irradiation suggests that the X-rays cause the formation of electron-hole pairs in the glass. The electrons are then primarily captured by the Sm^{3+}ions, becoming Sm^{2+}ions, with some of the electrons being captured by PO_n electron centers. The holes are captured by the POHCs. This process can be represented chemically as $Sm^{3+} + e^- \rightarrow Sm^{2+}$and $PO + h^+ \rightarrow POHC$. The stability of the Sm conversion under illumination was examined using photoluminescence spectra and the stability of the

X-ray induced defects was examined via the induced optical absorbance and EPR spectra.

Table of Contents

List of Tables

List of Figures

List of Abbreviations

BM	Bend Magnet
BMIT	Biomedical Imaging and Therapy
CLS	Canadian Light Source
CNS	Central Nervous System
CT	Computed Tomography
EC	Electronic Center
EPR	Electron Paramagnetic Resonance
FNTD	Fluorescent Nuclear Track Detector
FP	Fluorophosphate
HC	Hole Center
ID	Insertion Device
MOSFET	Metal-oxide-semiconductor Field-effect Transistor
MRI	Magnetic Resonance Imaging
MRT	Microbeam Radiation Therapy
NIR	Near Infrared
PO_n	Phosphorous Oxygen Molecular Complex
POHC	Phosphorous-Oxygen Hole Center
RE	Rare-Earth
PVDR	Peak-to-Valley Dose Ratio
PL	Photoluminescence
PMT	Photomultiplier Tube
Sm	Samarium
Sm^{2+}	Divalent Samarium
Sm^{3+}	Trivalent Samarium
SSSC	Saskatchewan Structural Science Center
TL	Thermoluminescence
UV	Ultraviolet
Vis	Visible

1. Introduction

1.1 Objectives

Since they were first characterized at the end of the 19th century, X-rays have found a wide range of applications. These applications include, but are not limited to, astronomy, security, industry, and perhaps most importantly, medicine.

The two primary uses of X-rays in medicine are imaging and radiation therapy to treat cancerous tumours. One very promising technique under development for cancer therapy is known as Microbeam Radiation Therapy (MRT). This technique is based on the irradiation of tumours with microplanar arrays of synchrotron generated X-rays. Parallel X-ray planes, a few microns in width, are generated by placing a collimator in front of the beam. These X-ray planes are uniformly spaced approximately 100 microns apart. This planar irradiation spares normal tissue and preferentially damages tumour tissue.

However dosimetry of MRT is a challenging task because one needs to know the peak-to-valley dose ratio (PVDR). The peak dose must be high enough to cause tumour necrosis while the valley dose must remain below the threshold dose to ensure efficient tissue repair. Due to this large dose gradient over a few microns no detector used in conventional radiotherapy has the spatial resolution and large dynamic range to accurately record the PVDR of the microbeam arrays.

So there is a need to develop a dosimeter for MRT that can measure a high dose with high spatial resolution. The dosimeter should have a high dose rate sensitivity, a large dynamic range, good linearity, should be reusable and economic. The objective

of this research is then to develop a dosimeter based on the conversion of the oxidation state, due to a change in the number of valence electrons, of rare-earth (RE) ions embedded in a glass or glass-ceramic host upon exposure to high energy radiation. In this case the RE conversion is $Sm^{3+} \rightarrow Sm^{2+}$ in a fluorophosphate (FP) glass host exposed to hard X-rays.

After exposure to ionizing radiation the Sm^{3+} doped glass will contain some Sm^{2+} ions which have a different fluorescence spectrum than Sm^{3+}. The intensities of these different emission bands is proportional to the concentration of Sm^{3+} and Sm^{2+} ions which is in turn proportional to the amount or X-rays the sample was exposed to. Thus it is possible to use the relative intensities of these peaks to determine a delivered dose.

The objective of this thesis is to characterize the X-ray induced conversion of $Sm^{3+} \rightarrow Sm^{2+}$ within the FP glass host. This will be accomplished by simultaneously exciting both the Sm^{3+} and Sm^{2+} ions and measuring the fluorescence, which can then be used to quantify the conversion of samarium ions as a function of irradiation time.

The glass samples were irradiated with X-rays at the Canadian Light Source (CLS) using the Biomedical Imaging and Therapy Bend Magnet (BMIT-BM) beamline to best approximate the energy and flux of X-rays that would be used in MRT. Simultaneous measurements of the emission spectra of both ions were performed before and after a variety or irradiation times using a spectrometer. In order to select an excitation source that would be efficient at exciting both the Sm^{3+} and Sm^{2+} ions in this glass the excitation spectrum of each ion was measured.

After a visual inspection of irradiated samples it became apparent that the X-ray irradiation also caused the formation of colour centers within the glass which were causing absorption of light in the visible part of the spectrum. To determine the affect of these colour centers on the measurement of the emission spectra of the samarium ions new samples were ground and polished then irradiated at the CLS for transmittance measurements. From these measurements it was possible to determine the degree with which this optical absorption impacted the measurement

of the samarium fluorescence and to identify the colour centers. Irradiated sample were also examined with an EPR spectrometer to help with the identification of the X-ray induced colour centers since the induced absorbance identification suggested that these defects were paramagnetic.

The photostability of the X-ray induced changes in the glass was also examined to determine if the light source used to measure the samarium conversion caused any permanent changes in the irradiated glass. The effect of that light source and a few others were examined by photobleaching irradiated samples and measuring the PL, optical transmittance, and EPR signal strength to characterize any changes to the X-ray induced effects.

1.2 Overview

In Chapter 2 the literature for microbeam radiation therapy will be reviewed along with an examination of the current detectors that are being tested to measure the peak-to-valley dose ratio. The chapter will also include an examination of the literature that suggests why a valency conversion dosimeter such as the one proposed above could be suitable for measuring large dose and being read with high spatial precision.

Chapter 3 outlines the experimental procedures used in this project. The preparation of the Sm^{3+}doped FP glass samples was performed by our collaborators, Dr. Andy Edgar and Chris Varoy at the School of Chemical and Physical Sciences, Victoria University of Wellington, New Zealand and is described in Section 3.1. The samples were then irradiated with X-rays as described in Section 3.2 after which any changes in the glasses were measured by changes in the photoluminescence (PL) spectrum as outlined in Sections 3.3 and 3.5 and changes in the optical absorption spectrum measured as explained in Section 3.4. Photobleaching experiments, Section 3.7, were performed to test the stability and possible erasure of any changes in the irradiated glass samples. Additionally, irradiated samples were examined using an electron paramagnetic resonance (EPR) spectrometer to help with the characteriza-

tion of any X-ray induced defects in the samples. This process is described in Section 3.6.

The experimental results are discussed in Chapter 4. The PL measurements showing the conversion of $Sm^{3+} \rightarrow Sm^{2+}$after X-ray irradiation are examined in Section 4.1 and the relative strength of the fluorescence peaks of the two oxidation states of samarium are used to create a detailed dose profile curve in Section 4.3 by comparing how the ratio of $Sm^{3+}$and Sm^{2+}changes with X-ray exposure time. The X-ray irradiation resulted in other changes in the glass samples besides the change in oxidation state of Sm. These induced effects are examined and identified as phosphour-oxide hole centers in Section 4.2 using the induced absorbance spectra and EPR spectra of the irradiated samples. The reconversion of $Sm^{2+}$to Sm^{3+}as determined by photoluminescence measurements and the decreased number of hole centers as determined by the strength of the induced absorbance and EPR signal after photobleachingand potential re-usability of the exposed samples after photobleachingis examined in Section 4.4.

Chapter 5 concludes this thesis with summaries of the research results and the conclusions that can be drawn from this work as well as recommendations for possible future works.

2. Background and Review

In his 1986 paper, Wilhelm Conrad Röntgen published the first noninvasive image of what is inside the human body making the world aware of the medical applications of X-rays [1]. The two primary uses of X-rays in medicine are imaging and radiation therapy to treat cancerous tumours [2]. One very promising technique under development for cancer therapy is known as Microbeam Radiation Therapy. This technique is based on the irradiation of tumours with microplanar arrays of synchrotron generated X-rays. Parallel X-ray planes a few microns in width are generated by placing a collimator in front of the beam. These X-ray planes are uniformly spaced approximately 100 microns apart. This planar irradiation spares normal tissue and preferentially damages tumour tissue [3].

Unfortunately, there are currently no suitable dosimeters for microbeam radiation therapy because the technique requires a precise determination of the peak-to-valley dose ratio. For there to be any benefits from this technique the peak dose must be high enough to cause tumour necrosis while the valley dose must remain below the threshold dose to ensure efficient tissue repair. It is this large dose gradient over a few microns that makes MRT dosimetry so challenging. None of the detectors used in conventional radiotherapy have a large enough dynamic range and the necessary spatial resolution to accurately record the PVDR of the microbeam arrays [4] [5].

This chapter will review microbeam radiation therapy and examine some different detectors that have recently been examined for synchrotron based MRT. Next, the literature supporting the possibility of a valency conversion RE doped glass or glass-ceramic for radiation dosimetry will be reviewed.

2.1 Microbeam Radiation Therapy

Traditional radiation therapy of tumours in the central nervous system has a large list of associated problems such as impairment of cognitive abilities including memory and processing speed. These radiation treatments also impair spinal cord growth and neuro-endocrine function along with increasing the risk of epilepsy, motor disorders and the chances of secondary tumours. These dangerous secondary effects are most likely to occur in infants and remain a larger concern in children under the age of seven [6]. To overcome these risks techniques such as intensity modulated radiotherapy and stereotactic radiosurgury have been developed which utilize small radiation fields. These techniques take advantage of the so-called dose-volume effect, which suggests that a smaller radiation field size results in an increase of the ability of healthy tissue to tolerate the radiation [7]. It is this same radiotherapy treatment principle that makes MRT a possible treatment for tumours in the central nervous system (CNS) of children [8] [9].

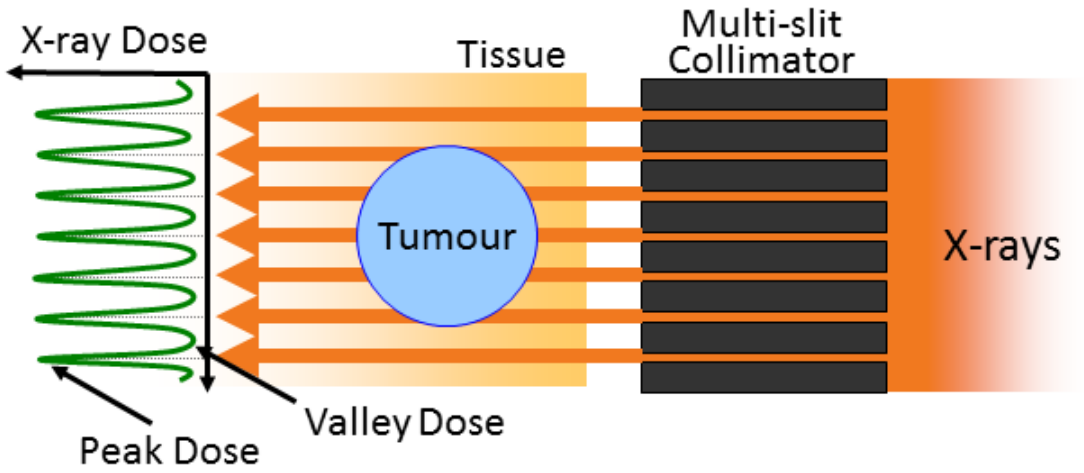

Figure 2.1: A depiction of uni-directional MRT. The X-rays are collimated into thin planes before reaching the target tumour resulting in large peak doses where the X-ray planes pass and lower doses in the valleys between the X-ray planes.

Microbeam radiation therapy was first developed at the National Synchrotron Light Source at Brookhaven National Laboratory [10]. The basic setup for MRT is outlined in Figure 2.1. The X-rays from a synchrotron source with a central energy

in the range of 50-250 keV [4] are passed through a collimator. The collimator for MRT is typically made of parallel stacks of two materials with very different mass attenuation coefficients in the desired energy range. A typical combination is tungsten which strongly absorbs the X-rays resulting in the dose valleys and Kapton which does not interact very much with the X-rays resulting in the dose peaks. An example of a collimator used in MRT experiments at the CLS is shown in Figure 2.2. A collimator for MRT typically produces a planar array of X-rays where the width of the X-ray planes is ∼25-100 μm and the center-to-center spacing between the X-ray planes is ∼100-400 μm [9].

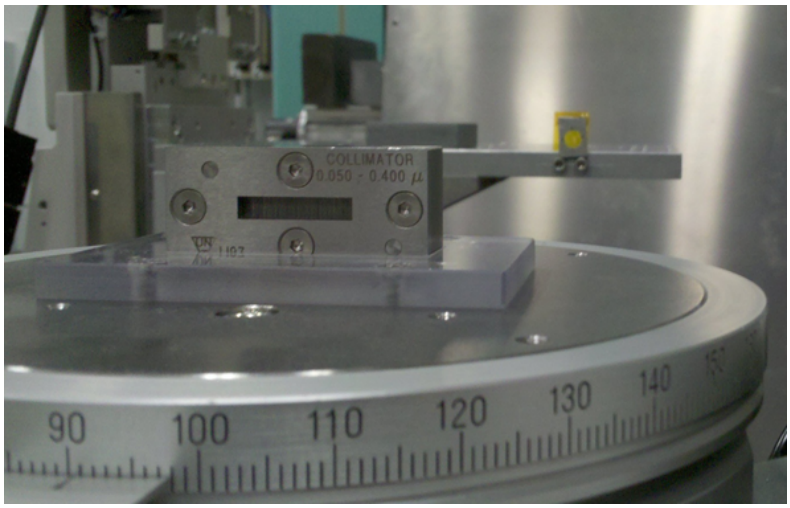

Figure 2.2: A tungsten collimator used for experiments related to MRT at the CLS.

The collimation of the X-rays contributes to the challenge of accurately determining the PVDR. The microbeams from a collimator are not perfectly precise, they have a "tail" that extends into the valley region which could also contribute to the dose in adjacent planes. There are also interactions between the incident X-rays with the materials of the collimator such as Compton scattering and characteristic X-ray emission from the tungsten that along with the propagation of segmented microbeams through the air prior to reaching the target make measurement and simulation of the PVDR challenging [4]. Figure 2.3 is a schematic of a MRT collimator depicting the scattering of X-rays by the collimator.

After passing through the collimator the micro-planar arrays pass through the

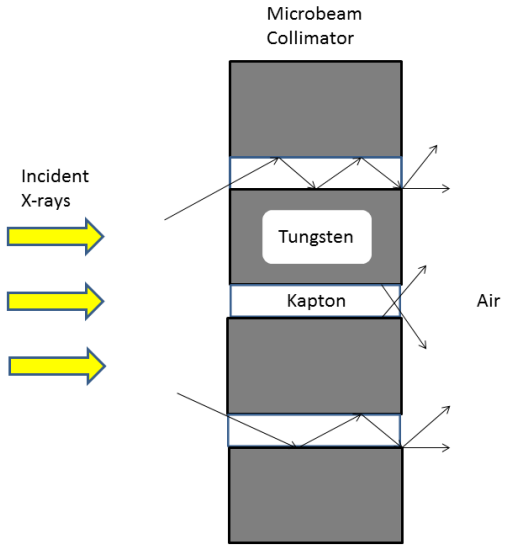

Figure 2.3: A schematic diagram illustrating the potential for the collimator to produce secondary radiation such as scattered photons and characteristic radiation from the tungsten.

tumour and healthy tissue and then on to the dosimeter. While it is not exactly known what peak dose is required for necrosis of the tumour, and it is likely to vary depending on the cell and tissue types being irradiated, experiments suggest the peak dose should be in the range of 800 to several thousand Grays [4] while keeping the valley dose below 20 Gy [11] with a dose rate of approximately 100 Gy/s or higher [12] resulting in a dose gradient of hundreds of Grays over a few microns. The resulting irradiation pattern for a rat cerebellum after MRT with a peak dose of 300 Gy is shown in Figure 2.4.

MRT experiments have been performed on suckling rats and piglets [10] as well as mice and duck embryos [14].The experiments with suckling rats were to examine the dose that can be tolerated without physiological behavioral effects in developing brains. The experiments with piglets was for the establishment of MRT therapy protocols on brains that are equivalent to those of human patients.

Experiments on rats have shown the effectiveness of MRT for treating tumours. The unirradiated controls had a median survival time of 20 days after the tumours

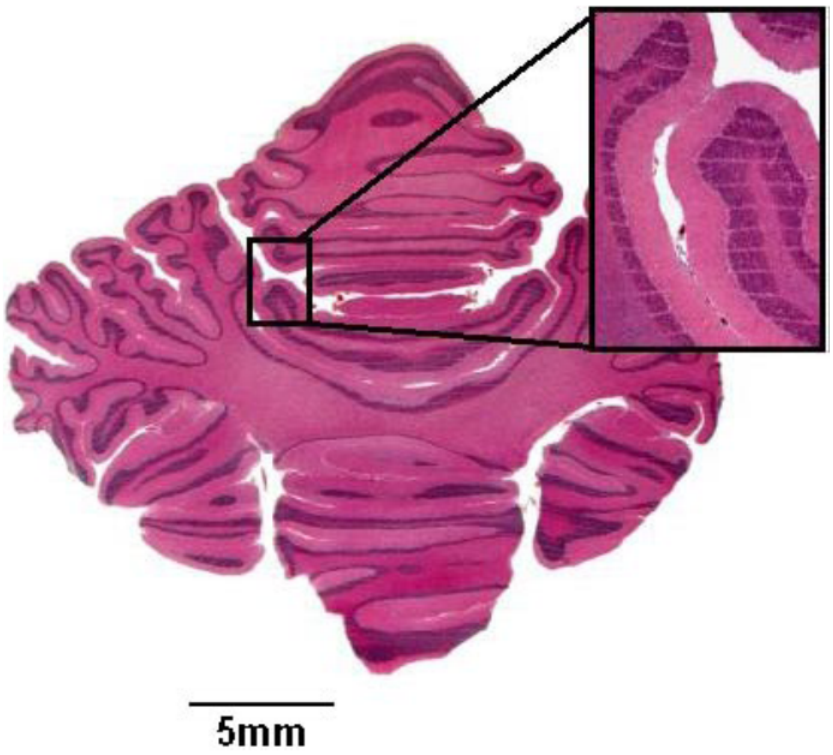

Figure 2.4: A stained tissue section of the cerebellum of a piglet fifteen months after a 300 Gy peak irradiation using MRT. The microbeams were 25 μm wide and were spaced 210 μm apart. The path of the microbeams can be seen as thin white stripes in the insert. After reference [13].

were induced. By comparison, rats that were irradiated with crossed arrays with a peak dose of 625 Gy had a median survival time of 159 days. For single array MRT with the same peak dose the median survival time was 44 days and for crossed arrays with a peak dose of 312 Gy the median survival time was 116 days. Even more promising, after irradiation 22 of the 36 rats tested had their tumours disappear [15].

The above mentioned studies have shown that high dose MRT is effective at destroying tumours while limiting the damage caused to normal tissues. Other studies have examined the cellular processes behind those results. It has been proposed that the sparing effect of MRT on normal tissues is the result of two phenomena [14]:

1. The volume effect which is a principle that states that the threshold dose for radiation damage to tissue increases as the irradiation volume decreases. For

segmented microbeams it is an inverse relationship between the dose tolerance and irradiation volume, for example if the irradiation volume is only 1/4 of the tissue volume then it takes four times the dose to cause the same tissue damage.

2. The biological repair effect is a mechanism that only occurs when the irradiation volume is very small. Although not completely understood the indication is that the irradiated tissues microvasculature is regenerated from angiogenic cells surviving between the microbeams. Figure 2.5 shows undamaged capillary blood vessels crossing the microbeam irradiation tracks in a rat cerebellum sixteen days after the exposure.

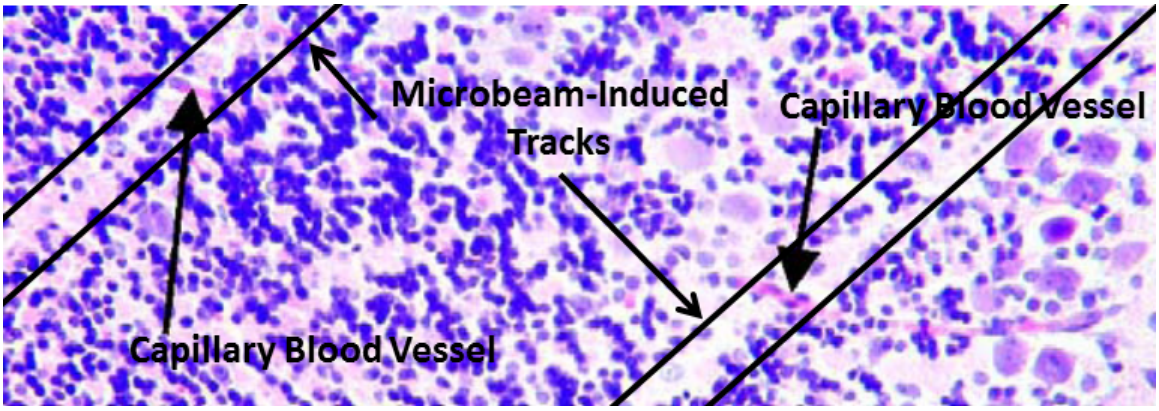

Figure 2.5: A magnified (200x) picture of a rat's cerebellum sixteen days after MRT. The tissue was stained with hematoxylin to image the neurons (purple). The white tracks outlined in the picture show the path of the X-ray bands where they damaged neurons. Also shown in the figure are two capillary blood vessels that appear undamaged despite crossing the area irradiated by the microbeams. Adapted from [16].

Crosbie *et al.* [17] have examined the different cellular response between tumour and normal tissue cells after MRT using immunohistochemsitry techniques. They found that normal tissue seems to effectively repair itself and replace damaged cells and that tumour cells were not able to repair. In fact, 24 hours after irradiation the tumour cells show extensive migration. Even after three days the peak irradiated normal tissue showed minimal evidence of migration. It has been suggested that this rapid intermixing of lethally irradiated cells with undamaged cells inside the tumour may explain the effectiveness of MRT even though only a small proportion of the tumour cells are irradiated.

2.2 Potential Dosimeters for MRT

The large differences in peak and valley doses along with the micrometer beam thickness for MRT make accurate dosimetry very challenging , accurate PVDR can not be measured with traditional dosimeters or easily modeled with Monte Carlo methods. This section will examine some of the attempts to measure the PVDR for MRT.

Ionization Chamber

Ionization chambers are gas filled chambers with two electrodes. The X-rays ionize the gas and the charged particles move towards the plates of the opposite polarity creating a measurable current. A properly calibrated ion chamber can be used to determine dose rates with very good precision, however there is no way to use an ion chamber by itself to determine the valley dose. MRT experiments involving ion chambers have been involved using two independent systems for dose measurement: ionization chambers for the peak dose and radiochromic film for the valley dose [18].

Radiochromic Film Dosimetry

Radiochromic film uses colour changes to indicate radiation dose. They colour directly upon exposure to ionizing radiation and do not require any chemical or thermal processing and are stable at room temperature and under standard lighting. The most common radiochromic film used in MRT experiments are those manufactured by ISP Technologies such as HD-810, MD-55, and EBT. HD-810 and MD-55 films are colourless before irradiation. They consist of a microcrystalline monomeric dispersion coating on a flexible polyester film base. These films turn progressively blue with exposure to ionization radiation due to the formation of two absorption bands centered around 610 and 670 nm. It is the degree of this absorption that is used to determine absorbed dose. The HD-810 film has a range of 50-2500 Gy and the MD-55 film has a range of 3-100 Gy [19]. These films have been reported to have a spatial resolution as high as 0.8 microns [20]. Figure 2.6 shows pieces of HD-810 film irradiated with a

broad beam and with a MRT collimator.

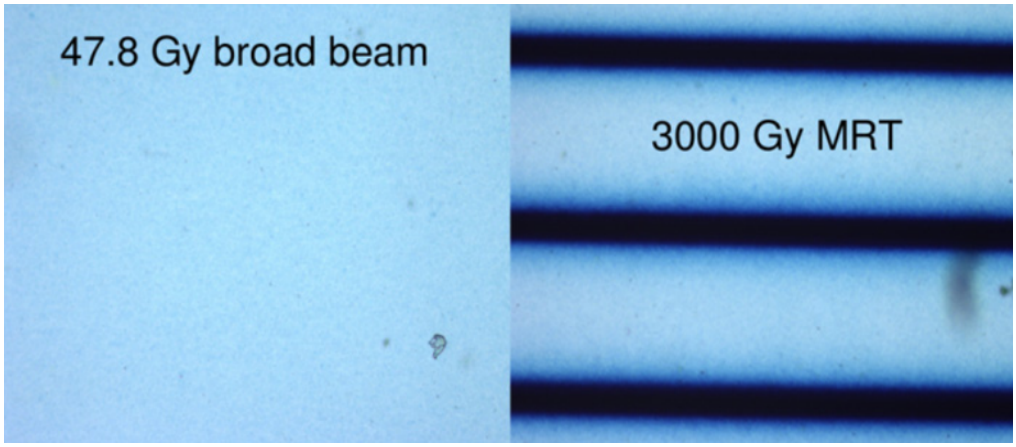

Figure 2.6: Left: HD-810 film exposed to broad beam radiation for a total dose of 47.8 Gy. Right: HD-810 film irradiated through a microbeam collimator with a peak dose of 3000 Gy. The change in optical density, which is proportional to dose, in the valley region of the microbeam irradiated film is comparable to the change in optical density of the broad beam irradiated film. After reference [4].

Used individually none of the radiochromic films has the desired range for efficiently measuring both the peak and valley doses. To overcome this, experiments have been performed irradiating parallel sheets of radiochromic films with different sensitivities. The idea being that a film like HD-810 would record the peak doses and a higher sensitivity film such as MD-55 or EBT would record the valley doses [4]. Using a microscope or a microdensitometer it is possible to read the films with sufficient resolution however there remains concerns about how well the observed optical density reflects the absorbed dose [20].

Flash Memory MOSFET

A metal-oxide-semiconductor field-effect transistor (MOSFET) is used in the switching and amplification of electronic signals. A flash memory MOSFET is a device where a polysilicon layer floating gate is interposed between the control gate and the substrate. The threshold voltage of a MOSFET can be changed allowing the permanent storage of a bit of information. If the device is then exposed to ionizing radiation a charge will be lost from the programmed floating gate which will induce a voltage

change that can be interpreted as dose information. Such a device is capable of producing submicron spatial resolution. However absolute dosimetry information would only be attainable after energy calibration and corrections would have to be made to account for the energy shift from the different spectra in the peak and valley regions. An additional problem with a MOSFET dosimeter is they provide only digital information to the user in the form of logic "0" and "1" which means that current user modes for commercial devices can not be easily adapted for use in MRT [5].

Magnetic Resonance Imaging Gel Dosimetry

The basis for polymer gel dosimetry is the polymerization of monomers dissolved in a gel matrix by free radicals produced by exposing water molecules to ionizing radiation. This results in the immobilization of the monomers and water molecules because of interactions with the interlaced polymer structure. The immobilization causes a change in the autocorrelation time for motion which causes the transverse relaxation time T_2 in Magnetic Resonance to be reduced because there is less averaging of the dipolar magnetic interactions of the 1H-nuclear magnetic moment. The T_2 parameter can then be quantitatively mapped with Multi-Slice-Parameter selective magnetic resonance imaging in three dimensions. Experiments have shown that T_2 increases linearly with dose for a limited dose range for several types of polymer gels however at high dose rates and high dose levels a saturation regime is quickly achieved resulting in a decrease in sensitivity to radiation. Attempts to use MRI gel dosimetry for MRT have yielded poor results for both spatial resolution and dose response [5].

Fluorescent Nuclear Track Detector

Fluorescent nuclear track detectors (FNTD) are a luminescent detector made of fluorescent aluminum oxide single crystals doped with magnesium and carbon. They were originally designed for neutron and heavy particle dosimetry but have been shown to have a linear response to X-rays and gamma rays up to 30 Gy and do not saturate until $\sim$100 Gy. FNTDs use a non-destructive intra-center luminescence

transition that is read with high resolution using an imaging system based on confocal laser scanning fluorescence microscopy technique since the fluorescence intensity response changes with absorbed dose. The FNTD is a passive detector that does not require batteries, wires or electronics during irradiation which makes it easy to use and position. The detectors are cheap, are not sensitive to room lights and are thermally stable up to 600°C meaning that a FNTD could serve as a legal record of dose for a patient file or can be reused after thermal annealing or photobleaching [21].

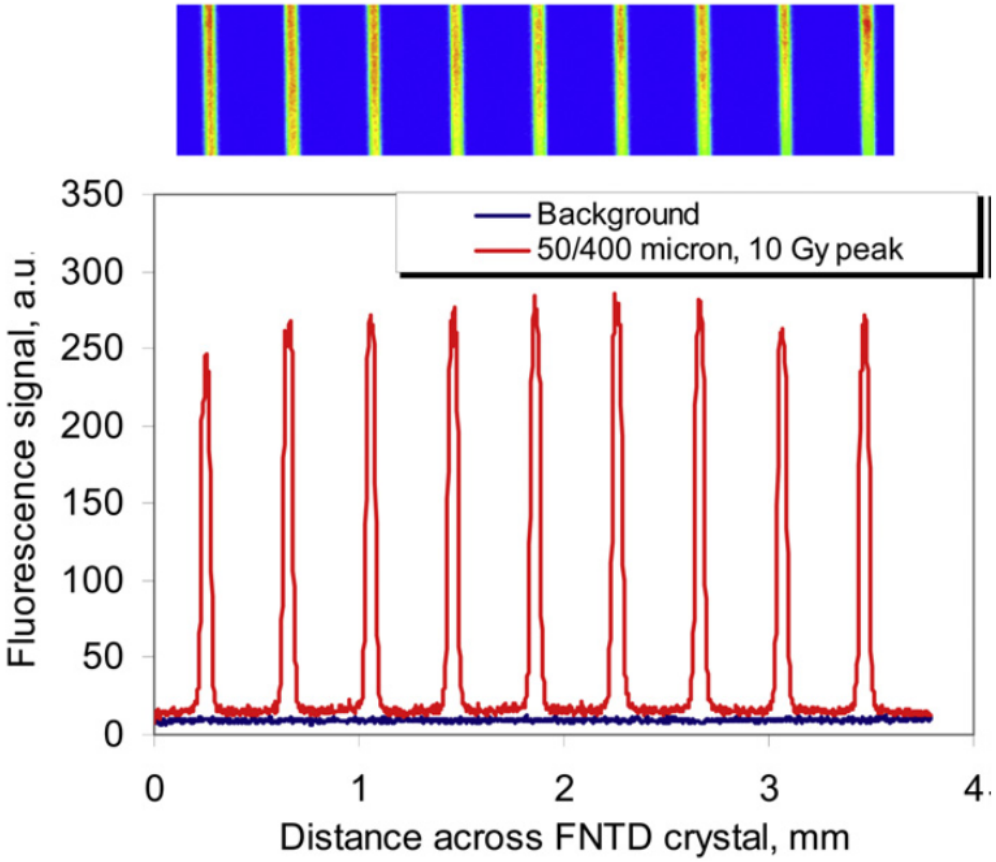

Figure 2.7: Top: Image of a FNTD irradiated with synchrotron generated microbeams. The detector was exposed to a peak dose of 10 Gy and the microbeams were 50 μm wide and had a center-to-center spacing of 400 μm. Below: The cross-section read out of the FNTD read using a laser scanning confocal fluorescent imager in 2D translation mode. After reference [21].

Experiments for MRT were performed with plates that had a dose range from 5 mGy to 50 Gy which is not a large enough dynamic range for MRT. Using a confocal microscope imaging system to read the detector the spatial resolution was observed to

be 0.6 microns. The FNTDs were also shown to be effective at dose rates as high as 10^8 Gy/s. The PVDR was measured to be in between 20 and 100 depending on the width of the microbeams, the center-to-center beam spacing and the depth of the detectors placement in the phantom [5]. Figure 2.7 shows an image of a FNTD irradiated with synchrotron microbeams and the read out of a confocal fluorescent laser scanning imager in two dimensions for a peak dose of 10 Gy depicting an excellent PVDR.

Optical Computed Tomography with PRESAGE^{TM} Radiochromic Plastic

Optical computed tomography operates on the same principle as conventional X-ray CT commonly used in hospitals for medical imaging applications. For three dimensional dose mapping a piece of radiochromic plastic named PRESAGE^{TM} is used. The plastic is initially a light yellow/green in colour and changes locally to a dark green when exposed to ionizing radiation. The extent of this colour change which is determined by the change in optical density is proportional to the absorbed dose meaning that the block of radiochromic plastic is like a three dimensional film like those discussed above. This three dimensional "film" is read using an optical CT scanner.

Experiments for MRT dosimetry have shown that the PRESAGE plastic has a dose range from $\sim$10 Gy to several hundred Grays. Within this dose range the response appeared to remain linear. The spatial resolution was only 20 microns which is good enough to resolve 50 micron microbeams but would not provide a precise measurement of the dose gradient between the peak and valley dose. It was also demonstrated that the measured response was not stable in time meaning that it would be necessary to create a dose response calibration sample at the desired time of radiotherapy [5].

Silicon Strip Detector Dosimetry

Silicon diodes are well established as dosimeters for conventional radiotherapy however the high dose gradients and micron size of the beams mean that conventional silicon detectors are not feasible for MRT. To overcome these limitations a silicon

single strip detector with associated electronics have been tested at the European Synchrotron Radiation Facility. This strip detector measures instantaneous dose rates at the detectors position which can then be integrated to make an estimate of the total absorbed dose.

The spatial resolution is the width of a silicon strip, which is currently 10 microns. The dynamic range covers five orders of magnitude which is sufficient for MRT. The problem of energy dependence mentioned in the above section on flash memory MOSFETs is reduced by the small dimensions of the strips but still needs to be considered, because compared to water, silicon has a strong energy dependence for X-rays below 100 keV.

The other improvement of the silicon strip detectors is that it can be scanned very quickly across an array of microbeams up to 5 cm wide. The new detector could also be used to perform on-line readout of the lateral microbeam profiles at a very high speed with good accuracy. These improvements mean that the strips could be used for fast quality control measurements of the microbeams just prior to a patient's treatment which is a task that no other detector is currently capable of performing. However there are still problems with calibrating the detector to accurately measure absolute dose [5].

High Resolution Optical Calorimetry

Optical calorimetry is based on previous work in holographic interferometry. This method uses the changes in the refractive index of water to measure changes in temperature which are directly related to absorbed dose. Just about all radiation that is incident on an absorbing medium is converted to heat which means that a calorimetric method could be used to determine the energy distribution of the beam based on the temperature increase of the medium after exposure. The induced temperature distribution will only remain indicative of the absorbed dose distribution for a few milliseconds before thermal dissipation makes the original distribution unreadable. This means that both the irradiation time and the measurement time must be

shorter than the thermal relaxation time.

The measurement is made using an interferometer: a beam splitter divides a laser into a reference and object beam, the object beam travels through the medium twice and is recombined with the reference beam to create a hologram. This hologram provides an interference pattern generated by the wavefronts of the object beam passing through the medium before and after irradiation. The interference fringes then correspond to the dose distribution.

Another calorimetric technique for measuring dose distributions is reference image topography. This technique uses the measurement of the apparent motion of a reference object to obtain the time resolved measurements of the topography of a free liquid surface. The object for these experiments was a speckle pattern projected through the calorimeter. The apparent motion of this pattern was then measured before, during, and after irradiation. The degree of apparent motion is directly related to the spectral rate of change of the refractive index which can then be integrated to determine the refractive index. In theory this refractive index data can then be used to determine the absorbed dose.

The limiting factors for these optical calorimetric techniques is the thermal diffusion. There is an finite amount of time required for the microbeams to produce a measurable change in the refractive index and there is a finite amount of time required to measure the heat distribution. During this time the heat distribution and hence the measured dose distribution is changing because of thermal diffusion [22].

Thermoluminescence Optical Fibers

It has long been established that commercially produced communication optical fibers produce usable intensities of thermoluminescence (TL) when exposed to radiation doses of similar magnitudes to those delivered in medical procedures such as radiotherapy. This response is dependent on the presence of structural defects in the material. The ionizing radiation causes the formation of these defects which in turn

emit visible light when the sample is heated. The intensity of this emitted light is proportional to the number of defects in the material which is proportional to the irradiation exposure. Experiments with optical fibers have shown a linear relation between the dose and the TL intensity over a range from 1 Gy- 2 kGy which is an acceptable range for MRT. The advantage of using these optical fibers over traditional TL-detectors is that the fibers have a small diameter, often around 125 microns, which means that they offer better spatial resolution, but the spatial resolution is still not sufficient for MRT. These fibers have also been shown to be impervious to water which means that they could be easily used for measurements inside a phantom for determining dose delivered to a tumour at a certain depth inside a patient [23].

2.3 Rare-Earth Doped Glass and Glass-Ceramics

Another possible approach to developing a detector for MRT is a chemical conversion dosimeter utilizing the valence conversion of RE-ions embedded in a suitable host material. X-ray storage phosphors of this sort have been used in medical imaging since 1980s. They provide several advantages to conventional film-screen systems including having a higher sensitivity, a lower energy dependence, and a larger dynamic range, both of which are desirable properties for a dosimeter for MRT [24]. The best known RE X-ray phosphor is $BaF(Br_x, I_{1-x}):Eu^{2+}$. This phosphor is read by photoluminescence techniques. Some disadvantages of current X-ray phosphors is that they are not stable under ambient light, fade over time because of spontaneous recombination of electron-hole pairs and have a limited signal to noise ratio [25].

Recently work has been performed towards developing effective glass and glass-ceramic phosphors using samarium instead of europium [26]. One of the primary reasons for the shift from europium to Sm is that the PL emission from Sm is in the red region which is well matched to current silicon based detector while europium emits in the blue region of the optical spectrum which is better matched to the more difficult to use photomultiplier tube [27] [28] [29]. Another reason that Sm-ions are a desirable choice for a valency conversion dosimeter is the unique emission spectra for

Table 2.1: The atomic transitions and emission peaks for Sm^{3+}(averaged from [31] [32]) and Sm^{2+}(averaged from [33] [34]) ions embedded in a glass host.

Sm^{3+}		Sm^{2+}	
Transition	Peak (nm)	Transition	Peak (nm)
$^4G_{5/2} \rightarrow {}^6H_{5/2}$	567	$^5D_0 \rightarrow {}^7F_0$	682
$^4G_{5/2} \rightarrow {}^6H_{7/2}$	603	$^5D_0 \rightarrow {}^7F_1$	699
$^4G_{5/2} \rightarrow {}^6H_{9/2}$	650	$^5D_0 \rightarrow {}^7F_2$	725

$Sm^{3+}$and Sm^{2+}. The electronic transitions that characterize the PL spectra of these ions and the position of corresponding emission peaks are listed in Table 2.1. As shown in the table, $Sm^{3+}$and Sm^{2+}have distinct emission peaks that are close enough together to be read simultaneously with a silicon based spectrometer but far enough apart that even in a spectra of mixed emission from both $Sm^{3+}$and $Sm^{2+}$the peaks from ions remain easily identifiable. The average lifetime for the $^5D_0 \rightarrow {}^7F_0$ transition in a borate glass host was 1.6 ms at room temperature [30], which is acceptable for quick PL measurements.

To use Sm-doped glasses or glass-ceramics as an X-ray dosimeter medium there must be conversion from $Sm^{3+} \rightarrow Sm^{2+}$after exposure to X-rays. Sm-doped glass-ceramics and powders have been shown to convert much more readily than many similar Sm-doped glass compositions [11] [35]. However a pure glass sample is preferable to the crystals in a glass-ceramic since the glass allows for higher doping levels, the geometry of the ion sites is more flexible, scatter fluorescent light less, and glasses are better for the fabrication of large flat plates or drawing into fibers [36].

Experiments have been performed showing conversion of $Sm^{3+} \rightarrow Sm^{2+}$in: a borate glass ($Li_2O-SrO-B_2O_3$) after X-ray irradiation [30], a sodium barium strontium phosphate glass after X-ray irradiation [37], a sodium borate glass after irradiation with a femtosecond pulsed laser at 800 nm [38], an aluminoborosilicate glass after β-irradiation [39], and an $Al_2O_3-SiO_2$ glass after X-ray irradiation [40]. The PL spectra of Sm^{3+}in an $Al_2O_3-SiO_2$ glass and the mixed PL spectra of $Sm^{3+}$and Sm^{2+}after X-ray irradiation is shown in Figure 2.8. The relative proportion of the Sm^{2+}ions in the

glass is a function of irradiation dose [39].

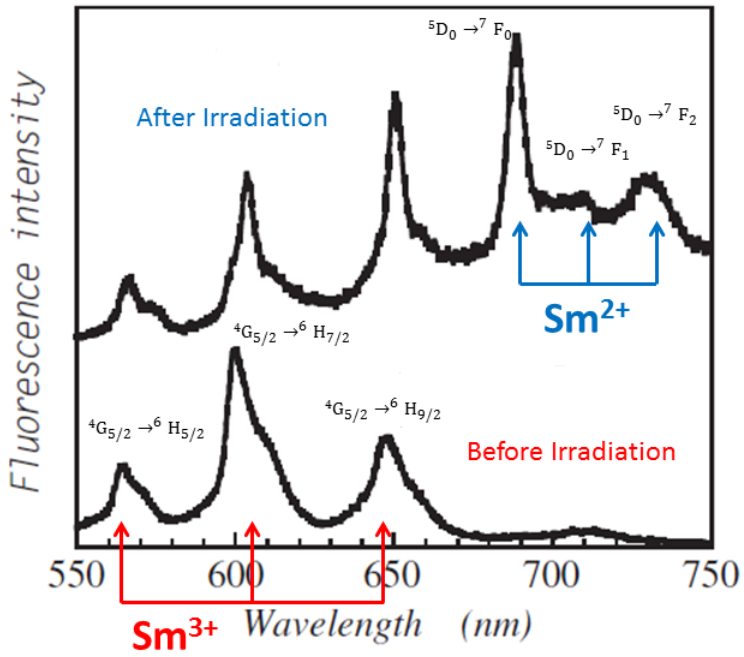

Figure 2.8: The PL spectra before and after a 14 hour X-ray irradiation for a Sm-doped irradiation for a Al_2O_3-SiO_2 glass showing the conversion of $Sm^{3+} \rightarrow Sm^{2+}$. The atomic transitions that give rise to each peak are also labeled. Adapted from [41].

It should also be noted that experiments using the valence conversion of irradiated Sm-doped glass as a possible material for three dimensional optical data storage devices have shown that it is possible to read converted areas or "bits" with a submicron precision. In these experiments $Sm^{3+}$was photo-reduced to Sm^{2+}using a femtosecond pulsed laser operating at 800 nm. The laser produced converted areas or bit sizes of 1 micron with a layer separation of 8 microns. The bits were read by using a reflection-type fluorescent confocal microscope that was set to detect the 682 nm emission peak of Sm^{2+} [38] [42]. Figure 2.9 shows a fluorescent image of the photo-reduced Sm^{2+}bits in a sodium borate glass along with a spatial readout of the fluorescent signal showing micron scale resolution which would be sufficient for MRT.

There has also been work recently towards developing a confocal laser microscope system specifically for the purpose of measuring the detailed dose distribution pattern associated with irradiation with microbeams in typical glass dosimeters. Testing of

this system with silver activated phosphate glass irradiated with alpha particles has shown that it is possible to use the radiophotoluminescence signal to achieve a spatial resolution of ∼3 mm. The sensitivity of the system was high enough that a resolvable signal was achievable after exposure to only five alpha particles in a unit area [43]. Figure 2.9 shows a schematic of a fluorescent confocal microscope.

Another interesting property of the $Sm^{3+} \rightarrow Sm^{2+}$conversion in glass is that the reduction can be reversed by exposing the converted glass to intense illumination in the blue and UV range of the spectrum, such as a 488 nm argon laser. This photobleaching quickly re-converts the Sm^{2+}back into $Sm^{3+}$to the point that there is no longer any sign of Sm^{2+}emission peaks in the PL spectra [44]. It has also been shown that after this sort of erasure the materials are still sensitive to X-ray irradiation [45] and $Sm^{3+} \rightarrow Sm^{2+}$conversion is still observed in glass that has been irradiated, bleached, and irradiated again [42]. Figure 2.10 demonstrates the photobleaching and re-conversion of Sm^{2+}bits produced by a femtosecond pulsed laser and bleached with a 488 nm argon laser. The ability to photobleach the Sm-doped glasses means that it could be possible to produce a reusable and therefore more economic Sm-doped glass dosimeter for MRT.

For this project, the glass to be doped with samarium is a fluorophosphate glass [46] [47]. The affect of X-ray irradiation on phosphate and fluorophosphate glasses has been studied using transmission experiments and electron paramagnetic resonance spectra to identify radiation induced effects in the glass. It has been found that the X-ray radiation produces electron-hole pairs in the glass which are then captured by electron and hole traps within the glass creating optical absorption bands and paramagnetic centers [48] [49] [50] [51]. Trivalent samarium ions, much like trivalent europium ions, are an electron trap and should suppress the development of induced absorption bands associated with electronic colour centers [52]. The end result then being the conversion of $Sm^{3+} \rightarrow Sm^{2+}$which can then be used to determine the absorbed radiation dose with high spatial resolution [53].

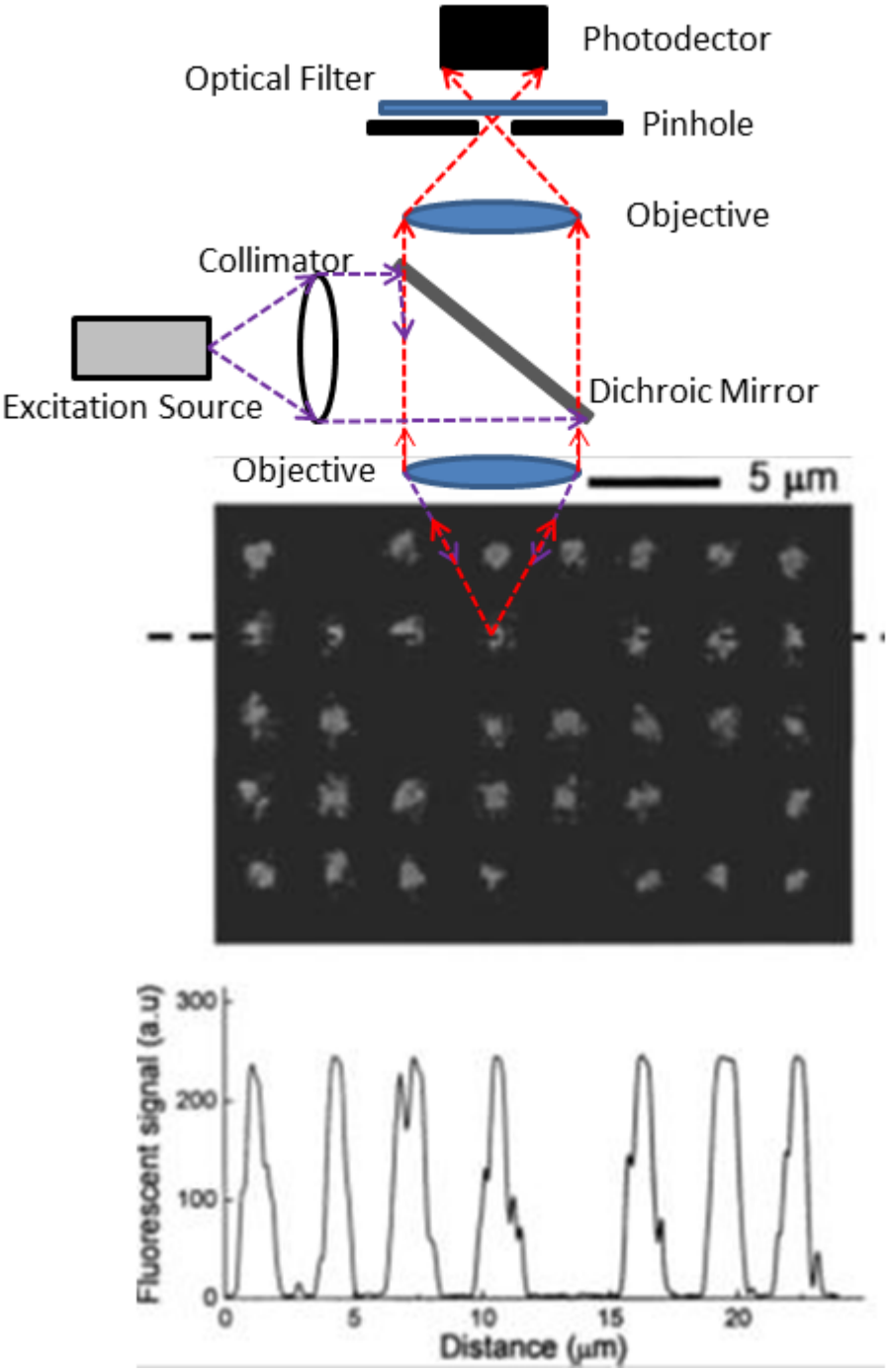

Figure 2.9: Top: A schematic of a fluorescent confocal microscope. Middle: Fluorescent image of the pattern formed in a Sm^{3+}-doped sodium borate glass using a femto-second pulsed laser. Bottom: The signal profile measured along the dashed line for the fluorescent signal at 682 nm which is a Sm^{2+}peak. Note the spatial scale of the profile is in microns. Adapted from [38].

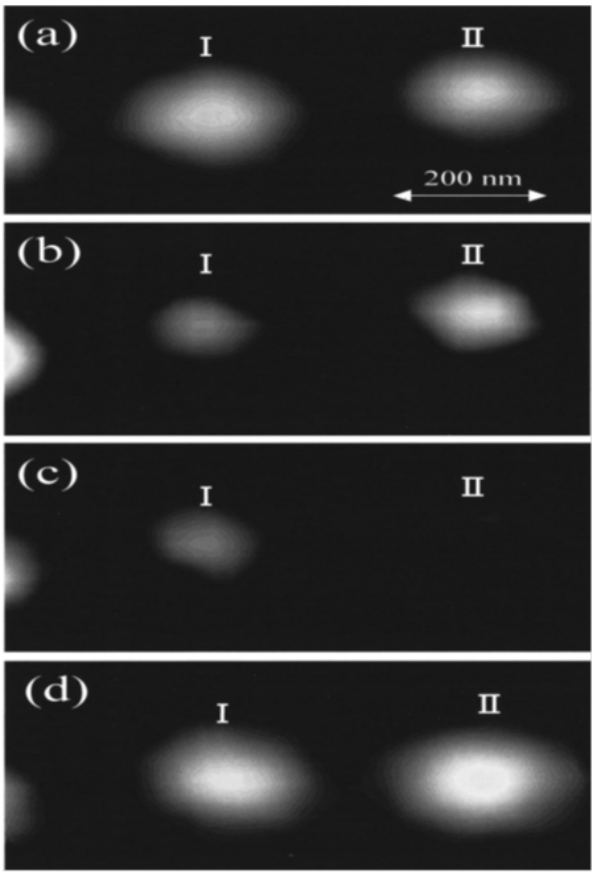

Figure 2.10: Photoluminescence images of Sm^{3+}-doped glass demonstrating erasure and reconversion of $Sm^{3+} \rightarrow Sm^{2+}$. The conversion was performed with a femto-second IR laser and the erasure was performed with a 10 mW Ar^{+} laser operating at 514.5 nm. (a) Image after conversion, before erasure. (b) Image after photoreduction of bit I using laser irradiation. (c) Image after photorduction of bit II by laser irradiation. (d) Image after femto-second laser irradiation to the areas where bit I and II were. After reference [42].

3. Experimental Procedure

This chapter discusses the general experimental setups and procedures involved in this research. The first section outlines the preparation of the glass samples. The following sections then deal with the X-ray irradiation of the samples (Section 3.2) and then the photoluminescence emission at low temperature and the excitation spectra are examined in Section 3.3. Th optical measurements used to identify X-ray induced defects are covered in Section 3.4. Then the stability of these defects under photobleaching is tested as described in Section 3.5. The experiments to develop an actual dose profile curve from our samples are outlined in Section 3.6 and Section 3.7 describes EPR experiments performed to help explain the optical measurements.

3.1 Sample Preparation

The objective of this project was to determine whether a valence conversion dosimeter for MRT could be developed utilizing the valence change in Sm ions doped in a fluorophosphate glass host under X-ray irradiation. This section briefly outlines the preparation of the samples used in the experiments.

The glasses were based on literature references [46] [47]. All samples were prepared by Dr. Andy Edgar and Chris Varoy from a collaborating research group at the School of Chemical and Physical Sciences, Victoria University of Wellington, New Zealand. There were three different compositions of fluorophosphate glass used in this project with Sm concentrations ranging from 0.001% to 0.5%.

The first FP glass is composed of 10.0%MgF_2, (34.400 -x)%AlF_3, 30.4%CaF_2, 15.2%SrF_2, 10.0%$Sr(PO_3)_2$, and x%SmF_3 by molar percentage. The strontium metaphos-

phate was prepared prior to batching the glass from strontium carbonate and ammonium dihydrogen phosphate. The batches were melted in a Pt-Rh10% lidded crucible at 1050°C for one hour under a "dry, oxygen free" argon flow. The melt is lowered to 1000°C for one hour and then poured in a "dry, oxygen free" N_2 atmosphere onto quench plates at 350°C for two hours. After which the samples are cooled to 300°C at -10°/hr and then to 20°C at -20°C/hr.

The second FP glass is composed of 10.0%MgF_2, (34.400 -x)%AlF_3, 30.4%CaF_2, 15.2%SrF_2, 10.0%$Ba(PO_3)_2$, and x%SmF_3 by molar percentage. The barium metaphosphate was prepared prior to batching the glass from barium carbonate and ammonium dihydrogen phosphate. Otherwise the melting and quenching procedure is the same as for the above composition.

The third FP glass composition was 10.0%MgF_2, (27.9333 -x)%AlF_3, 30.4%CaF_2, 25.0%SrF_2, 6.6666%$Al(PO_3)_3$, and x%SmF_3 by molar percentage. The batches were melted in a Pt-Rh10% lidded crucible at 1050°C for one hour under a "dry, oxygen free" argon flow. The melt is lowered to 1000°C for one hour and then poured in a "dry, oxygen free" N_2 atmosphere onto quench plates at 430°C for two hours. After which the samples are cooled to 400°C at -10°/hr and then to 20°C at -20°C/hr.

Ehrt and Töpfer have reported that fluorophosphate glass with a similar composition to these glasses, with $x = 0$, has a density of 3.60 g/cm^3 [54].

3.2 X-Ray Irradiation

The samples were irradiated using two different x-ray sources. A Faxitron X-ray cabinet was used to irradiate samples for EPR and photobleachingexperiments while the Biomedical Imaging and Therapy bend magnet beamline at the Canadian Light Source was used to irradiate the samples used for the dose profile experiments.

3.2.1 Faxitron X-Ray Cabinet

For some experiments not directly related to dose profile experiments the samples were irradiated in-lab due to the limited availability of shifts at the synchrotron. The X-ray source used for these irradiations was a Faxitron cabinet X-ray system, model 43855D. This model has a tungsten anode and operates at a maximum tube voltage of 110 kVp at approximately 3 mA tube current. A calculation of the energy spectrum of the X-rays from this source can be seen in Figure 3.1. The system has a timer that can be manually set for exposures ranging from 1 second to 1 hour. For irradiation, the samples were placed on an aluminum rod that is used to raise the samples up close to the aperture through which the X-rays enter the chamber to maximize exposure as shown in Figure 3.2. No filters were used for any exposures.

The warm-up procedure that was followed before the first operation of the day is as follows:

1. Turn the key to activate the system
2. With the tube voltage set at zero set the exposure time to 5 minutes
3. Start exposure and turn tube voltage up to 30 kVp
4. After exposure turn tube voltage back down to zero
5. Start a new 5 min exposure and turn the tube voltage up to 60 kVp
6. After exposure turn tube voltage back down to zero
7. Start another 5 min exposure and turn the tube voltage up to 90 kVp

8. After exposure turn the tube voltage back to zero.

The chamber is then ready for operation.

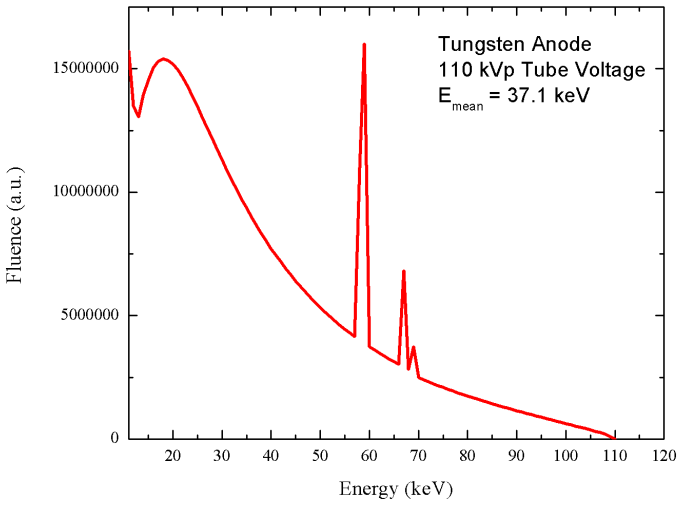

Figure 3.1: The calculated Bremsstrahlung X-rays and characteristic peaks for a tungsten anode X-ray tube operated at 110 kVp with no added filters. The spectrum was calculated with [55] [56] [57] using values from [58].

(a) (b)

Figure 3.2: (a) The Faxitron cabinet X-ray system unit model 43855D used to irradiated some of the samples for this project. (b) An interior picture of the chamber showing the aluminum rod and clamp used to position the sample close to the X-ray tube.

3.2.2 Canadian Light Source

The X-ray irradiation of samples for dose profile curves took place at the Canadian Light Source, a third generation synchrotron facility located in Saskatoon, Canada. The beamline used was the Biomedical Imaging and Therapy Bend Magnet Beamline, BMIT-05BM. The CLS operates at 2.9 GeV energy and is designed to have a ring current of 500 mA, however at the time of these experiments the maximum ring current was 250 mA. The bend magnet has a magnetic field of 1.354 T resulting in critical or central energy of 7.57 keV and the photon brightness is 1.5×10^{11} ph s^{-1} mr^{-2} mA^{-1} $(0.1\%\text{bandwidth})^{-1}$ at 10 keV. The largest beam dimensions are 240 mm in the horizontal and 7 mm in the vertical at 23 m from the source [59] [60] [61].

In order to perform experiments with an X-ray beam of similar energy to the X-rays used for MRT three copper filters of thickness 0.110, 0.276, and 0.552 mm for a total of 0.938 mm were placed in the beam. This filtering results in the spectrum of X-ray irradiation seen in Figure 3.3 with a peak energy around 50 keV. Measurements performed by the beamline scientists through a 100 μm slit using a Keithley 96030 ionization chamber connected to a Keithley 35050 dosimeter suggest that the maximum surface dose rate with 3 Cu filters is in the range of 2 Gy/s. This dose rate is for a tissue equivalent surface dose in air, the actual dose absorbed in the glass samples would be higher than this dose rate indicates.

Turning the beam "on" and "off" into the experimental hutch is a slow and imprecise method for controlling exposure time with such an intense X-ray source. So for these experiments the so-called fast shutter was used. This shutter is positioned in the beam just inside the hutch as shown in Figure 3.4 and is controlled by a computer program in the control room that allows us to set exposure times from 0.1 to 5000 seconds.

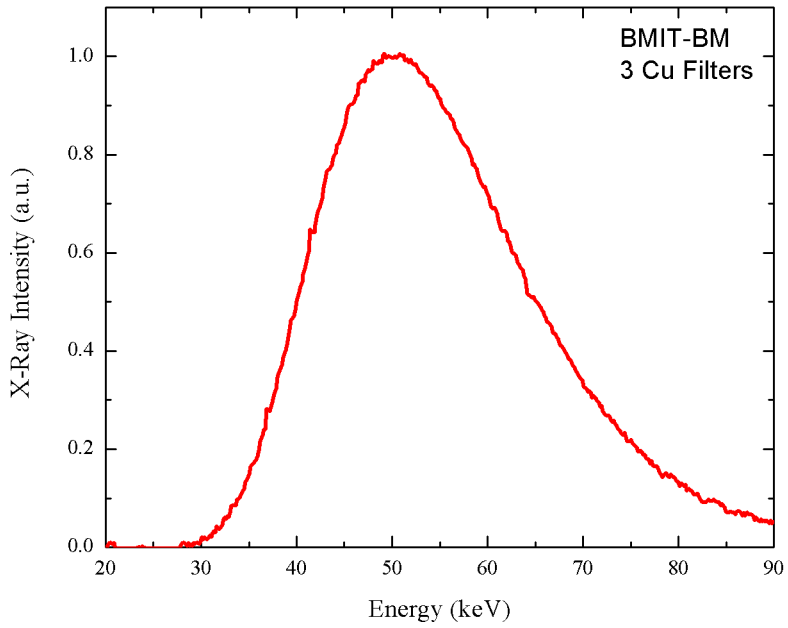

Figure 3.3: The normalized spectrum of X-ray energies from the BMIT-BM beamline with 3 Cu filters showing a peak X-ray energy of ∼50 keV. The spectrum was determined by calculations for a slit that was 10 mm in the horizontal and 0.1 mm in the vertical positioned so that the center of the slit was in the center of the beam 25.5 m from the bend magnet source, where irradiations were performed.

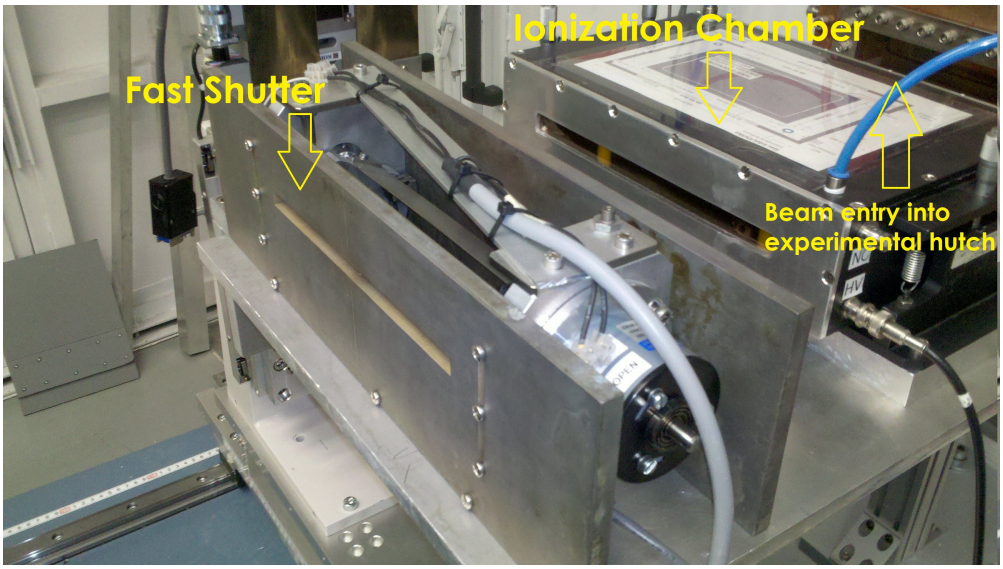

Figure 3.4: The fast shutter and ionization chamber positioned where the beam enters the experimental hutch for the BMIT-05BM beamline.

3.3 Photoluminescence

For this project two types of steady state photoluminescence experiments were performed. Measurements of the emission spectra of X-ray induced Sm^{2+}at low temperatures and measurements of the excitation spectra for both $Sm^{3+}$and Sm^{2+}in irradiated glass samples at room temperature. Figure 3.5 provides a general idea of the photoluminescence work station used for both type of experiments.

3.3.1 Low Temperature Emission Spectrum

For low temperature measurements the sample was cooled using a closed cycle He cryostat. The system consists of 22C Cryodyne Cryocooler, a compressor, and a cryostat controller. The sample was held in the sample holder which is connected to the cold head by sapphire bars. Before cooling the sample is sealed in a windowed chamber that is then evacuated down to 0.1 torr using a BOC Edwards, E2M0.7 rotary vacuum pump. The temperature was monitored with an Omega CYD211 temperature monitor. This system allows for the sample to be cooled to a temperature as low as 12 K.

To obtain an emission spectrum from the now cooled sample, a 532 nm laser is used to excite the irradiated sample. The laser light was reflected off of a mirror through the window of the vacuum chamber and onto the sample. The fluorescent light from the sample is then collected by lens and is passed through a filter to remove any reflected laser light before passing into an Oriel Cornerstone 130 Monochromator. The light is dispersed by the diffraction grating and the photons of the selected wavelength, set via computer control, pass through to a Hamamatsu C7950 photomultiplier tube which converts the incoming electromagnetic radiation into an electrical signal. The electrical signal is then read by a Spectra-Physics 70310 optical power meter. The computer controls the monochromator rotating the diffraction grating so an intensity signal is recorded every 0.2 nm over a range from 630 to 750 nm. Figure 3.6 is a schematic of the experimental setup described above.

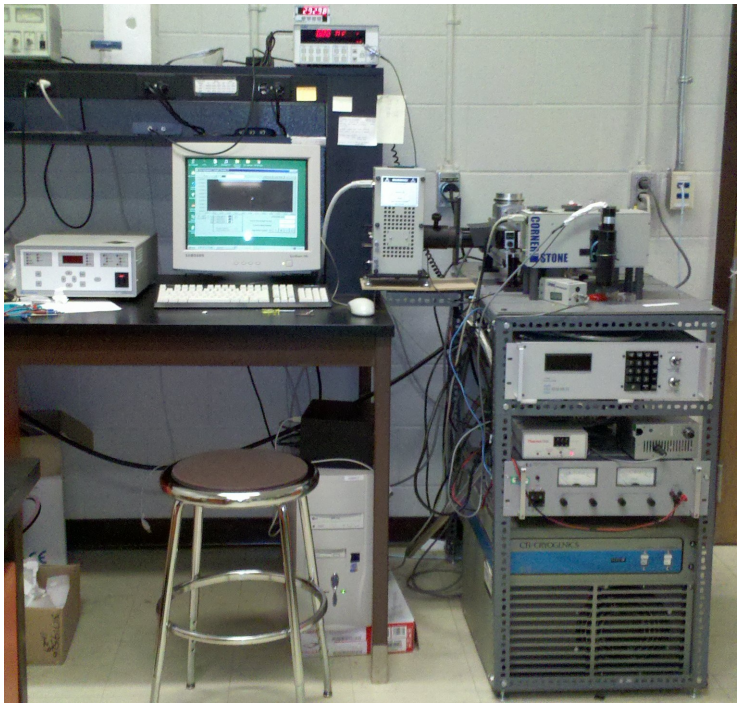

(a)

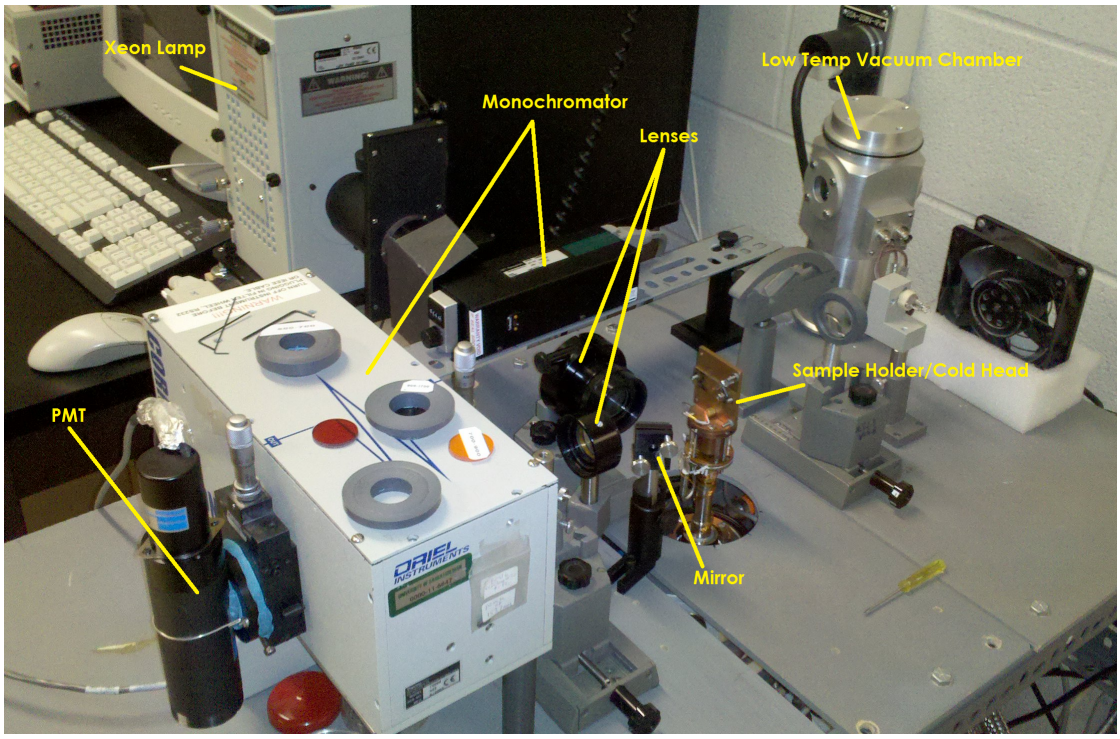

(b)

Figure 3.5: The work station for photoluminescence experiments.

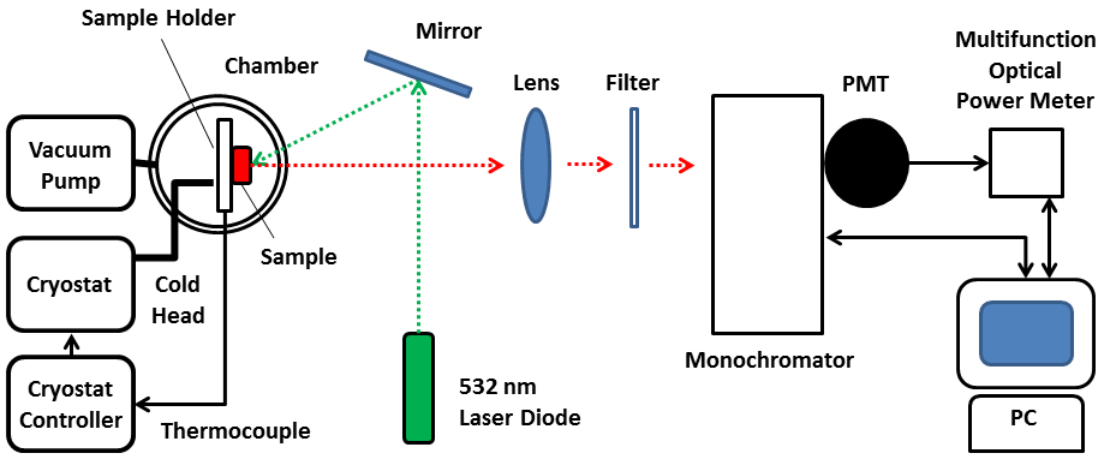

Figure 3.6: A schematic diagram of the experimental setup for obtaining low temperature emission spectra.

3.3.2 Excitation Spectrum

For excitation spectra the sample is placed in the sample holder where it is then illuminated one nanometer of wavelength at a time. The excitation source is a Spectra-Physics 66902 halogen-xenon lamp which produces light in a range covering UV to NIR. The Spectra-Physics 69907 power source ensures a constant power supply to the lamp, thus providing a steady intensity. The infrared light is filtered from the spectrum using a glass cuvette filled with distilled water. The light is then passed through a Newport monochromator (model 78025) that is hooked up to an Optometrics PCM-02 motor controller. The monochromator can be set to allow only light of a given wavelength pass through to the nearest nanometer. The selected wavelength of light is then collected by a lens and is reflected onto the sample. The fluorescent light is then collected as described in Section 3.3.1 except that the value of the collecting monochromator is fixed to the position of one of the emission peaks of Sm^{3+}or Sm^{2+}while the wavelength of the exciting light is changed by the first monochromator. Figure 3.7 is a schematic of the experimental setup described above.

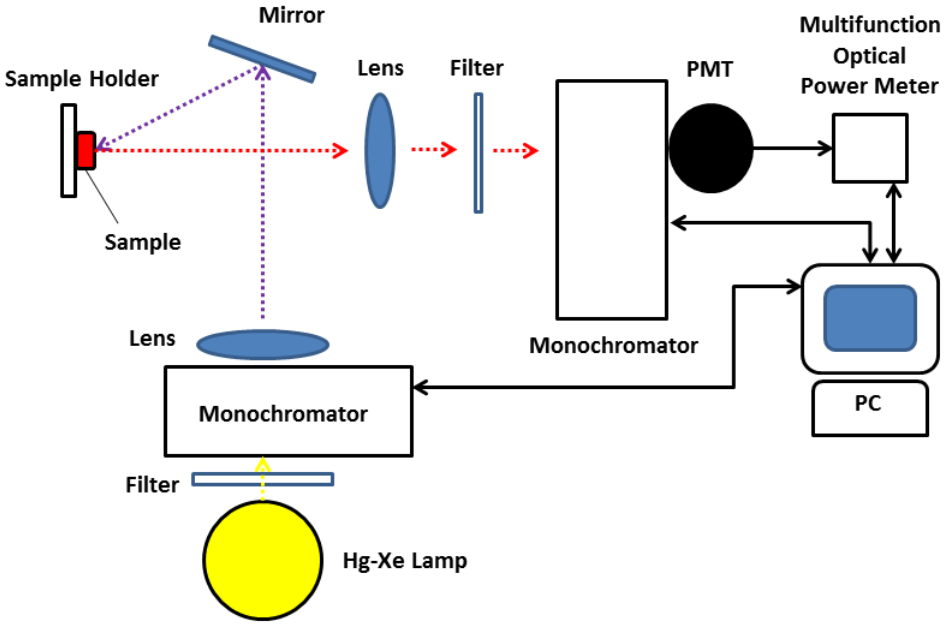

Figure 3.7: A schematic diagram of the experimental setup for obtaining excitation spectra.

3.4 Optical Transmission

This section describes the general procedure involved in acquiring optical transmission spectra.

3.4.1 Grinding and Polishing

Before any experiments can be performed, samples must be cut from the bulk glass. The cutting was performed using an IMPTECH Europe precision cutter with a diamond tipped blade. Ethylene glycol was used as a blade lubricant.

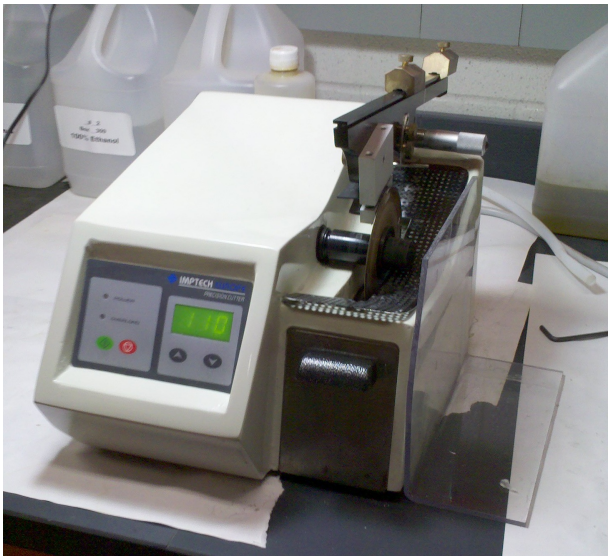

Figure 3.8: IMPTECH Europe precision cutter used to cut glass samples for experiments.

For transmittance measurements the samples must be ground down and polished. The grinding ensures that the sample surfaces are flat and parallel. The polishing procedure removes roughness and imperfections from the sample surface. These treatments act to reduce the amount of light scattered by imperfections and poor surface geometry. This process also helps to normalize the surfaces of samples that were prepared with different chemicals under different conditions. The procedure for grinding and polishing was adopted from previous work [62] [63]:

1. 600 micron silicon carbide powder is mixed with ethanol on a heavy glass plate

as depicted in Figure 3.9.

2. The sample is then placed on the plate and ground by dragging the sample through the slurry in a figure-eight pattern using one's hand and fingers. Additional powder and ethanol can be added as necessary. This ensures a flat surface on one side of the sample and removes any large defects such as deep scratches.

3. The sample is then adhered to the sample holder using bee's wax. The sample holder is warmed on the hot plate to approximately 80°C then a small amount of wax is melted onto the sample holder. The sample is then placed with the ground surface facing down onto the sample holder. The sample holder is then removed from the hot plate to cool so that bee's wax can solidify, thereby attaching the sample to the holder.

4. The other side of the sample is now ground as described above. Because the sample holder has an adjustable brass ring (see Figure 3.10) the sample can be ground down to a level set by the experimenter while guaranteeing that flat, parallel sides are maintained.

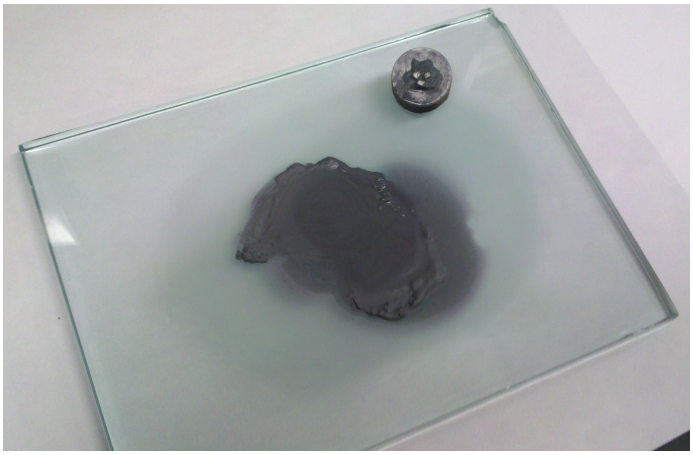

Figure 3.9: 600 micron silicon carbide powder mixed with ethanol on a heavy glass plate for grinding. On the top right: three pieces of glass adhered to the sample holder for grinding.

Figure 3.10: Thermolyne HP2305B hot plate, bee's wax, and sample holder for grinding and polishing.

Figure 3.11: From left to right: 0.05 micron alumina powder, 3 micron alumina powder, ethanol + glycol mixture, Buehler Minimet 1000 Polisher.

The next step in sample preparation is polishing. The polisher was a Buehler Minimet 1000 Polisher, shown in Figure 3.11. The polishing bowls have a glass plate in the bottom onto which the polishing cloth is adhered. The bowels can be slotted into place under the arm of the polisher and then the sample holder is then attached to the arm of the polisher, with the sample facing down onto the cloth. The sample is then polished as the machine arm moves the sample holder across the cloth in

circular motions. Polishing powder and a mixture of ethanol and glycol are added as a lubricant as needed. The arm of the polisher can be set to a speed ranging from 0 to 50 rpm with a downward force from 0 to 10 pounds for durations ranging in length from 30 seconds to 99 hours. The samples were polished using a three stage process:

1. The samples were polished using a rough cloth with a few drops of the ethanol and glycol mixture but without any polishing powder. The polisher speed was set to 50 rpm, the force was 1 pound, and the polishing duration was 10 minutes.

2. The sample was polished on a smooth polishing cloth with a few drops of the ethanol and glycol mixture and 3 micron alumina polishing powder. The polisher speed was set to 50 rpm, the force was 2 pounds, and the polishing duration was 10 minutes.

3. The sample was polished on a smooth polishing cloth with a few drops of the ethanol and glycol mixture and 0.05 micron alumina polishing powder. The polisher speed was set to 50 rpm, the force was 1 pound, and the polishing duration was 20 minutes.

Upon completion of the third stage of polishing the sample holder is once again placed on the hot plate to melt the bee's wax adhering the sample. The wax was cleaned from the sample using diethyl ether and then rinsed with ethanol. The sample is then reattached to the sample holder using bee's wax so that the polishing procedure may be performed on the other side of the sample.

3.4.2 Transmission Spectrum Measurement

All transmission measurements were performed using a PerkinElmer Lambda 900 spectrophotometer. A sketch of the exterior is shown in Figure 3.12 and Figure 3.13 is a schematic depicting the inner workings of the device.

The spectrophotometer contains two different lamps as light sources. There is a deuterium lamp (DL) to produce the ultraviolet (UV) light and a halogen lamp (HL)

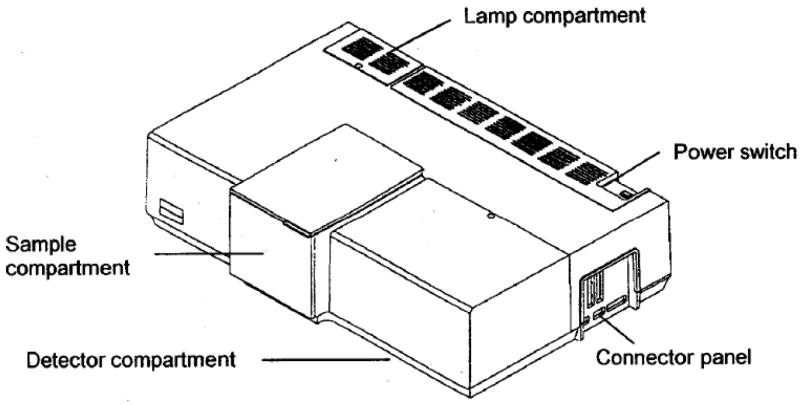

Figure 3.12: A sketch of the PerkinElmer Lambda 900 spectrophotometer. Diagram after reference [64].

to produce the visible (Vis) and near infrared (NIR) part of the spectrum.The lamps were turned on approximately one hour before the spectrophotometer was used to allow time for their spectrum to stabilize. The choice of radiation source is controlled by mirror M1. This device has two monochromators (G1 and G2) each with two diffraction gratings, one for the UV/Vis part of the spectrum and one for the NIR part of the spectrum. The light is guided from the source to the monochromators by mirrors (M1-M6), a slit assembly (SA), and an optical filter wheel assembly (FW) which is synchronized with the monochromators so that for a desired wavelength the correct filter is in place. The light then passes through a common beam mask (CBM) and a chopper (C) via mirrors (M6-M8). When the chopper is not actuated the light reflects off of the mirrors (M9 and M10) and passes through the reference beam attenuator (RBA) into the sample compartment to create the reference beam. The intensity of the reference beam is then measured by a photomultiplier (PM) for light in the UV/Vis range or a Peltier-cooled lead sulfide detector (PbS) for the NIR range. The detector is selected by a rotating mirror (M14). When the chopper is actuated the light is reflected off a mirror (M10') and passes through the sample beam attenuator (SBA) into the sample compartment to create the sample beam. The light that is transmitted through the sample is then detected by one of the previously mentioned detectors. Both reference and sample beams are measured for every wavelength and the difference in intensity between the two beams gives the

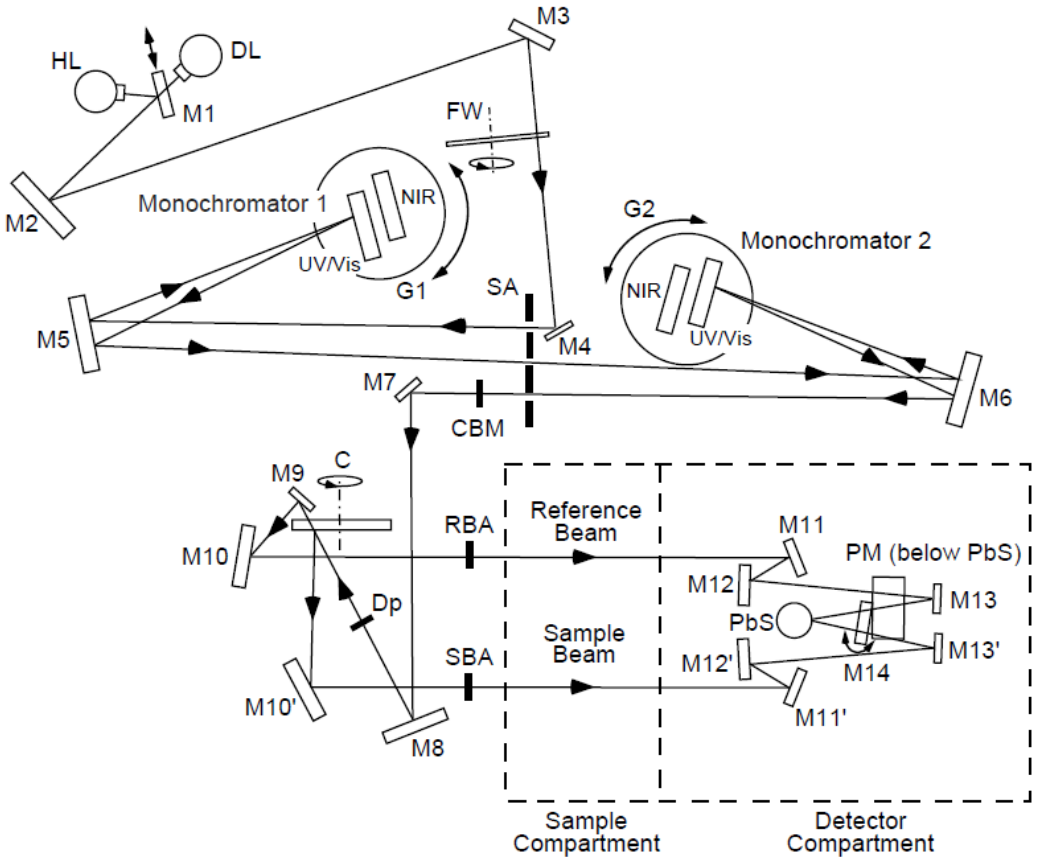

Figure 3.13: A schematic diagram of the PerkinElmer Lambda 900 spectrophotometer. Diagram after reference [64].

transmittance of the sample for that wavelength.

The UV WinLab L800/L900 software allows for a fair amount of control in the scan settings [65]. For this project the typical scan was from 1800 nm to 180 nm with data being collected every nanometer. The slit size was also set to one nanometer. The detector integration time was set to 0.08 seconds for the UV/Vis range, resulting in a scan speed of 500 nm/min. In the NIR range the integration time was set as 0.12 seconds resulting in a scan speed of 500 nm/min.

All samples were placed on slides that only let a pinhole of light pass through to the detectors to make sure that each sample's transmittance was measured at the point where it was exposed to the vertical middle of the X-ray beam where the flux is highest.

3.5 Dose Profile Measurements

The dose profile measurements were all performed using the BMIT-BM beamline at the CLS. All irradiations were performed with 3 Cu filters in place resulting in the beam profile described in Section 3.2.2. Figure 3.15 is a schematic of the experimental setup described in this section. The beam enters at one end of the experimental hutch where it passes through an ionization chamber that is used to confirm that the beam is in fact on in the hutch. After the ionization chamber is that fast shutter which is used to control the sample exposure times. When the fast shutter is open the beam is then incident on the sample. The sample is held in the so-called "black box" apparatus which will be discussed in the next paragraph. The sample is initially aligned in the beam by using two laser levels inside the hutch (horizontal and vertical) moving the stage the black box is mounted on. For finer alignment and beam sizing a closed circuit camera in the hutch is aimed at a X-ray scintillator placed in the sample holder of the black box. Then the beam is let into the hutch with the lights off. Under these conditions it is possible to see the size and location of the beam from the control room. The stage moved as necessary by computer control (Figure 3.14) to center the sample in the beam. The beam size is then adjusted using the computer interface until it is large enough to cover the sample without hitting the sample holder. A typical beam size for these experiments is 6 mm $\times$ 6 mm at 23 m from the source.

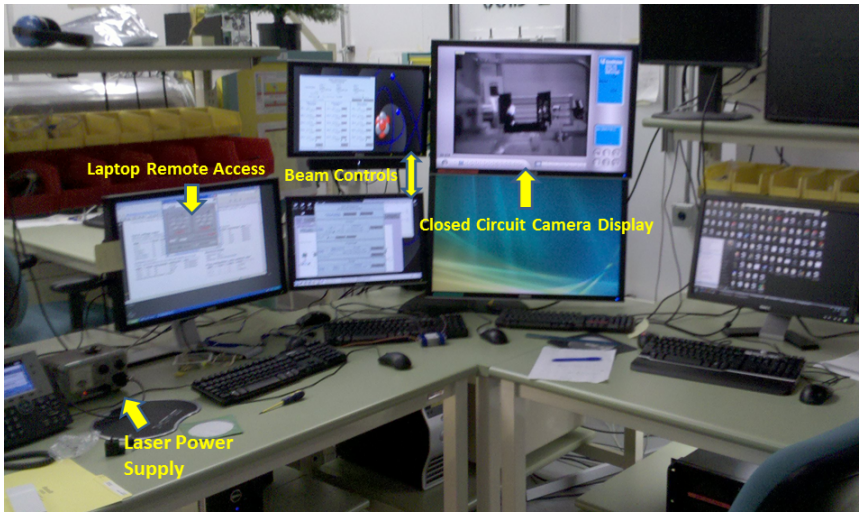

Figure 3.14: The control room for the BMIT-05BM beamline at the CLS.

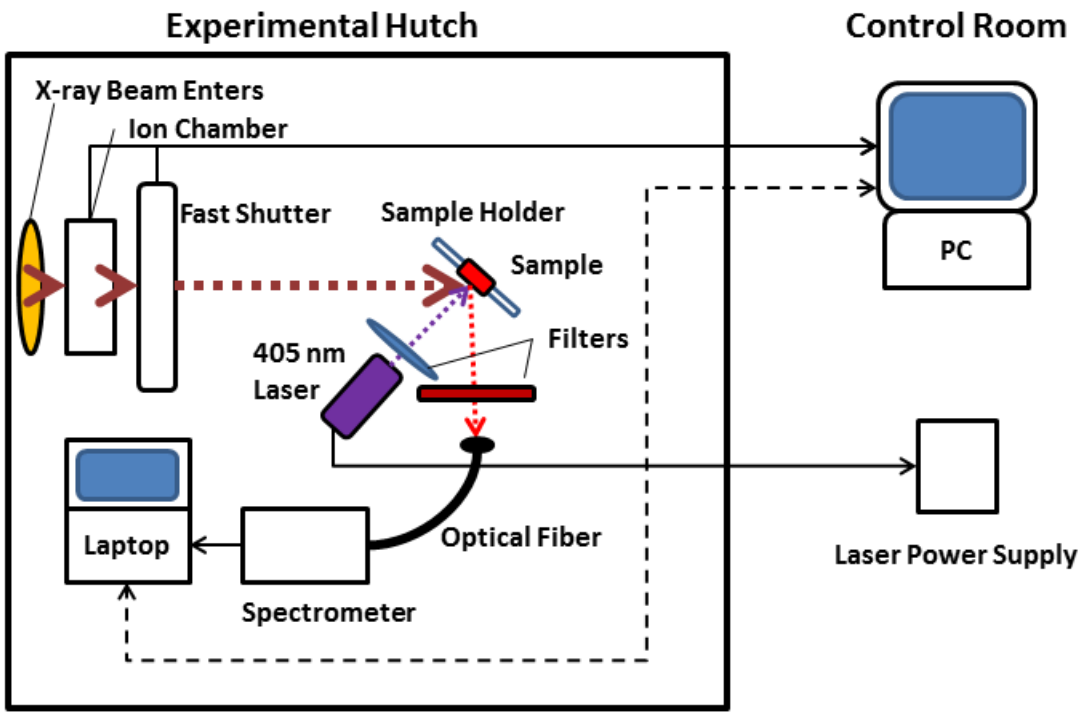

Figure 3.15: A schematic of the experimental setup for dose profile measurements at the BMIT-BM beamline at the CLS.

The black box (Figure 3.16) contains the PL system used to determine the conversion of $Sm^{3+}$to Sm^{2+}. Within the "black box" the sample holder is an aluminum plate with the center drilled out. The plate is held in the black box using a microscope slide holder. The sample is attached to the sample holder using Kapton tape which is made of polymers that do not interact significantly with the X-rays and also does not fluoresce under the excitation light. After irradiations the sample is excited with an unfocused 405 nm laser diode held in the side of the "black box". The laser is powered by a variable voltage power supply that is kept in the control room of the beamline so that it can be turned on and off from outside the hutch. The fluorescent light from the sample passes through a red filter to remove any reflected laser light where it is then collected by a multimode optical fiber which guides the light to the spectrometer. The spectrometer is a StellarNet EPP2000 spectrometer that operates across a range from 230 to 1100 nm with a spectral resolution of 0.5 nm. Inside the hutch the spectrometer is plugged into a laptop which is then remote accessed by a

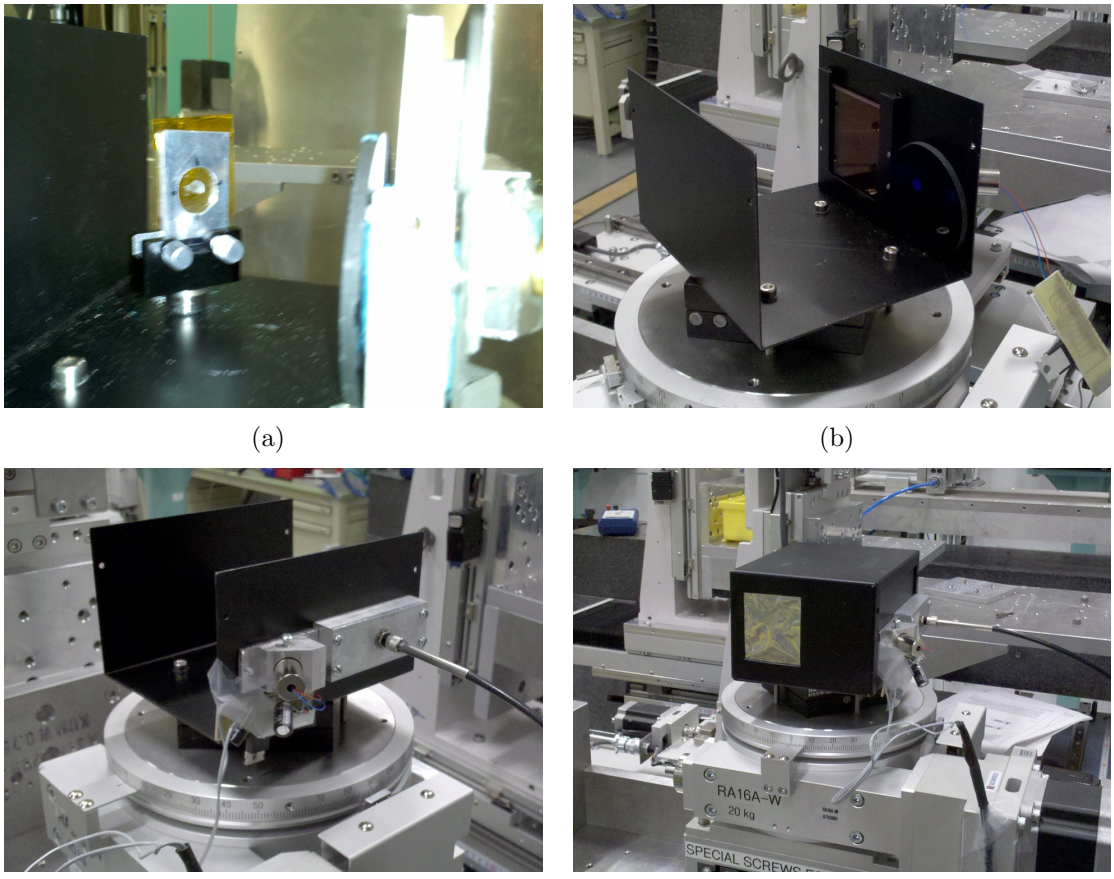

(a) (b)

(c) (d)

Figure 3.16: The "Black Box" used for dose profile experiments at the CLS. (a) A sample held in the apparatus for dose response using Kapton tape. (b) The blue filter over the excitation source and the red filter covering the fiber to the detector. (c) The 405 nm laser diode for excitation and the multimode optical fiber that collects the fluorescence and transports it to the spectrometer. (d) The apparatus cover with thin aluminum foil "window" to limit interactions with the X-ray beam.

computer in the control room.

Using this experimental setup PL spectra are saved for the as prepared sample and then again after total irradiation times of 0.1s, 0.2s, 0.5s, 1s, 2s, 5s, 10s, 20s, 50s, 100s, 200s, 500s, 1000s, 2000s, etc.

3.6 Electron Paramagnetic Resonance

The EPR experiments were performed at the EPR Laboratory at the Saskatchewan Structural Science Center (SSSC). The spectrometer at the SSSC is a Bruker EMX EPR Spectrometer, shown in Figure 3.17. It uses an ER041XG Microwave Bridge X-Band source with 200 mW leveled source output. The apparatus offers 1 dB attenuation with 0.5 dB precision up to a maximum attenuation of 60 dB. The magnetic field is generated with 10 inch magnets powered by a 2.7 kW power supply with a Hall Field Controller with an operating range 100 G-18 kG with a field accuracy better than 800 mG over the full operating range. Sweeps are performed in 100 mG steps with a resolution of 2 mG [66].

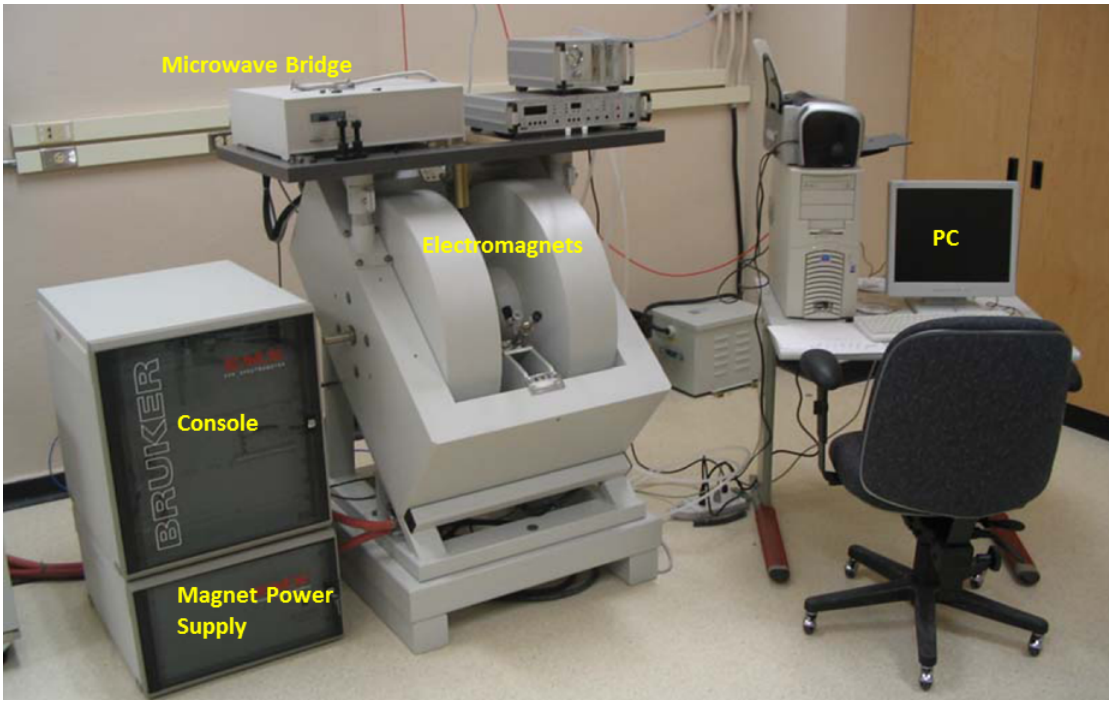

Figure 3.17: The EPR Laboratory at the SSSC.

The electromagnets were always powered up at least one hour before experiments to allow time for the field to stabilize. Calibrations were performed with the sample tube in the resonant cavity, empty, then a baseline spectra of the tube is taken. Experiments were performed on pieces of FP glass that had been irradiated in the Faxitron X-ray chamber. The samples were placed inside a 3 mm quartz tube that

was then lowered into the middle of the resonant cavity. A sample tube is shown in the resonant chamber in Figure 3.18. The scans and scan settings are controlled by the WINEPR Acquisition software on the PC. The scans had a center field of 3200 G with a scan sweep of 2000 G. The attenuation was set to 20 dB which gives microwaves with a power of 2.01 mW. Each spectra was the result of nine scans taken back to back.

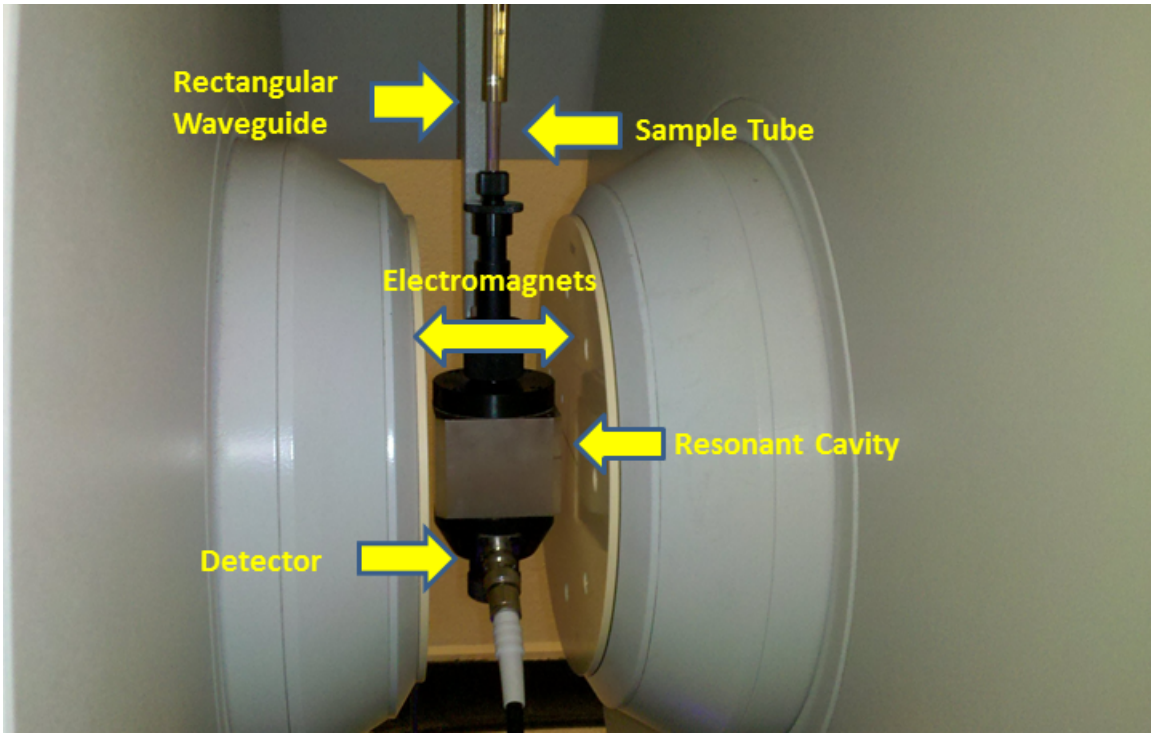

Figure 3.18: A close-up of the sample area of the EPR spectrometer at the SSSC.

3.7 Photobleaching

Irradiated samples were exposed to various excitations sources in order to determine what effect such exposure would have on the optical properties of the samples. Samples were exposed to laser light at 405 nm and 532 nm and UV light from LEDs centered at 315 nm and 285 nm. After various exposure times the photoluminescence and transmission spectra were measured. Separate samples were used for PL and transmission experiments.

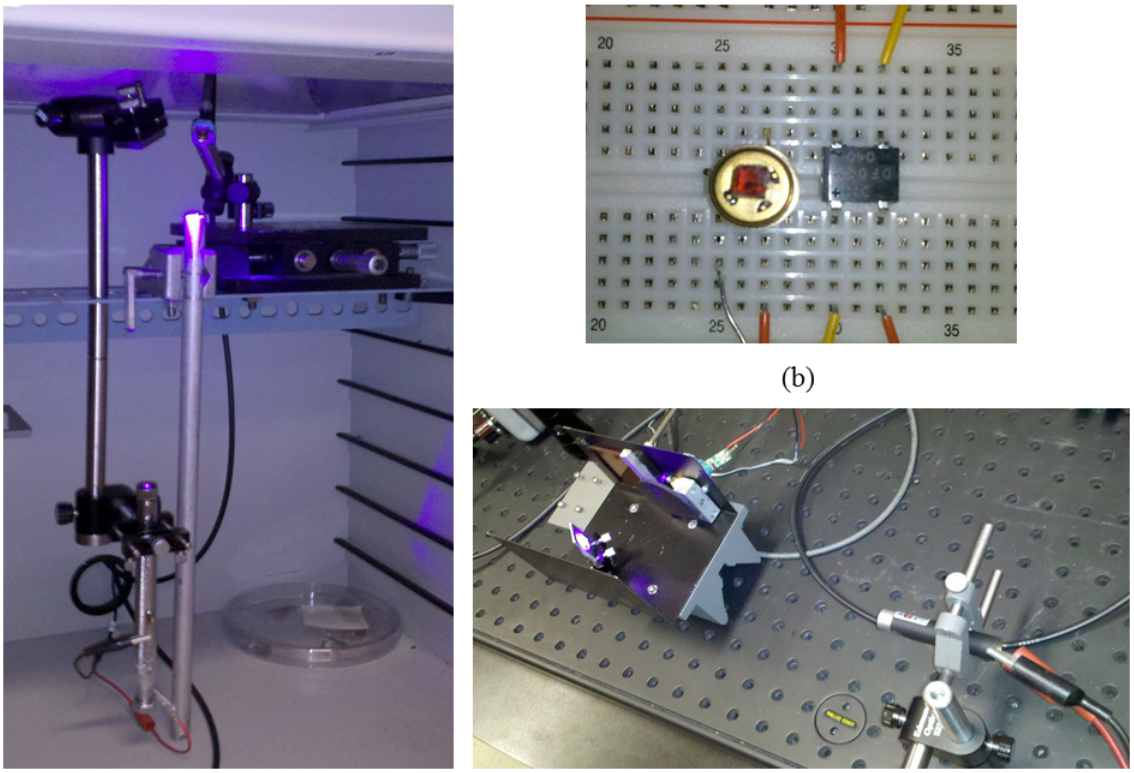

(a) (b) (c)

Figure 3.19: Bleaching samples for PL measurements: (a) A sample being bleached by a 405 nm laser inside the Faxitron X-ray cabinet. (b) A sample being bleached, sitting on the glass window of a UV LED. (c) A sample being bleached with a 532 nm laser in the black box apparatus.

For photobleachingsamples with the 405 nm laser the sample was left in the Faxitron X-ray chamber which is outfitted with a laser diode and a lens attached to an optical fiber that runs out of the chamber to an ASEQ Instruments LR1 spectrom-

eter. This spectrometer operates over the range of 237 nm-1073 nm with a spectral resolution of ∼0.3 nm. This setup is depicted in Figure 3.19 (a). For PL measurements in the UV range the sample was placed directly on the window of the LED as shown in Figure 3.19 (b). The black box apparatus described in Section 3.5 was used for photobleachingPL measurements with the UV LEDs and the 532 nm laser. The photobleachingwith the green laser is shown in Figure 3.19 (c).

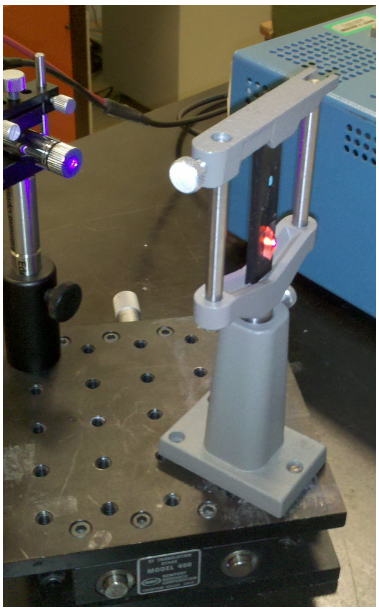

Figure 3.20: For transmission measurements the sample is bleached while on a transmission sample slide.

For all of the photobleachingexperiments involving transmission measurements the sample was placed on a transmission slide after irradiation and was left on the slide for the duration of the experiment so that all measurements were of the exact same part of the glass. A sample being bleached on a transmission slide can be seen in Figure 3.20.

Since both lasers and LEDs were used as excitation sources, to compare the effect of the different wavelengths it is necessary to know something about the relative optical power of the devices. So all of the above mentioned excitation sources were measured using a Thorlabs PM100D Optical Power Meter with a Thorlabs S120VC which has a range of 200-1100 nm and saturates above 50 mW. The measured inten-

sities of the sources can be found in Table 3.1.

Figure 3.21: Measuring the optical power of a 315 nm LED with a Thorlabs S120VC sensor attached to a Thorlabs PM100D optical power meter (insert).

Table 3.1: Optical Power of Excitation Sources for Photobleaching

Excitation Source	Optical Power (mW)	
	Photoluminescence	Transmission
405 nm laser	27	27
532 nm laser	26	26
315 nm LED	0.56	0.13
285 nm LED	0.78	0.20

Figure 3.22: Bleaching a sample for dose profile repeat experiments using a Model DE-4 EPROM Eraser UV lamp with a peak intensity of 254 nm.

In addition to the PL and transmission experiments, photobleachingwas also part of dose profile and EPR experiments. For the dose response experiments the as-prepared sample was irradiated for dose profile measurements as described in Section 3.5. The aluminum sample holder slide, with the sample in place, was then removed from the slide holder and placed in the tray of a Model DE-4 EPROM Eraser which is a high power UV lamp with a peak intensity around 254 nm (Figure 3.22). The sample was exposed to the UV light for one hour and then returned to the black box where another dose profile was performed. This process was repeated multiple times on the same sample.

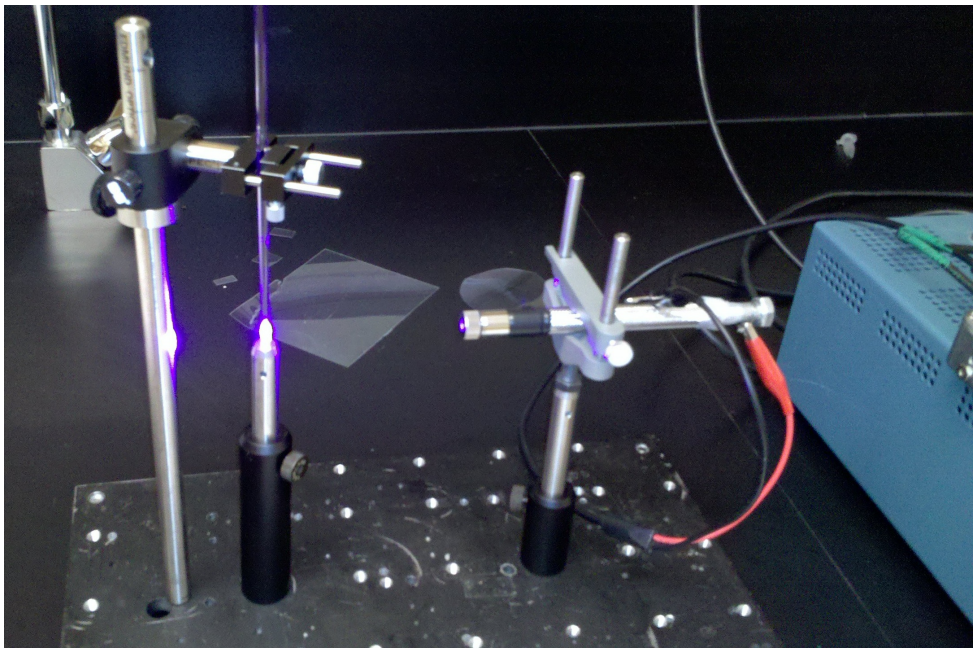

Figure 3.23: Bleaching a sample for EPR measurements with a 405 nm laser. The sample is kept in the tube to reduce contamination.

The photobleachingfor EPR measurements was performed with the 405 nm laser. The quartz sample tube was removed from the resonant chamber and placed in a holder in front of the laser (Figure 3.23). The sample was left in the tube to reduce the chance of contaminating the sample. The tube was marked to make sure it was placed back into the resonant chamber at the same depth and orientation to avoid any changes in intensity caused by a change in sample position. The EPR scans were performed as described in Section 3.6.

4. Results and Discussion

It should be noted from the onset that the results and subsequent discussions do not make specific mention of the different FP glass compositions described in Section 3.1 since the results of the experiments were the same for all three FP glass compositions.

4.1 Photoluminescence Characterization

This section on photoluminescence is focused on the excitation and low temperature emission spectra. The PL measurements detailing the conversion of $Sm^{3+} \rightarrow Sm^{2+}$is covered in Section 4.3 Dose Profile Curves.

4.1.1 Excitation Spectrum

An excitation spectrum represents the measured signal intensity of a PL emission peak as a function of the wavelength of the excitation source. These spectra are used to determine which wavelength an excitation source should operate on to generate the most intense fluorescence. The excitation spectra for $Sm^{3+}$and Sm^{2+}were determined for the range of 350-550 nm. The normalized spectra are presented in Figure 4.1. For $Sm^{3+}$the intensity of the PL emission peak at 596 nm was measured, which corresponds to the $^4G_{5/2} \rightarrow {}^6H_{7/2}$ transition [32]. The excitation spectrum for $Sm^{2+}$was obtained by measuring the intensity of the PL emission peak at 682 nm which corresponds to the $^5D_0 \rightarrow {}^7F_0$ transition [33]. The measured excitation spectra for $Sm^{3+}$and Sm^{2+}in the X-ray irradiated FP glass are very similar to the reported excitation spectra for these ions in other glass hosts [31] [45].

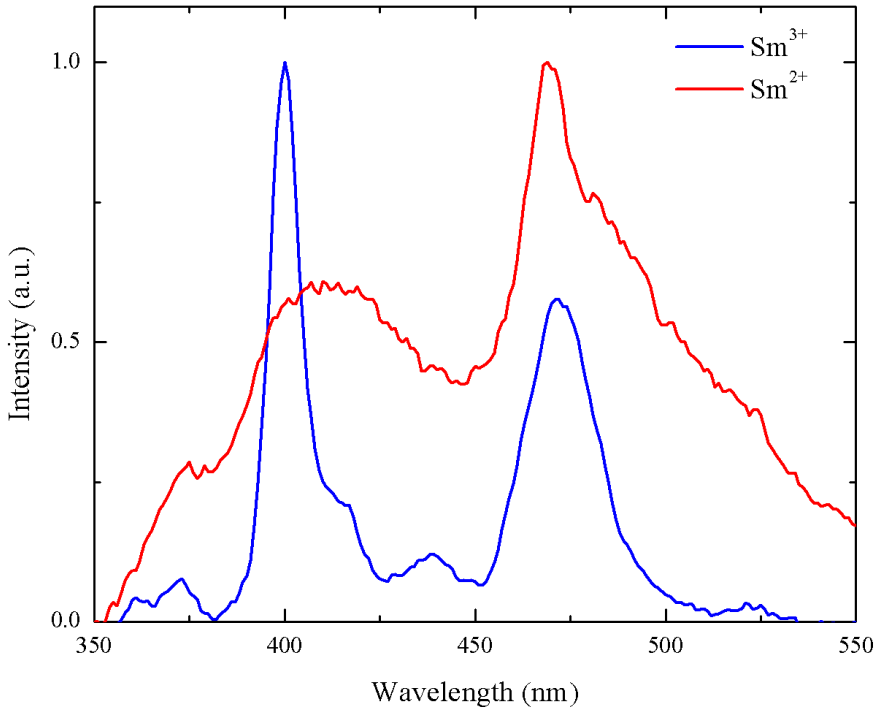

Figure 4.1: The normalized excitation spectra for $Sm^{3+}$and Sm^{2+}in an FP glass. The sample before irradiation contained 0.5% $Sm^{3+}$and was then irradiated at the CLS for 2000s. The excitation spectrum for $Sm^{3+}$was obtained by measuring the intensity of the 596 nm emission band. The excitation spectrum for $Sm^{2+}$was obtained by measuring the intensity of the 682 nm emission band. The overlapping peaks of the excitation spectra, at 405 and 470 nm, indicate the best wavelength choices for a source to excite the emission spectra of these ions.

Figure 4.1 clearly shows that 405 nm is a good choice for an excitation source for measuring the PL of both $Sm^{3+}$and Sm^{2+}. An excitation source operating around 470 nm would also work. Knowing which excitation sources can excite both $Sm^{2+}$and Sm^{3+}at the same time in the FP glass is important because it is the ratio of $Sm^{2+}$to Sm^{3+}that will be used to determine the delivered dose from the X-rays. It can also be seen that it is possible to excite only Sm^{2+}within this range. For example Sm^{2+}can be excited using a common green laser operating at 532 nm without exciting the Sm^{3+}ions.

4.1.2 Low Temperature Emission Spectrum

There have been a variety of experiments that show that the emission spectra of $Sm^{2+}$is temperature dependent in some host materials [37] [33] [28] [26] [27]. It is important to know if that is the case for the spectra in the FP glass as well because these same experiments have shown that the intensity of the radiative transitions increases as the temperature of the sample is decreased. This increase is to be expected as lower temperatures result in less atomic vibrations which means a decreased chance of non-radiative relaxation of excited electrons which results in a stronger PL emission. The increase in emission intensity for Sm^{2+}at low temperatures in the FP glass host depicted in Figure 4.2. This increase in signal intensity at low temperatures could prove useful for making precise dosimeter out of the Sm-doped glass as it would provide a stronger signal-to-noise-ratio when "reading" the dosimeter.

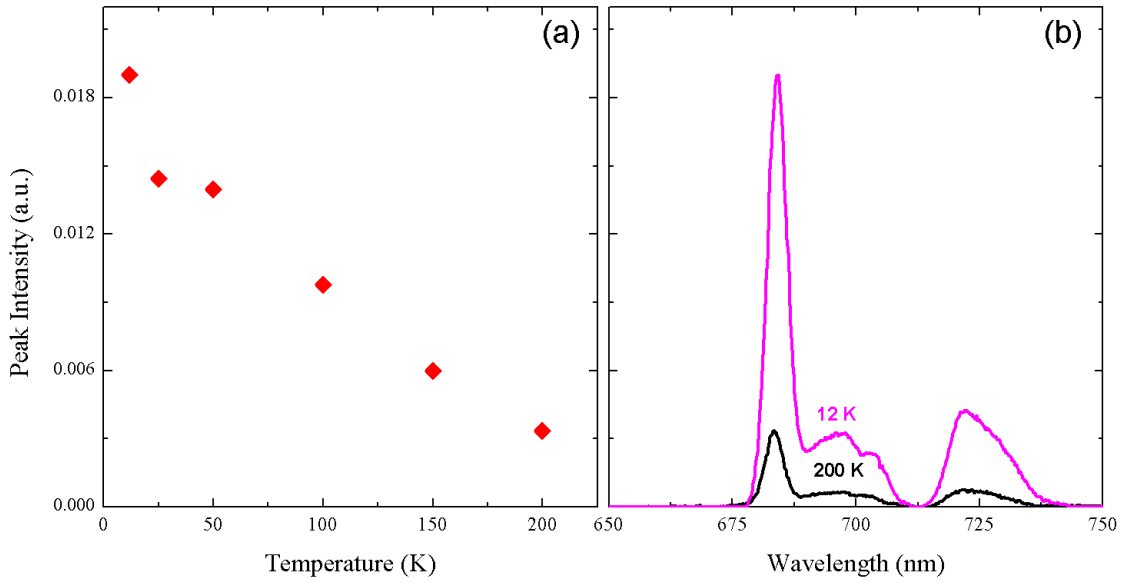

Figure 4.2: (a) The dependance of the intensity of the $^5D_0 \rightarrow {}^7F_0$ transition on temperature. (b) Sm^{2+}emission spectra intensity at two temperatures.

Figure 4.3 shows that there is no significant change in the number or position of the peaks that make up the emission spectrum for Sm^{2+}over a range from 200 K down to 12 K. This means that if the irradiated samples were to be read at lower temperatures the detection range would not have to be changed which simplifies the

modifications that would have to be made to the confocal microscope to read the dosimeter at low temperatures.

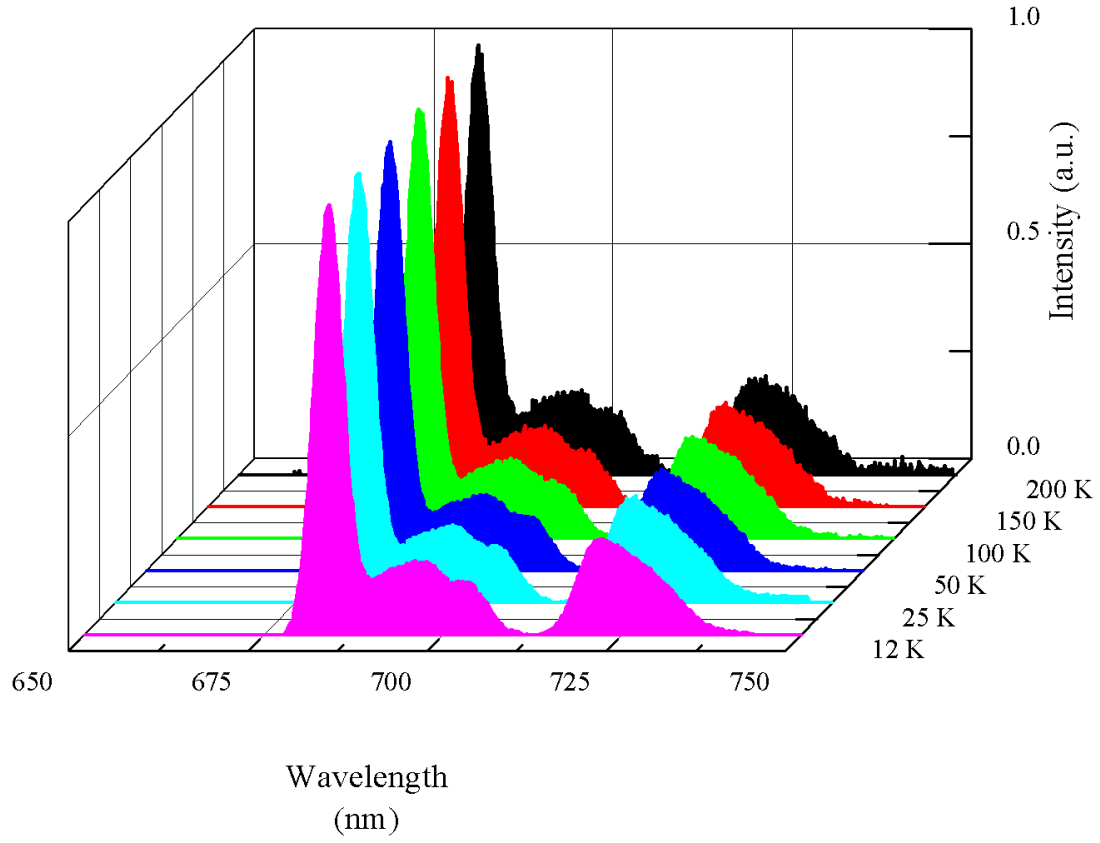

Figure 4.3: The emission spectrum of Sm^{2+}at a variety of low temperatures, normalized to peak intensity. The normalized spectra show that there is no change in the position of Sm^{2+}emission peaks at lower temperatures. The sample originally contained 0.2% $Sm^{3+}$and was irradiated at the CLS for 5000s. The excitation source for this emission was a 532 nm laser.

4.2 X-Ray Induced Effects

For the purposes of this section, X-ray induced effects will refer to phosphor and oxygen hole and electron centers that form in the glass as a result of X-ray irradiation. These effects will be characterized using two methods, the induced optical absorption of the irradiated glass and the EPR spectra of the irradiated glass. Changes in the oxidation state of samarium will be examined directly in Section 4.3.

4.2.1 Optical Absorption

As outlined in Section 3.4.2 the transmission spectra of the "as prepared" and irradiated samples were measured. Examples of these transmission spectra for FP glasses containing 0.2% $Sm^{3+}$and 0.0% Sm^{3+}can be seen in Figure 4.4 (a) and (b). However other than determining that there is difference in the spectra for samples containing Sm versus a sample without Sm there is little to glean from this presentation. That is why the transmission data is instead presented as induced optical absorbance which is a modification of absorbance.

Absorbance is a quantitative measurement of the logarithm of the ratio of the radiation that is incident on a material and the radiation transmitted through the material. Induced absorbance modifies this concept by measuring the ratio of the radiation transmitted through an "as prepared" sample and the radiation transmitted through an irradiated sample. This method has the benefit of giving an absorbance spectrum that is solely the product of X-ray induced effects in the glass, removing any absorbance caused by the glass before irradiation.

$$A(\lambda) = -\log_{10}\left(\frac{I_{\text{irradiated}}(\lambda)}{I_{\text{as prepared}}(\lambda)}\right) \tag{4.1}$$

The induced absorbance spectra for a variety of irradiation times for a Sm- doped sample and a sample without any Sm are shown in Figure 4.4 (c) and (d).

It is possible to analyze induced absorbance spectra by fitting it by summing a

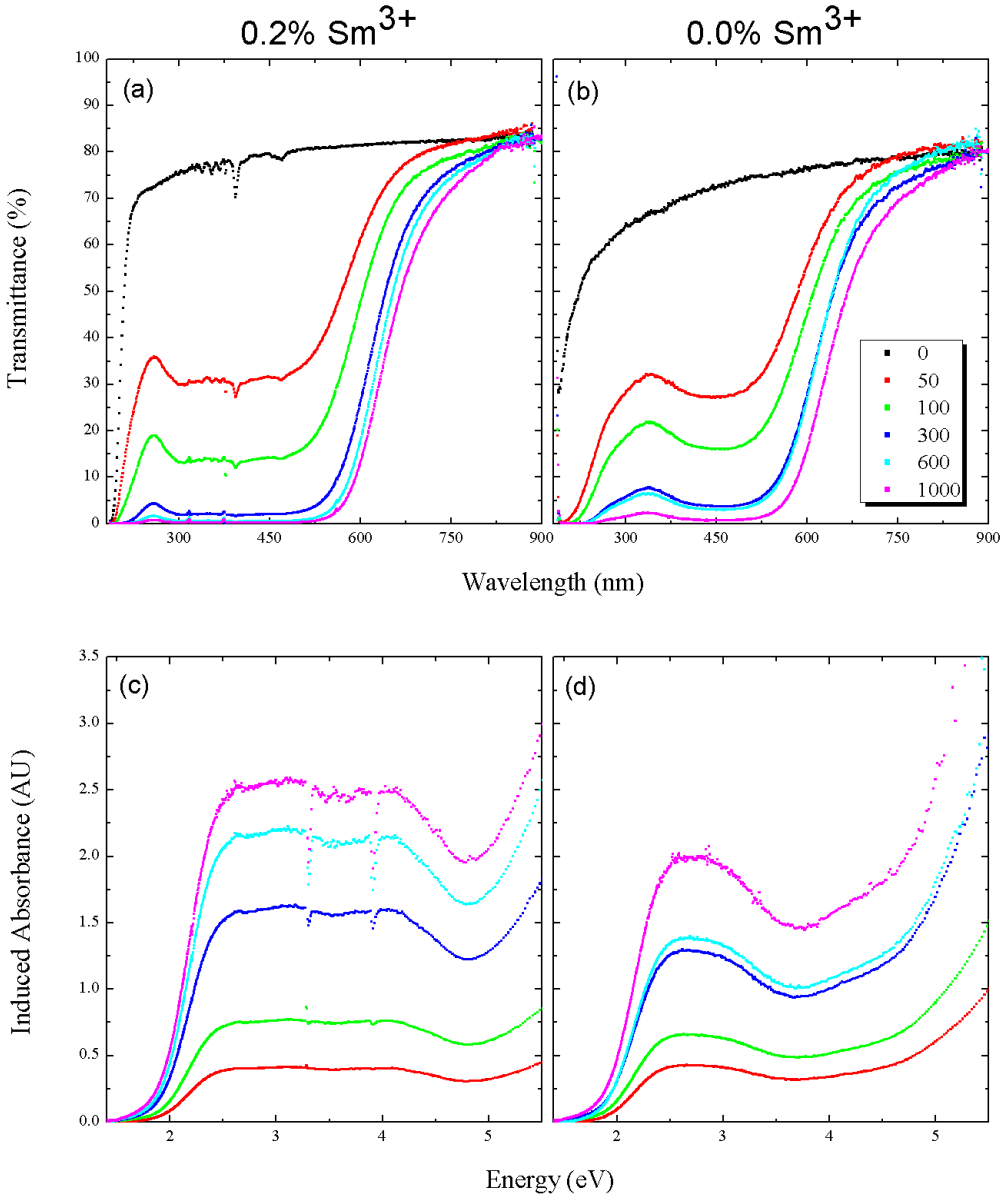

Figure 4.4: (a) 0.2% $Sm^{3+}$and (b) 0.0% Sm^{3+}show the transmission spectra for FP glass samples irradiated for 0, 50, 100, 300, 600, and 1000s at the CLS with 3 Cu filters. (c) and (d) is the same data expressed as induced absorbance.

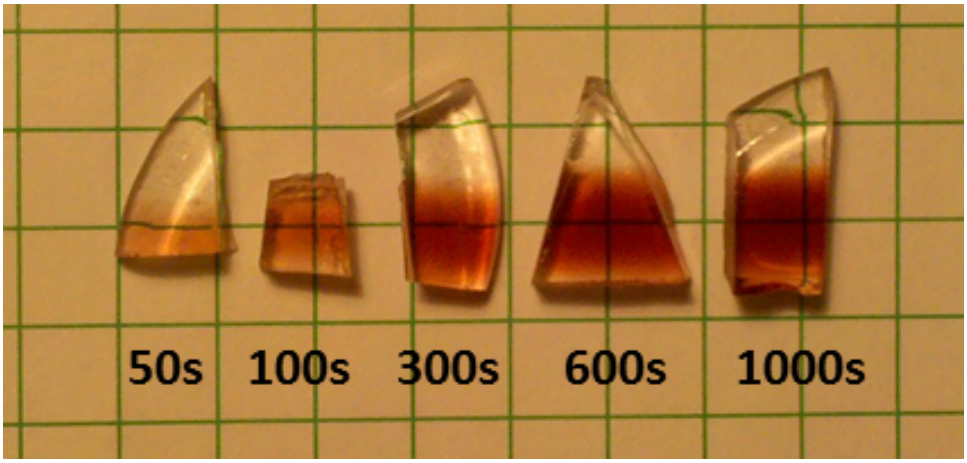

Figure 4.5: A visual inspection of FP glass samples containing 0.1% Sm^{3+}that were irradiated for 50s, 100s, 300s, 600s, and 1000s at the CLS with 3 Cu filters. The irradiated bottom sections of the samples clearly demonstrate the induced absorbance in the visible part of the spectrum caused by the X-ray induced effects when compared to the unexposed top sections.

series of overlapping Gaussians. The fit to experimental data and the Gaussians that the fit is composed of are displayed in Figure 4.6 for both doped and undoped samples. Four of the Gaussians marked G1, G2, G3, and G4 are of particular interest and the average central energies (E) and wavelengths (λ) are presented in Table 4.1.

It is widely accepted that the radiation induced absorbance is related to atomic scale defects appearing in a glass structure and in some glasses these defects have been identified by comparing the induced optical absorption with EPR spectra. For example, references [49], [47], [50], and [48] show such an identification for fluorophosphate glass. These papers have shown that phosphorus-oxygen hole centers (POHC) in phosphate glasses form several absorption bands in the visible and near UV part of the spectrum. The values of the Gaussians G1-G5 from this work are compared to the absorption bands in the same range [48] in Table 4.1. The agreement of the results implies that X-ray induced absorption in the samples is related to POHCs. Additionally, the close match between the bands G1-G5 to the previously reported bands would seem to suggest that the absorption from $Sm^{2+}$is a minor effect.

Another point of interest from the induced absorbance experiments is the differ-

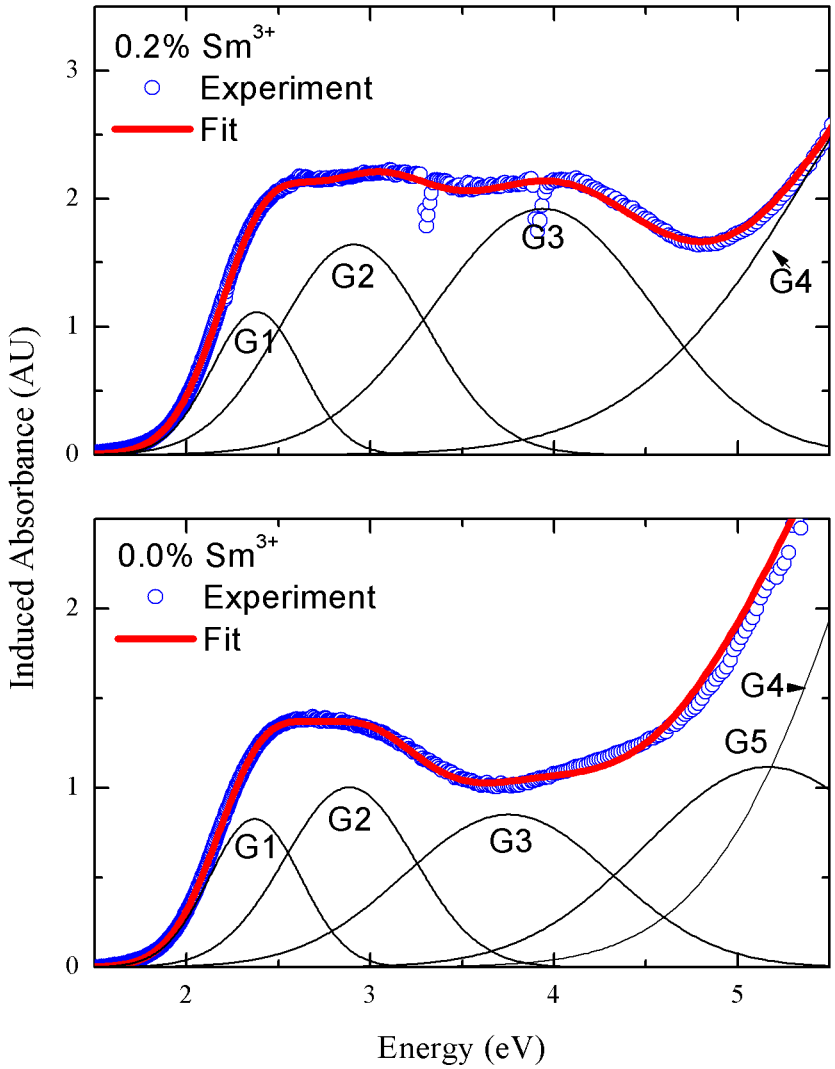

Figure 4.6: This figure illustrates the Gaussian absorption bands used to fit the induced absorbance of the irradiated FP glass. Both spectra are for samples irradiated 600s at the CLS with 3 Cu filters.

ence between the spectra for samples doped with Sm and the same glass without Sm. As indicated in Figure 4.6 the samples with Sm has four Gaussians (G1-G3) in the visible to near UV all of which match up well with the POHC absorption bands and one band (G4) which matches closely with the absorption band for the electron center PO_3 reported in other papers. However the induced absorbance for the sample without any Sm requires a fifth Gaussian (G5) which can be matched to an absorption band reported to be PO_4 which is also an electron center. This suggests that under

X-ray irradiation electron-hole pairs are created and in the Sm-doped samples the Sm^{3+}acts as an electron capture center.

Figure 4.7 shows that the change in intensity of the POHC absorption bands and the PO_3 electron center in Sm-doped samples under X-ray irradiation may be approximated as:

$$x(t) = x_0 \left[1 - \exp\left(\frac{-t}{\tau}\right)\right] \tag{4.2}$$

with $\tau \approx 270$s where the parameters x_0 and τ do not depend on the concentration of Sm in the glass. The fit of this exponential decay and its apparent independence from the Sm concentration of the samples suggests that no matter how many Sm^{3+}ions are available to act as electron centers the capture of X-ray produced electron-hole pairs is limited by the availability of POHCs, of which there is a finite amount independent of the amount of samarium present in the glass.

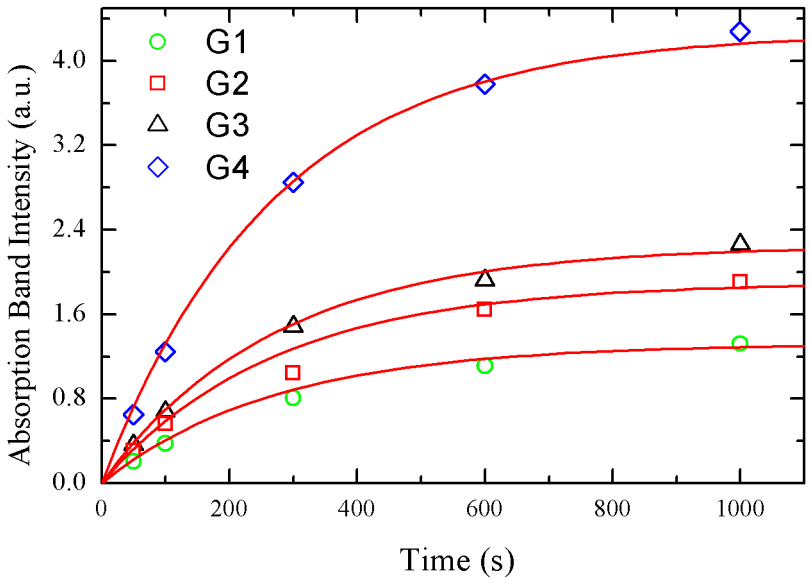

Figure 4.7: The change in absorption band peak intensity with irradiation time for a sample doped with 0.2% Sm^{3+}. The sample was irradiated for 50, 100, 300, 600, and 1000s at the CLS with 3 Cu filters. The red lines are the exponential fit with τ=270s and varying x_0 values.

Based on the conversion of $Sm^{3+} \rightarrow Sm^{2+}$(discussed in more detail in Section 4.3) and the formation of POHCs in the irradiated glass it would seem that the X-rays cause the formation of electron-hole pairs in the glass. The electrons are then

primarily captured by the Sm^{3+}ions becoming Sm^{2+}ions with some of the electrons being captured by PO_n electron centers. The holes are captured by the POHCs. This process can be represented chemically as:

$$Sm^{3+} + e^- \rightarrow Sm^{2+}$$

and

$$PO + h^+ \rightarrow POHC$$

Table 4.1: The comparison of central wavelengths (λ), and central energies (E) of Gaussian absorption bands (G1-G5) observed in experiments with POHC data from Ebeling *et al.* [48]

Experiments			Values by Ebeling *et al.*				
Bands	λ (nm)	E (eV)	λ (nm)	E (eV)	Defect	Type	Structure[a]
G1	521±10	2.38±0.01	540	2.30±0.02	POHC	HC	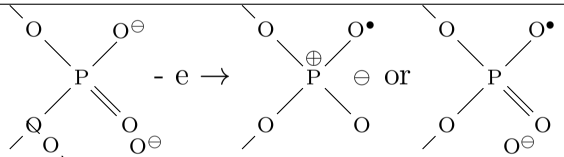
G2	430	2.88±0.03	430	2.89±0.04	POHC	HC	
G3	321	3.86±0.12	325	3.82±0.04	POHC	HC	
G4	190	6.5±0.1	210	5.90±0.06	PO_3	EC	
G5	240	5.16±0.05	240	5.12±0.06	PO_4	EC	
			265	4.68±0.08	PO_2	EC?	

[a] Symbols: (O) oxygen ion; (P) phosphorus ion; ($\oplus$) positive charge; ($\ominus$) negative charge; ($\bullet$) paramagnetic electron.

4.2.2 Electron Paramagnetic Resonance

While Sm^{3+}does contain a paramagnetic electron resulting in an EPR spectra [67] [68] [40] it is the spectra resulting from the paramagnetic centers of the X-ray induced effects that are of interest in this project. The aim of the EPR experiments is to help with the identification of the hole and electron centers that appear in the irradiated glass samples which was started in Section 4.2.1. This is accomplished by interpreting the experimental spectra using previously published work as a guide to identify the absorption bands [48] and comparing the results to the interpretation of the induced absorption spectra.

The EPR spectra analysis was a slightly more involved process than the analysis of the transmission spectra. First of all the frequency, ν, of the X-band microwave bridge is not entirely constant over from scan to scan so it is necessary to convert the x-axis values from magnetic field values to g-factor values. This can be done using the fundamental equation of electron paramagnetic resonance [69]:

$$g = \frac{h\nu}{\mu_B B_0} \tag{4.3}$$

where h is Planck's constant, μ_B is the Bohr magneton, and B_0 is the magnetic field. The frequency value is included in the spectra data file. Once all of the spectra have been converted to g-factors it is possible to compare the position of absorption peaks from different scans. The scans presented here have both g-factor and magnetic field values displayed on the x-axis. The g-factors were used to calculate new magnetic field values based on a set frequency choice of $\nu = 9.85$ GHz, which is within the operating range of the microwave bridge.

EPR spectra are recorded as the first derivative of an absorption spectra, so in order to properly assign a baseline to the spectra it is necessary to integrate the data. This was done numerically using a technique that set the intensity of the lowest g-factor value to zero and then the subsequent values were determined at each point x

using the relation:

$$I_{\text{integrated}}(x) = I_{\text{signal}}(x)[g(x-1) - g(x)] + I_{\text{integrated}}(x-1) \tag{4.4}$$

With the absorption spectra it is possible to fit a baseline. The chosen baseline was a cubic polynomial:

$$I_{\text{baseline}}(x) = A[I_{\text{int}}(x) - I_{\text{int}}(0)]^3 + B[I_{\text{int}}(x) - I_{\text{int}}(0)]^2 + C[I_{\text{int}}(x) - I_{\text{int}}(0)] \tag{4.5}$$

where A, B, and C are the fitting parameters. The results of this numerical integration and the fit of the baseline are shown in Figure 4.8 (a). Now that a baseline for the absorption spectrum has been determined it can be numerically differentiated so that it is a baseline for the experimental signal. The resulting baseline is shown with the experimental signal in Figure 4.8 (b). From this point it is trivial to subtract the baseline from the experimental signal to get the spectrum that will be analyzed.

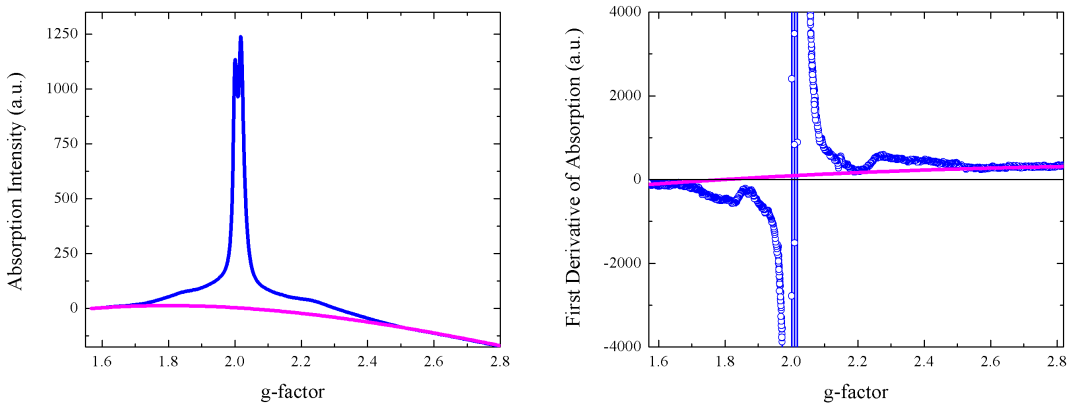

(a) (b)

Figure 4.8: (a) The numerically integrated signal intensity (blue) and the cubic polynomial baseline (pink) with $A = 58$, $B = -280$, and $C = 120$. (b) The experimental signal (blue) and the numerical derivative of the baseline from Equation 4.5 (pink).

The experimental signal was fit using a variety of Gaussian and Lorentzian functions. A good fit was found using four Lorentzians and six Gaussians that were numerically differentiated. The fit over the full signal intensity is shown in Figure 4.9 and the fit over the lower intensity peaks that are on the wings of the high intensity

main peaks is shown in Figure 4.10.

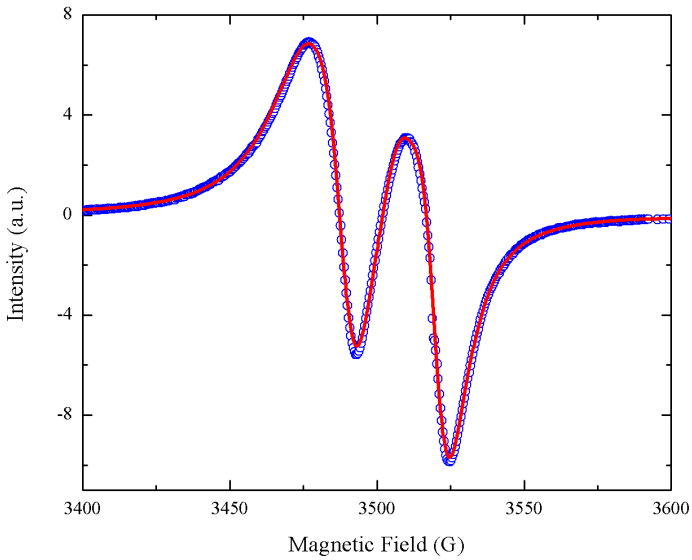

Figure 4.9: The full intensity of the EPR signal for a piece of FP glass containing 0.5% Sm^{3+}after it was irradiated for two hours in the Faxitron X-ray chamber (blue symbols). The red line is the approximation of the spectrum using differentiated Gaussians and Lorentzians.

By comparing the experimental spectrum to the spectra from Ebeling *et al* [48] it was possible to match the peaks from this experiment to those identified in that paper. The four Lorentzians appear to be two sets of doublets that simulate the POHC related EPR spectra. The six Gaussians appear to be three doublets simulating the EPR spectra of the PO_2, PO_3, and PO_4 electron centers. The labeled differentiated Gaussians and Lorentzians are shown with the experimental signal in Figure 4.11. The likely POHC and PO_n electron center identifications are labeled on the figure.

The strength of these identifications based on the appearance of the spectra can be improved by comparing the g_m values. The g_m value is the middle value between the g-factors of both lines of a doublet, ie $g_m = (g_1 + g_2)/2$. The g-factors from the simulation are the center peak values from the original Gaussians and Lorentzians. The g_m values from the simulation of the experimental data are compared to reference values in Table 4.2.

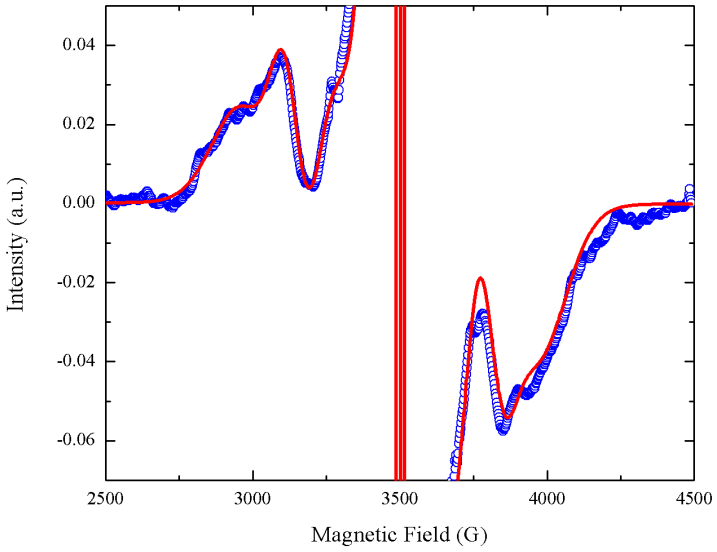

Figure 4.10: The low intensity wing peaks of the EPR signal for a piece of FP glass containing 0.5% Sm^{3+}after it was irradiated for two hours in the Faxitron X-ray chamber (blue symbols). The red line is the approximation of the spectrum using differentiated Gaussians and Lorentzians.

Table 4.2: The comparison of g_m values for POHCs and PO_ns from the simulation of the experimental EPR spectrum to the g_m values from Ebeling *et al.* [48]

Defect	Type	g_m values	
		Simulations of Experiments	Ebeling *et al*
POHC	HC	2.010 2.011	2.008±0.003
PO_4	EC	2.062	2.142±0.008
PO_3	EC	2.043	2.064±0.005
PO_2	EC?	2.041	2.006±0.003

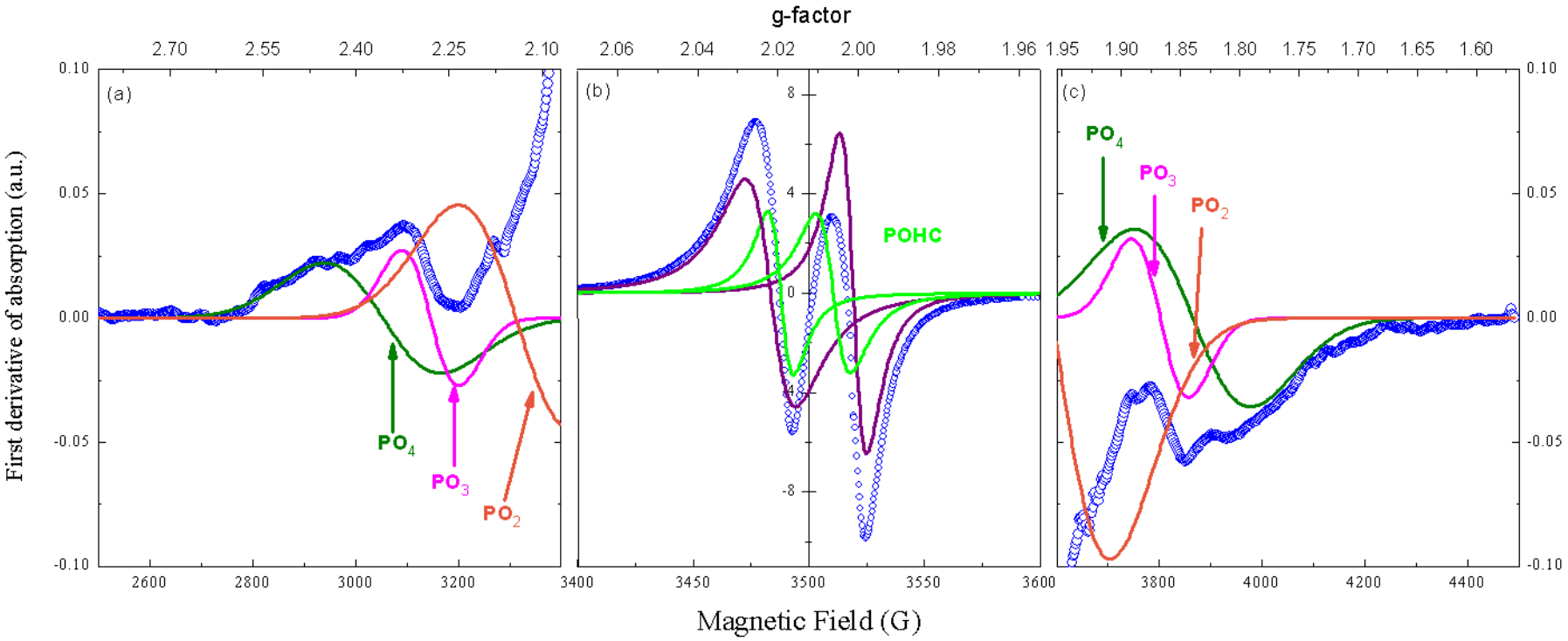

Figure 4.11: The EPR signal for a piece of FP glass containing 0.5% Sm^{3+}after it was irradiated for two hours in the Faxitron X-ray chamber (blue symbols). The individual differentiated Lorentzians used to simulate the POHCs related EPR signals, and the individual differentiated Gaussians used to simulate the EPR signals of the PO_2, PO_3, and PO_4 electron centers are shown as solid lines. The red fit line that approximates the experimental spectrum in Figures 4.9 and 4.10 is the sum of these differentiated Gaussians and Lorentzians.(note the different x and y scale for graph (b))

4.3 Dose Profile Curves

The over reaching goal of this project is the development of an X-ray dosimeter based on the conversion of the oxidation state of RE ions embedded in a glass host. The specific goal of this work is to characterize the conversion of $Sm^{3+} \rightarrow Sm^{2+}$ in fluorophosphate glass under X-ray irradiation. After exposure to the ionizing radiation the Sm^{3+} doped glass will contain some Sm^{2+} ions which have a different emission spectra than Sm^{3+}. Notably the appearance of emission bands around 683 and 725 nm in the irradiated glass samples. The intensity of these bands is proportional to the concentration of Sm^{2+} ions in the sample which is in turn proportional to the radiation dose. Thus it is possible to use the relative intensity of the Sm^{3+} and Sm^{2+} emission bands to determine the radiation dose.

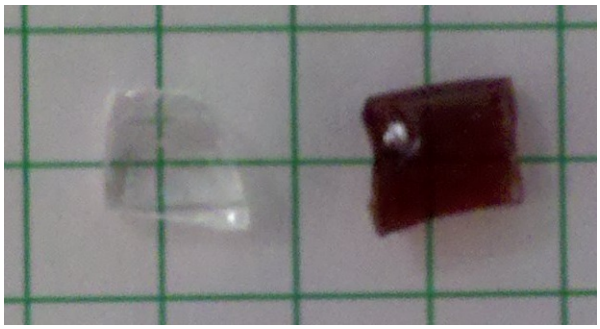

Figure 4.12: FP glass doped with 0.001% Sm^{3+} for dose profile experiments. Left: as prepared glass. Right: a sample irradiated for 5000s at the CLS with 3 Cu filters.The grid is 1 cm $\times$ 1 cm.

The photoluminescence area of interest for comparing the spectra of Sm^{3+} and Sm^{2+} is the range from 500 to 850 nm. However as can be seen in Figure 4.12 there is considerable X-ray induced absorbance in the optical range. From Section 4.2.1 it is clear that the absorbance within this range can be attributed to the absorption band G1 which is a POHC with a central energy of 2.38 and a width of 0.35 eV. This induced absorption can be represented as a function of wavelength using a Gaussian:

$$A(\lambda) = C_1 \exp\left(-\left(\frac{\frac{1240\text{eV nm}}{\lambda[\text{nm}]} - 2.38\text{ eV}}{0.35\text{ eV}}\right)^2\right) \tag{4.6}$$

where C_1 is a fitting parameter that changes with irradiation time to match the amplitude of the induced absorption band.

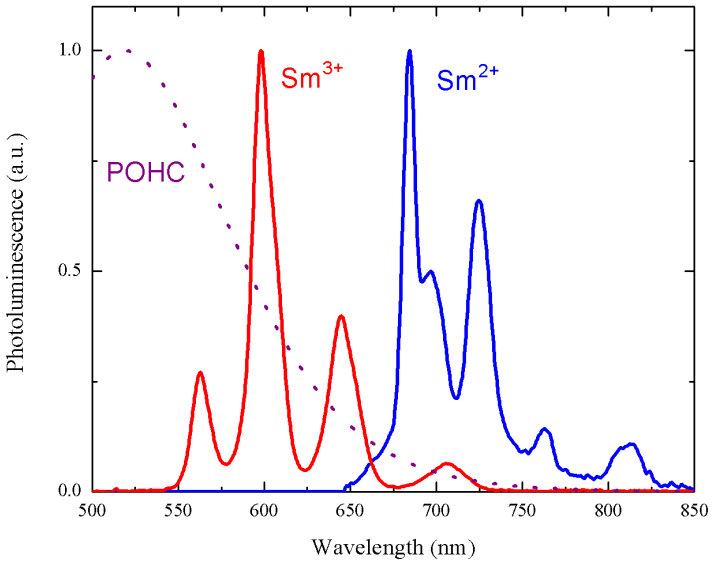

Figure 4.13: The normalized emission spectra for $Sm^{3+}$and Sm^{2+}as measured by the StellarNet EPP2000 spectrometer. The dashed line is the normalized induced absorption attributed to the POHC with a center energy of 2.38 eV.

So as long as this induced absorption is accounted for it is possible to simulate the experimental PL spectra using a combination of the emission spectra for $Sm^{3+}$and Sm^{2+}. The normalized spectrum for Sm^{3+}can be converted into a function $\Phi_{Sm^{3+}}(\lambda)$ where Φ is the intensity of the sample spectra at a specified wavelength, λ. Similarly, the spectrum of Sm^{2+}gives $\Phi_{Sm^{2+}}(\lambda)$. The spectra utilized for these functions and the induced absorption function are shown in Figure 4.13. Using these Sm emission functions and the induced absorption the experimental PL can be simulated as:

$$\Phi_{sim}(\lambda) = \frac{C_2\Phi_{Sm^{3+}}(\lambda) + C_3\Phi_{Sm^{2+}}(\lambda)}{10^{A(\lambda)}} \tag{4.7}$$

where C_2 and C_3 are adjustable fitting parameters that represent the intensity of the Sm emission bands. The induced absorbance is presented as an exponential of 10 because of the logarithmic relation it has with transmission (Equation 4.1). The

fitting was performed using the Solver package in Microsoft Excel.

This means that the denominator is equivalent to multiplying the strength of the emission bands by the induced decrease in transmission reducing the intensity of the spectra at the wavelengths where the transmission has decreased. The fit of these simulated spectra is shown for a variety or irradiation times in Figure 4.14 and the fitting parameter values for these spectra are listed in Table 4.3.

Table 4.3: The fitting parameters used in Equation 4.7 to simulate the spectra from Figure 4.14.

Irradiation Time (s)	C_1	C_2	C_3	$R(t)$
1	0.02	2576	6.25	2.43×10^{-3}
100	0.32	836	215	0.258
2000	0.82	596	844	1.29

For the creation of a dose profile curve the important terms are C_2 and C_3 as they represent the relative strength of the $Sm^{3+}$and Sm^{2+}emission peaks respectively. The ratio of these two terms

$$R(t) = \frac{C_3}{C_2} \tag{4.8}$$

can be used to characterize the degree of conversion of $Sm^{3+}\rightarrow Sm^{2+}$with irradiation time. Having the weighting factor for Sm^{3+}in the denominator is not a concern since the conversion stops before all of the $Sm^{3+}$is converted, even for very low initial concentrations of samarium. Plotting $R(t)$ vs irradiation time can provide information about the dose which is proportional to the exposure time. A plot of $R(t)$ vs irradiation time for samples with varying concentrations of Sm is shown in Figure 4.15.

The fit line from Figure 4.15 demonstrates that the ratio of $Sm^{2+}$to Sm^{3+}can be approximated using an exponential decay:

$$R(t) = R_0\left[1 - \exp(t/\tau)\right] \tag{4.9}$$

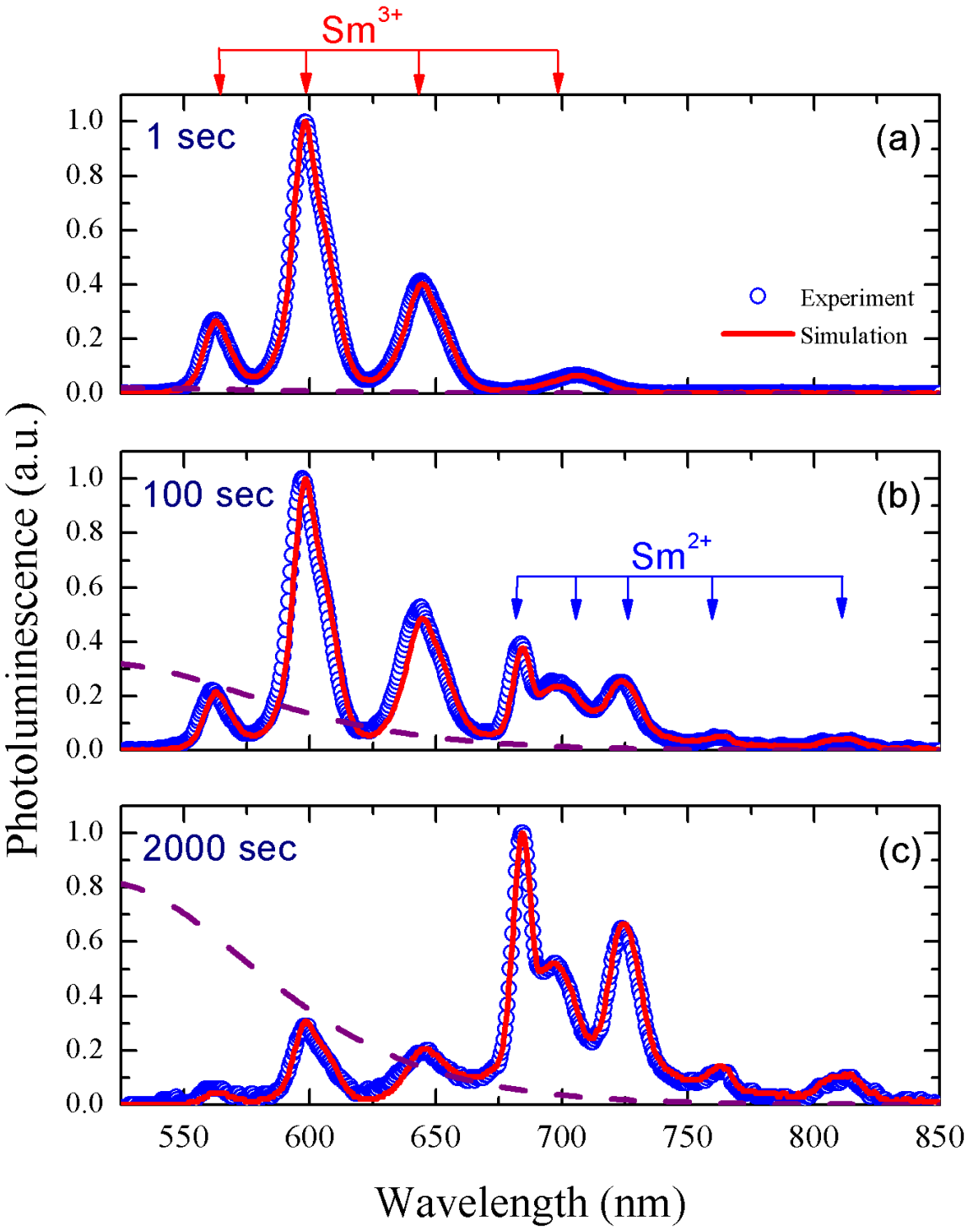

Figure 4.14: The evolution of PL spectra for a sample containing 0.1% Sm^{3+}under X-ray irradiation at the CLS with 3 Cu filters. The irradiation times were (a) 1 s, (b) 100 s, (c) 2000 s. The blue symbols are experimental data, the red line is the simulation from Equation 4.7 and the dashed line is the X-ray induced absorbance.

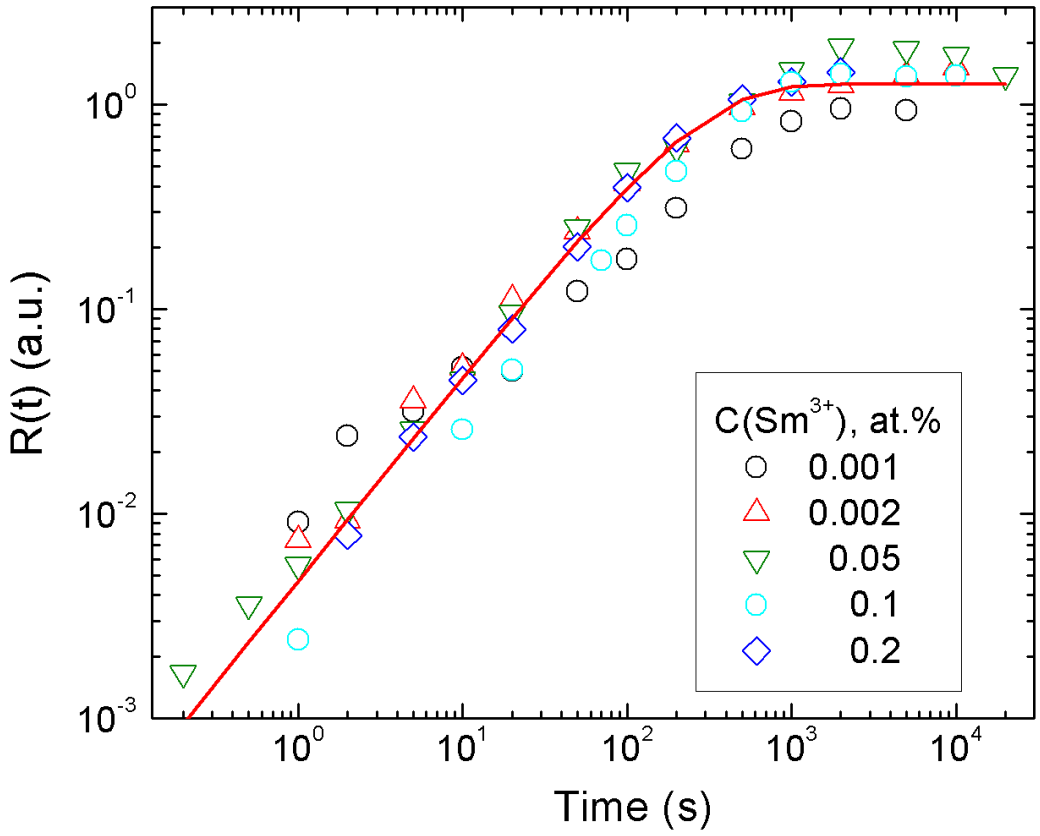

Figure 4.15: The ratio $R(t)$ for glasses with varying concentration of Sm versus irradiation time. The line is based on an exponential decay with τ ≈270 s and R_0 comparable to the ratio at which the conversion of $Sm^{3+} \rightarrow Sm^{2+}$saturates.

where τ ≈270 s and R_0 and τ do not appear to depend on Sm concentration.

As the conversion of $Sm^{3+} \rightarrow Sm^{2+}$has now been characterized in terms of irradiation time, the next step is to go from irradiation time to delivered dose. The maximum surface dose rate of the BMIT-BM beamline at the CLS with 3 Cu filters is 2 Gy/s in air, however the ring current is not constant. The flux of the X-ray photons at a bend magnet beamline at a synchrotron has a linear dependence on the ring current [70]:

$$\frac{d^2\dot{N}}{d\theta d\psi} = 1.327 \times 10^{13} E^2[\mathrm{GeV}] I[\mathrm{A}] H_2(\mathrm{y}) \quad \text{photons} \cdot \mathrm{s}^{-1} \cdot \mathrm{mr}^{-2}(0.1\%\mathrm{bw})^{-1} \qquad (4.10)$$

where E is the storage ring energy, I is the ring current, and H_2(y) is a ratio of the photon energy to the critical photon energy.

The absorbed dose is the energy deposited divided by the object mass and has a linear dependence the photon flux:

$$D(E_{ph}) = \frac{E_{ph} N_0}{\rho A t} \frac{\mu/\rho_{EA}}{\mu/\rho_T} \left[1 - \exp\left(-\frac{\mu}{\rho_T}\rho t\right)\right] \tag{4.11}$$

where N_0 is the number of incident photons of energy E_{ph}, μ/ρ_T is the total mass attenuation coefficient and μ/ρ_{EA} is the energy absorption coefficient. Since the dose is linearly dependent on the photon flux which is in turn linearly dependent on the ring current it is reasonable to recalculate the dose rate as a fraction of the maximum dose rate using the ratio of the average ring current during an exposure time to maximum ring current. The ring current decays exponentially after injection:

$$I_R(t) = I_R(0)\, e^{-t/\tau_{\mathrm{CLS}}} \tag{4.12}$$

where $I_R(t)$ is the ring current at the conclusion of an exposure t seconds long, $I_R(0)$ is the ring current at the start of the exposure and τ_{CLS}=104400 s at the CLS. Using this function it is easy to determine the average ring current during an irradiation time:

$$I_{R,\,\mathrm{average}}(t) = \frac{I_R(0)}{t-0} \int_0^t e^{-t/\tau_{\mathrm{CLS}}}\, \mathrm{d}t = \frac{I_R(0)\tau_{\mathrm{CLS}}}{t} \left[1 - e^{-t/\tau_{\mathrm{CLS}}}\right] \tag{4.13}$$

and the dose delivered during the irradiation time t can then be approximated by:

$$D(t) = \frac{t\, \dot{D}_{\max}\, I_{R,\,\mathrm{average}}(t)}{I_{R,\,\max}} \tag{4.14}$$

where the maximum dose rate $\dot{D}_{\max}$ is 2 Gy/s, and $I_{R,\,\max}$ is the maximum ring current which was 250 mA. Note that Equation 4.14 gives the tissue equivalent surface dose in air and is not equal to the dose absorbed by the sample. A plot of the Sm ratio versus delivered dose for a variety of Sm-doping concentrations is shown in Figure 4.16.

The red fit line shown in Figure 4.16 is the same exponential decay equation used to fit the $R(t)$ vs time plot (Equation 4.8) except with $\tau \approx 540$ Gy. It is evident from these results that the conversion efficiency depends almost linearly on the tissue equivalent surface dose in air up to ~150 Gy and saturates at doses exceeding ~1500 Gy. This indicates that it should be possible to use the Sm-doped FP glasses as an X-ray dosimeter with a dynamic range spanning three orders of magnitude into the kilo-Gray range.

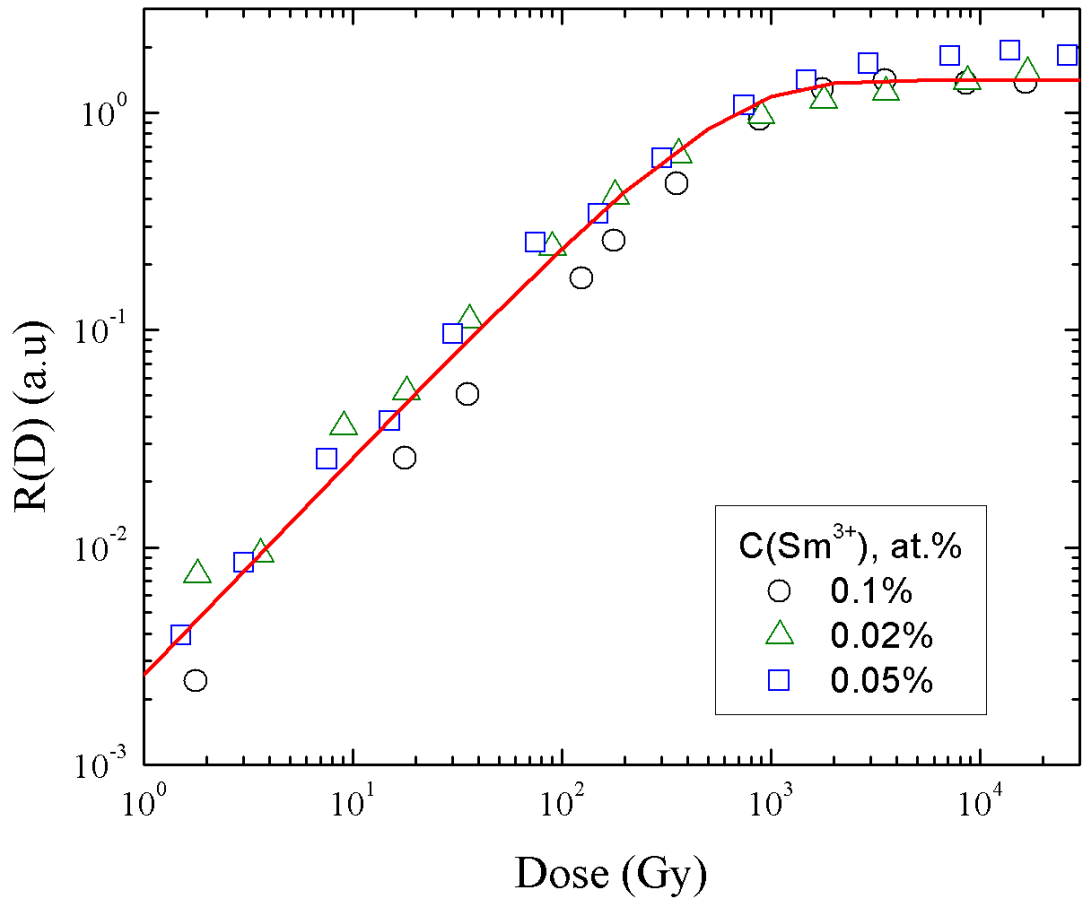

Figure 4.16: The ratio $R(D)$ for glasses with varying concentration of Sm versus the tissue equivalent surface dose based on the maximum surface dose rate of 2 Gy/s in air adjusted for decreasing ring current, R_c. The line is based on an exponential decay with $\tau \approx$540 Gy and R_0 comparable to the ratio at which the conversion of $Sm^{3+} \rightarrow Sm^{2+}$saturates.

4.4 Stability & Reusability

It is important to study the stability of the $Sm^{3+} \rightarrow Sm^{2+}$conversion as well as the other X-ray induced effects under exposure to light (photobleaching) for two reasons. The primary reason is that an optical laser is used to excite the $Sm^{3+}$and Sm^{2+}emissions that are characterized in Section 4.3 and used to determine the delivered X-ray dose so it is important to understand if there any changes in the sample resulting from exposure to this laser. The other reason is to test the reusability of the glass samples as a dosimeter. It would be economically beneficial if it was possible to use a sample as a dosimeter and then undo all of the X-ray induced effects by photobleachingthe sample and then be able to perform the same X-ray irradiation and recreate the same dose profile.

4.4.1 Photoluminescence

PL measurements are used to examine the effects of photobleachingon the Sm emission spectra and whether it is possible to re-use an irradiated sample after photobleachingto recreate the dose profile.

Samarium Conversion

The stability of the X-ray induced Sm^{2+}under illumination from excitation sources is important as it is the ratio of the Sm^{2+}emission signal to the Sm^{3+}emission signal that is being interpreted to determine delivered dose. As can be seen in the left side of Figure 4.17 under illumination with a 405 nm laser the signal strength of Sm^{2+}emission quickly decreases and after 100 minutes of photobleachingthese is essentially no trace of Sm^{2+}in the emission spectra. The right side of Figure 4.17 shows the change in PL spectra for a sample that is illuminated with a 532 nm laser of similar intensity. While it is clear that photobleachingwith the green laser also decreases the strength of the Sm^{2+}peaks, the strength of the effect is much lower.

Figure 4.18 shows the decrease in the ratio $R(t)$ with photobleachingtime for a variety of illumination sources. It is clear from the figure that the 405 nm laser

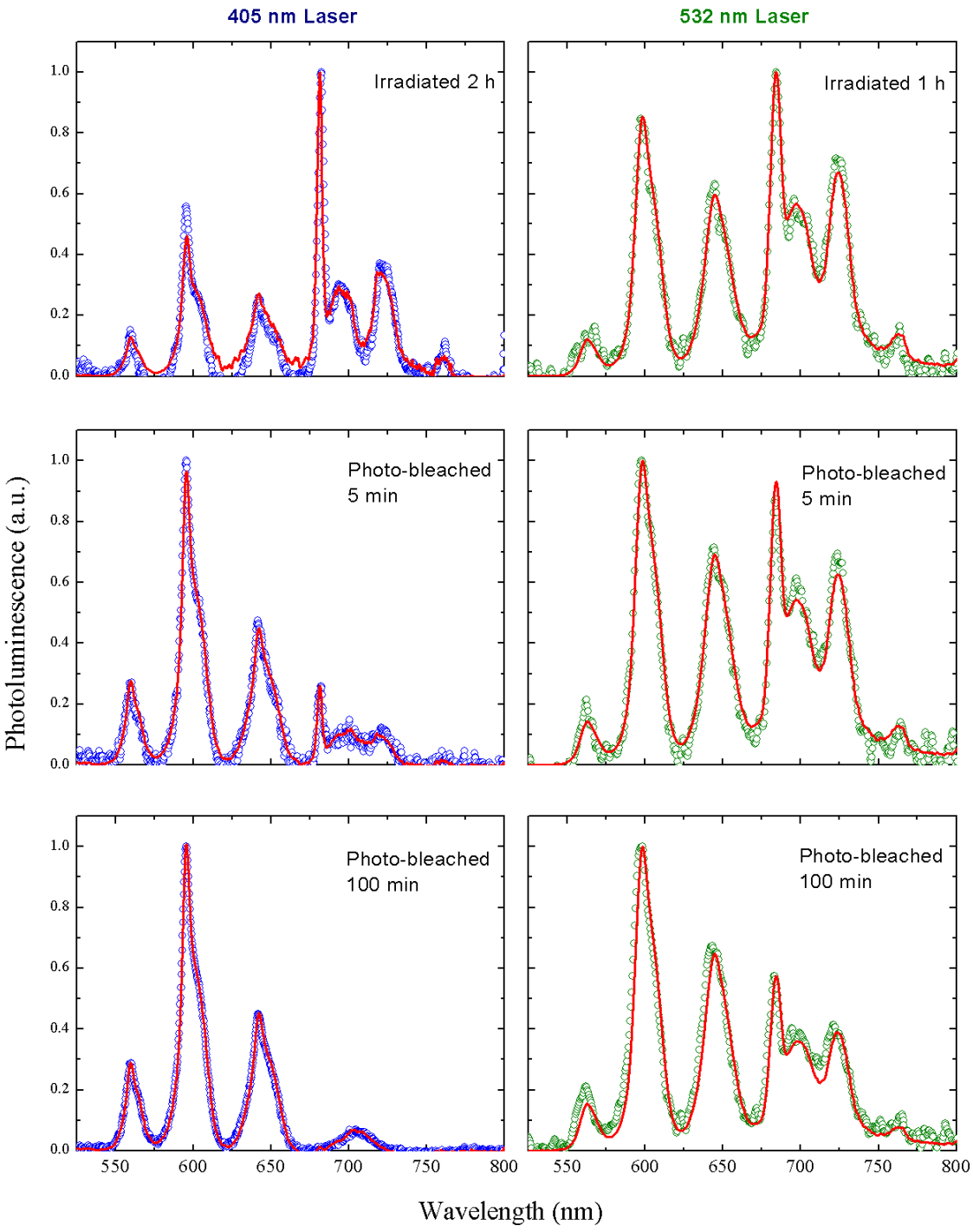

Figure 4.17: Left column: the evolution of the normalized PL emission for samples containing 0.5% Sm^{3+}after irradiation in the Faxitron X-ray chamber after photo-bleachingwith a 405 nm laser. Right column: photobleachingwith a 532 nm laser.

currently used to excite the irradiated samples to obtain the PL measurements used to determine dose undoes some of the measured Sm conversion. This could prove problematic for precision measurements of dose. It could be possible to decrease the photobleachingeffect by shortening excitation times, de-focusing the laser, or by placing an optical density filter between the excitation source and the sample.

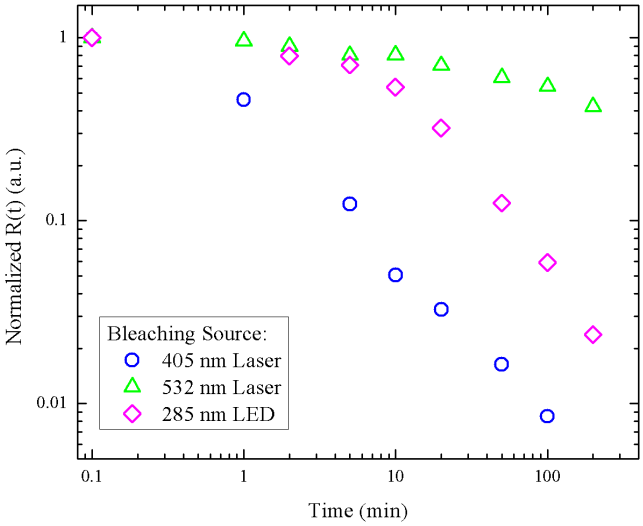

Figure 4.18: The change in $R(t)$ with photobleachingtime for three different light sources, a 405 nm laser, a 532 nm laser, and a 285 nm LED. Note that the ratios were normalized so that $R(0) = 1$ and that in this case $Time$ refers to photobleachingtime not irradiation time. From Table 3.1, the optical power of the light sources used was 27 mW for the 405 nm laser, 26 mW for the 532 nm laser, and 0.78 mW for the 285 nm LED.

Dose Profile Repeats

Since it was shown above that it is possible to undo at least some of the chemical conversion from $Sm^{3+} \rightarrow Sm^{2+}$it would be interesting to know if the dose profile curves from Section 4.3 are reproducible after photobleachingthe irradiated sample. To test this an "as prepared" sample was irradiated for a dose profile measurement and then bleached for 1 hour using a 254 nm UV lamp as described in Section 3.7. The sample was then placed back in the black box and a new set of dose profile curve measurements were performed. This process was repeated multiple times on the same

sample. The resulting dose profile curves are shown in Figure 4.19

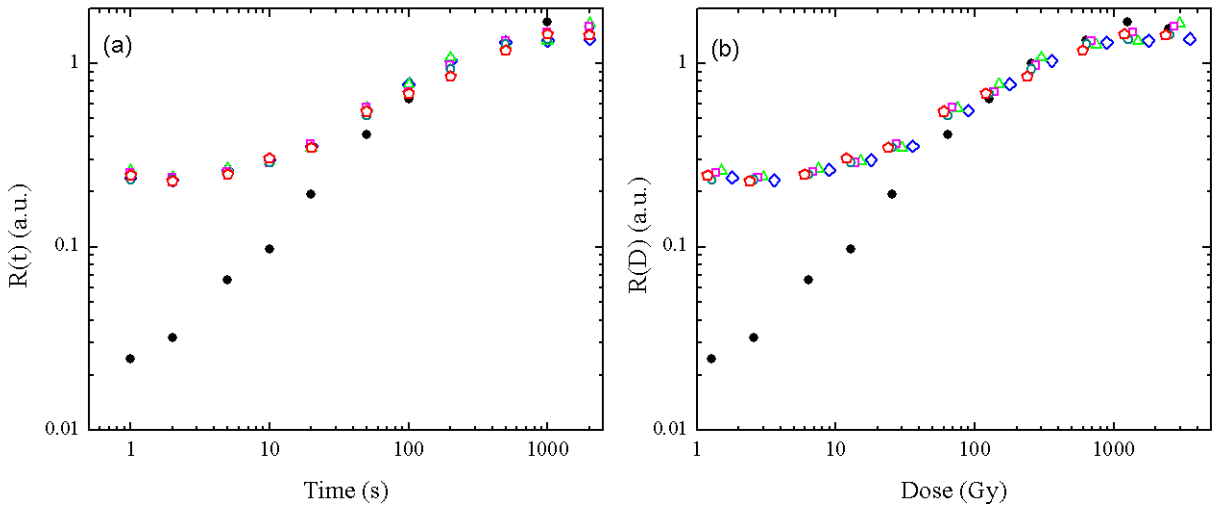

Figure 4.19: (a) the change in $R(t)$ for an "as prepared" sample containing 0.2% Sm^{3+}(black circles) and the $R(t)$ for the same sample after 1 hour of photobleaching-with a 254 nm UV lamp five times (coloured symbols). (b) the same data in terms of tissue equivalent surface dose, corrected for changes in ring current. All irradiations were performed consecutively at the CLS with 3 Cu filters.

It is clear from these results that the photobleachingwith this source did not completely re-convert the Sm^{2+}in the glass resulting in different initial values for $R(t)$ along with a different slope when compared to the as prepared sample. However at approximately 100 Gy the original and repeat $R(t)$ values are very close to each other and follow the same curve for the rest of the irradiation time. It is also clear that the five repeat exposures all result in very similar $R(t)$ values that follow the same progression with irradiation time and delivered dose. Based on these results it would appear that photobleachinga sample could make it reusable if it has already been exposed and the total exposure and bleaching times are kept relatively constant. However this is probably not an ideal solution to making a clinically reusable dosimeter and other methods such as annealing should be examined.

4.4.2 Changes in X-ray Induced Effects

Optical Absorbance

Changes in the optical absorbance of irradiated samples photobleached with a variety of different illumination sources were studied. The change in transmission spectra for photobleachingwith a 285 nm LED and a 405 nm laser are shown in Figure 4.20. The change in transmission spectra depicted for illumination with the 285 nm LED is similar to the results for illumination with a 315 nm LED and even less changes occurred when a 532 nm laser was used for photobleaching. Since the strongest changes were observed in samples illuminated with the 405 nm laser and because 405 nm is in one of the few optical ranges that excite both $Sm^{3+}$and Sm^{2+}, the photobleachinginduced changes resulting from a 405 nm laser will be the focus of this section and the section on EPR.

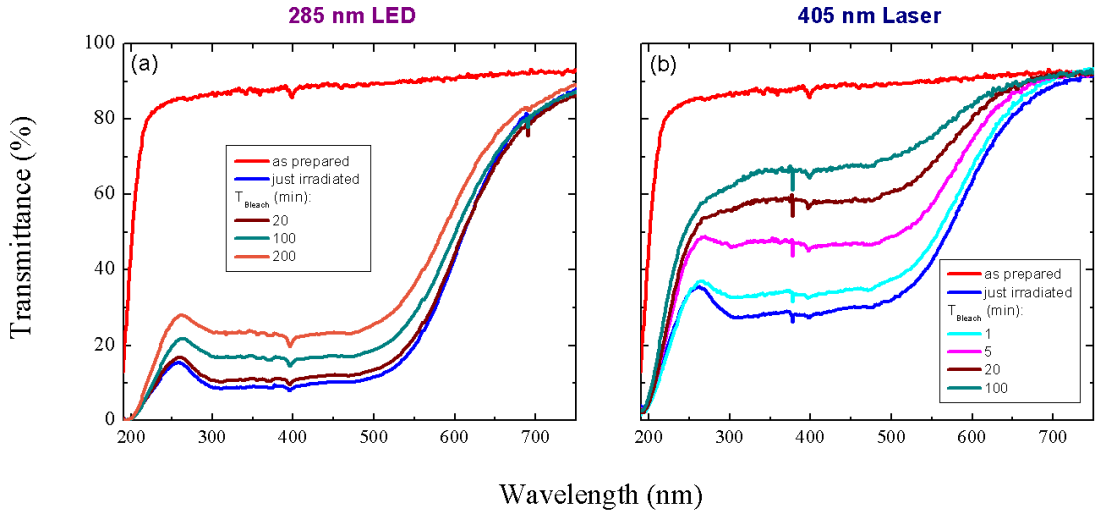

Figure 4.20: The effect of photobleachingwith (a) a 285 nm LED and (b) a 405 nm laser on the optical transmittance of samples containing 0.5% Sm^{3+}that were irradiated in the Faxitron X-ray chamber. From Table 3.1, the optical power was 0.20 mW for the 285 nm LED and 27 mW for the 405 nm laser.

It is evident from Figure 4.20 (b) that illumination with a 405 nm laser both increases the transmission in the UV and visible part of the spectrum but also results in a change in the shape of the transmission spectra. This change is examined in detail

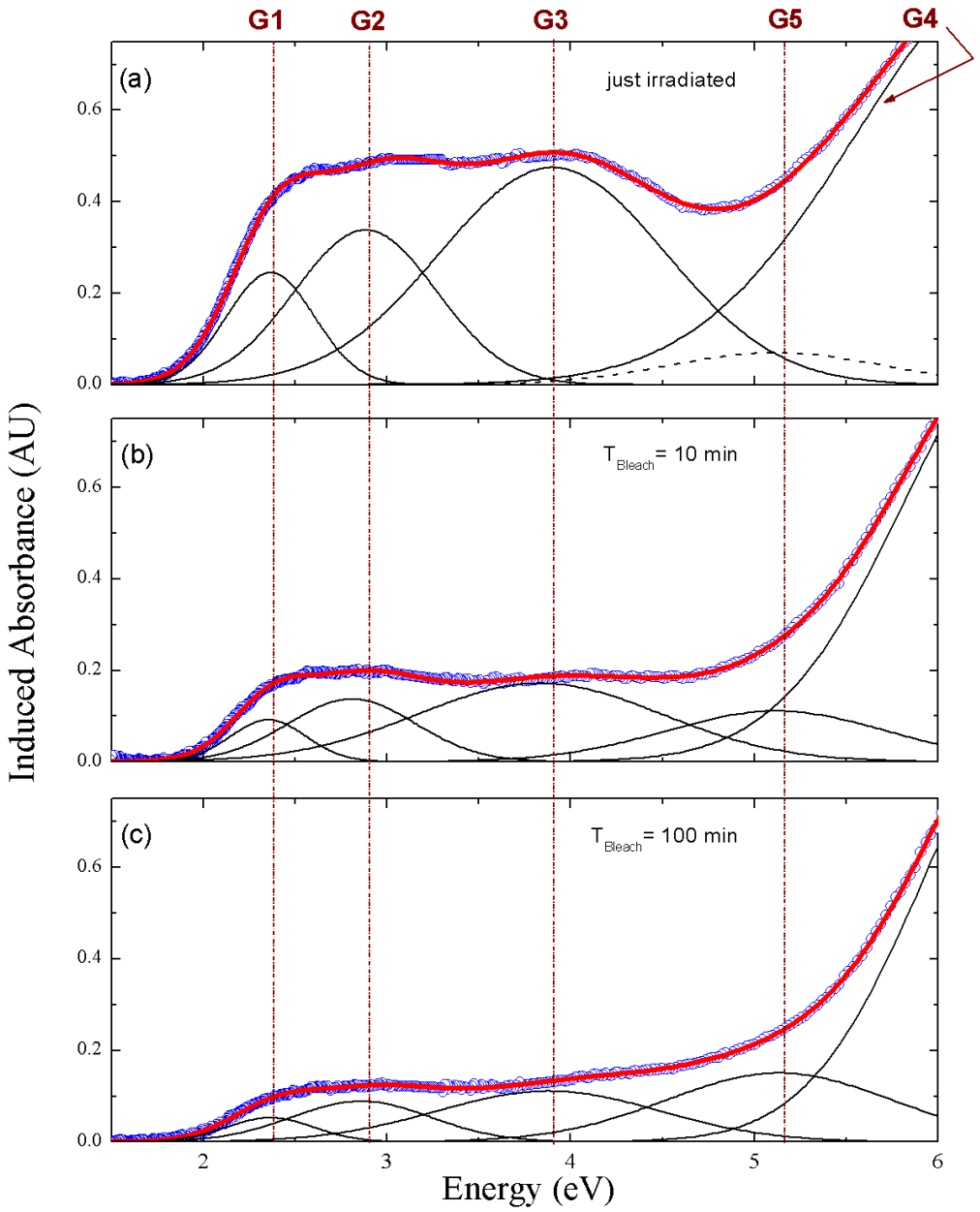

Figure 4.21: The evolution of X-ray induced absorbance during photobleachingwith a 405 nm laser in a sample containing 0.5% Sm^{3+}that had been irradiated in the Faxitron X-ray chamber. The experimental data (symbols) are approximated by a sum of Gaussians (red line). The individual Gaussians from G1-G5 are shown with thin black lines.

in terms of the evolution of the induced absorbance spectra with photobleachingtime in Figure 4.21. Just after irradiation the spectra can be simulated with four Gaussians G1-G4 just like the induced absorption spectra for irradiated Sm-doped glass in Figure

4.6. But as the sample is illuminated with the laser the overall intensity of the spectra decreases and the shape of the spectra changes. This change in the shape of the induced absorbance means that a fifth Gaussian G5 is required to simulate the spectra. Furthermore, as the photobleachingprogresses the intensity of this new band increases. This new band, G5 has the same central energy of the band G5 used to simulate the induced absorption spectra of irradiated, undoped FP glass as shown in Figure 4.6.

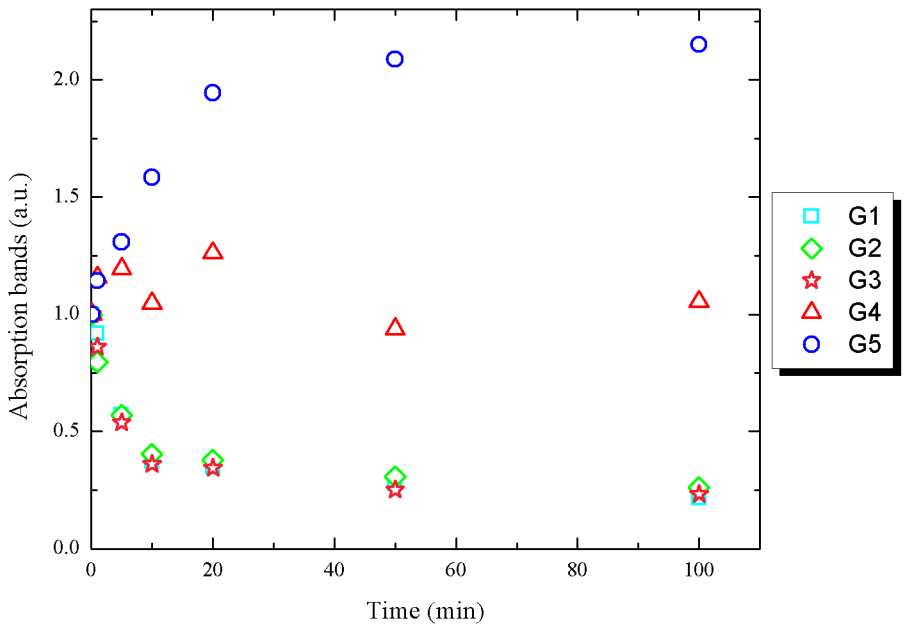

Figure 4.22: The change in the peak amplitude of the Gaussians G1-G5 as a function of photobleachingtime. The sample contained 0.5% $Sm^{3+}$and was irradiated in the Faxitron X-ray chamber. The amplitudes of all five Gaussians were normalized to a value of 1 after irradiation but before photobleaching. This representation shows that the peak intensities of Gaussians G1-G3 decreases, the peak intensity of G5 increases, and there is little change in the peak intensity of G4 with photobleachingtime.

Figure 4.22 shows the change in the amplitude of the Gaussians G1-G5 as a function of photobleachingtime. The three bands G1-G3 that were identified as POHCs in Section 4.2.1 all decrease in intensity with bleaching time while the band G5, which was identified as an electron center, increases in intensity with bleaching time.

This along with the decrease in Sm^{2+}emission signal intensity described in Section 4.4.1 suggests that photobleachingresults in the release of the electrons trapped by $Sm^{3+}$and the holes trapped by the POHCs. After they are freed from their respective traps some of the holes and electrons recombine but some of the electrons are instead trapped by the electron center G5. This would mean that it is not possible to completely remove all of the X-ray induced defects from the irradiated glass by photobleachingeven if all of the $Sm^{2+}$is reconverted to Sm^{3+}.

Electron Paramagnetic Resonance

For EPR measurements of photobleachingthe spectra were converted to g-factors, baselined and fit using Gaussians and Lorentzians as described in Section 4.2.2. The top half of Figure 4.23 shows the measured spectra for the sample just after irradiation and after a variety of bleaching times with a 405 nm laser. The bottom half of the figure is the numerically integrated spectra to make the changes in signal intensity easier to visualize. The identification of the various PO_n electron centers and POHCs is also shown on the figure.

The change in the amplitudes of the Gaussian and Lorentzian doublets used to simulate the experimental data are shown as a function of bleaching time in Figure 4.24. The amplitudes of the Lorentzians used to simulate the POHCs decreasing under illumination. The amplitude of the Gaussian doublet used to simulate PO_3 increases over the bleaching time and the amplitude of the PO_2 and PO_4 Gaussians is stable.

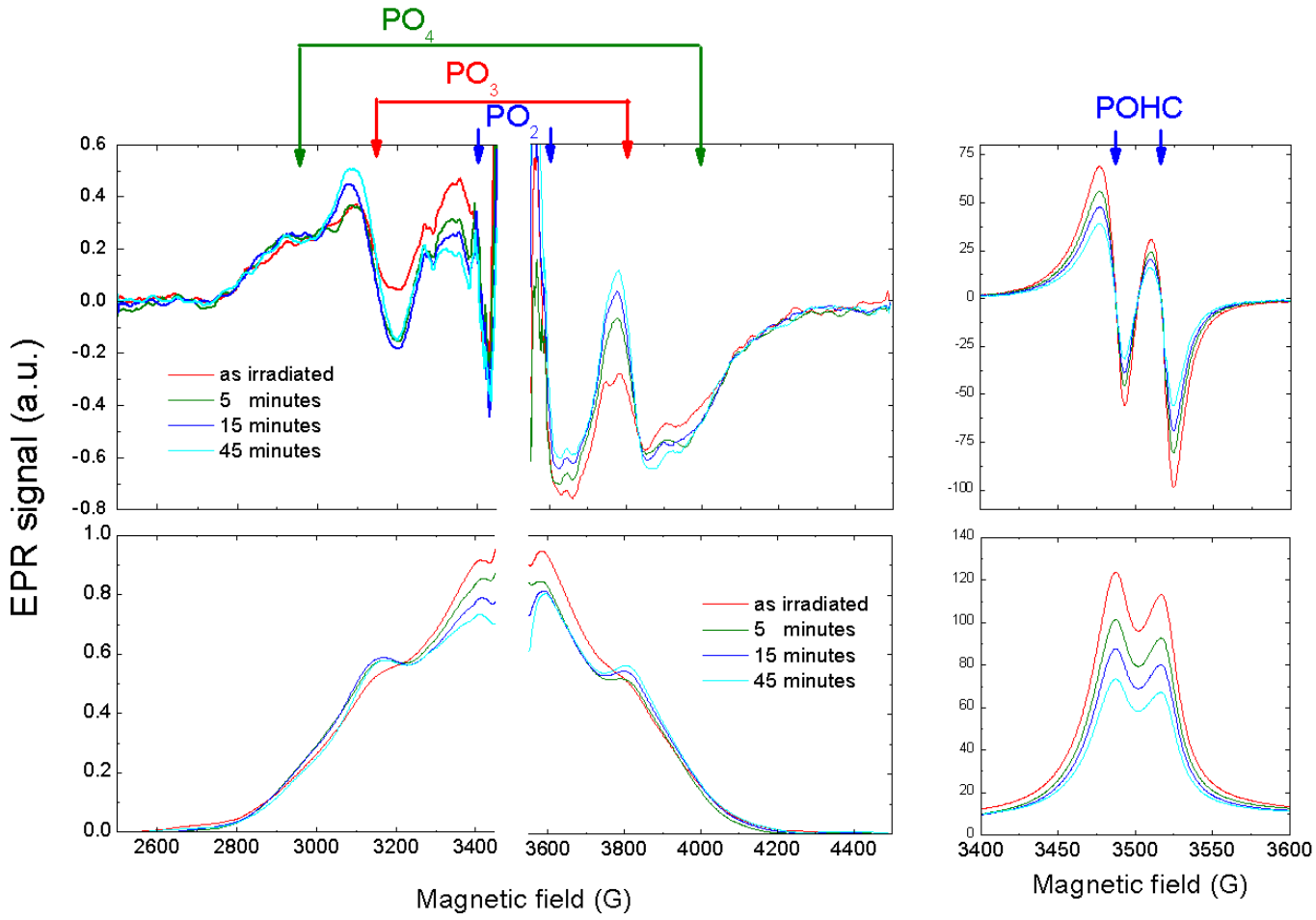

Figure 4.23: Top: the evolution of the measured EPR spectra with photobleachingtime. It can clearly be seen that the intensity of the POHCs peaks decreases with bleaching time and that amplitude of the peaks associated with the PO_3 EC increase with bleaching time. Bottom: a numerical integration of the EPR spectra to clearly demonstrate the changes in signal intensity with photobleaching, showing the decreased intensity of the peaks associated with the POHCs and the increase in signal intensity around the location of the PO_3 EC with bleaching time. The sample contained 0.5% Sm^{3+}, was irradiated in the Faxitron X-ray chamber, and was bleached using a 405 nm laser.

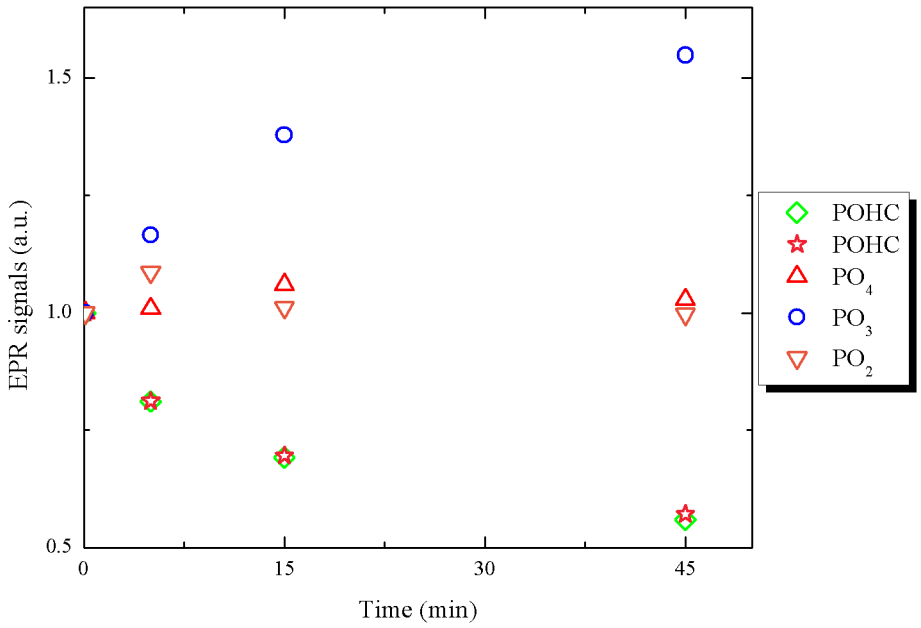

Figure 4.24: The change in the amplitudes of the Gaussians and Lorentzians that are used to simulate the EPR spectra after photobleachingwith a 405 nm laser. The sample contained 0.5% $Sm^{3+}$and was irradiated in the Faxitron X-ray chamber. The identification of the EPR lines is based on Figure 4.11. The peak amplitudes for the Gaussians and Lorentzians were all normalized to a value of 1 after irradiation but before photobleaching. This representation shows that peak intensities of the Lorentzians that represent the POHCs decrease, the peak intensities of the Gaussians that represent PO_3 increase, and the peak intensities of the Gaussians that represent PO_4 and PO_2 show little change with photobleachingtime.

Summary

Both optical absorbance and EPR measurements show a decrease in the amplitude of the Gaussians and Lorentzians simulating the POHCs and an increase in the amplitude of a Gaussian simulating an electron center. This indicates that even if photobleachingcould be used to reconvert all of the Sm^{2+}ions back to Sm^{3+}ions it could not be used to remove all of these X-ray induced effects in the glass.

The decrease in the amplitude of the Lorenztians used to simulate the POHCs mirror the decrease in amplitude of the Gaussian absorption bands G1-G3 under

Table 4.4: Identification of absorption bands G1-G5 based on changes in induced absorption and EPR spectra intensity caused by photobleachingwith a 405 nm laser.

	Induced Absorption		EPR
Band	Change in band amplitude	Defect[b]	Change in signal intensity
G1			
G2	↓	POHC	↓
G3			
G4	-	PO_4	-
		PO_2	-
G5	↑	PO_3	↑

[b]: Identification of the defects is based on g_m-values as shown in Table 4.2.

illumination. The increase in intensity of the Gaussian identified as PO_3 by its g_m value is very similar to the increase of absorption band G5 which had matched to PO_4 by the central energy of the band. The steady amplitude of the PO_2 and PO_4 EPR Gaussian matches the unchanging amplitude of the absorption band G4 which was matched to PO_3 by the central energy of the band. Since the simulation of the absorption spectra was performed utilizing the minimum number of Guassians required to fit the spectra and the EPR g_m values have a closer match between the simulation and experiment a new identification of the absorption bands G1-G5 is now presented to account for the changes in the amplitudes of the Gaussians and Lorentzians due to photobleaching. Bands G1-G3 are still considered to be POHCs, G4 is likely a combination of the absorption of PO_2 and PO_4 and G5 would then be absorption caused by PO_3. This revised identification of the X-ray induced effects and the changes in their intensities are summarized in Table 4.4

5. Summary and Conclusions

The objective of this project was to characterize the optical changes in X-ray irradiated fluorophosphate glass doped with trivalent samarium. This characterization was performed with the hope of being able to use a rare-earth doped glass or glass-ceramic plate as a valency conversion dosimeter for microbeam radiation therapy. Microbeam radiation therapy requires a detector with a large dynamic range that can be read with very high spatial resolution. Samarium was chosen as the rare-earth dopant because if it changed oxidation state from $Sm^{3+} \rightarrow Sm^{2+}$ under X-ray irradiation it would be easy to identify the change since the two ions have distinctive emission spectra with large easily identifiable peaks. Further more the strength of the peaks is proportional to the number of ions in the sample meaning it should be possible to measure the change in the relative strength of the peaks during irradiation.

The excitation spectra of both Sm^{3+} and Sm^{2+} ions was measured for the FP glass host. The results showed that there are two overlapping excitation regions in the visible spectrum where it is possible to excite both ions, one is around 405 nm and the other is around 470 nm. Both of these regions are significantly removed from the emission spectra of the ions that the excitation source should not obscure the reading of the spectra.

Low temperature emission spectra were also measured for Sm^{2+} in the FP glass over a range from 200 to 12 K. These experiments showed that signal intensity increases with decreasing temperature which could be useful for improving the signal-to-noise ratio when making high precision measurements of the PL of an irradiated sample. The low temperature experiments also showed that there is no change in the

number or position of the emission peaks with temperature so if samples were read at low temperatures no changes to how the data is processed would be necessary.

Optical transmission measurements showed that there is large increase in the absorption of the glass after irradiation in the visible and UV region. This X-ray induced absorption was simulated using a sum of Gaussians. The induced absorption in the Sm-doped glass required four Gaussians (G1-G4) to simulate the spectra. By comparing the central energies of these Gaussians to the central energies of identified absorption bands in irradiated FP glasses it was determined that three of these absorption bands are POHCs and one of them is a PO_n electron center. The amplitude of these Gaussians increases with irradiation time following an exponential decay $x(t) = x_0[1 - \exp(t/\tau)]$ until saturation.

The formation of these hole centers along with the conversion of $Sm^{3+} \rightarrow Sm^{2+}$ under X-ray irradiation suggests that the X-rays cause the formation of electron-hole pairs in the glass. The electrons are then primarily captured by the Sm^{3+} ions becoming Sm^{2+} ions with some of the electrons being captured by a PO_n electron center. The holes are captured by the POHCs. This process can be represented chemically as $Sm^{3+} + e^- \rightarrow Sm^{2+}$ and $PO + h^+ \rightarrow POHC$.

EPR spectra of the irradiated glass were measured and analyzed to verify the identification of of POHC and PO_n electron centers within the irradiated glass. The signal was interpreted by simulating the spectra using two Lorentzian doublets and three Gaussian doublets, all differentiated. The center of both bands for each doublets were then used to determine the middle g-values, g_m, which were then matched to published g_m values for defects in irradiated FP glass. Based on this analysis the EPR spectra for the Sm-doped FP glasses has peaks matched to POHCs and the electron centers PO_2, PO_3, and PO_4.

The conversion of $Sm^{3+} \rightarrow Sm^{2+}$ was examined in detail in terms of irradiation time and delivered dose. The PL spectra containing peaks from both Sm^{3+} and Sm^{2+} emission was interpreted by simulating the spectra using the normalized emis-

sion spectra of just $Sm^{3+}$and just Sm^{2+}. The PL spectra can then be simulated using these spectra as functions where the intensity is dependent on wavelength: $\Phi_{sim}(\lambda) = [C_2\Phi_{Sm^{3+}}(\lambda) + C_3\Phi_{Sm^{2+}}(\lambda)]A(\lambda)$ where C_2 and C_3 are the fitting parameters and $A(\lambda)$ is an added term to account for the X-ray induced absorption in this region caused by one of the POHCs. The conversion is then expressed as the ratio of the signal strength of $Sm^{2+}$and Sm^{3+}expressed as: $R(t) = C_3/C_2$. The dose profile curves were created by plotting R versus irradiation time and the delivered dose. From these plots it is apparent that the samarium conversion follows an exponential decay similar to the one followed by the amplitudes of the POHCs with irradiation time: $R(t) = R_0[1 - \exp(t/\tau)]$. It is evident from these dose profile curves that the conversion efficiency depends almost linearly on the tissue equivalent surface dose up to ∼150 Gy and saturates at surface doses exceeding ∼1500 Gy. This indicates that it should be possible to use the Sm-doped FP glasses as an X-ray dosimeter with a dynamic range spanning three orders of magnitude into the kilo-Gray range.

The stability of these X-ray induced effects under illumination was then tested. Exposure to UV and some optical light sources including the 405 nm laser used to excite the PL spectra for dose profile measurements caused a reconversion of $Sm^{2+} \rightarrow Sm^{3+}$. This means that in order to determine a precise dose which is required for radiotherapy the exposure times must be kept short and the excitation laser should be defocused or have an optical density filter placed in front of it decrease its intensity.

Since it is possible to use photobleachingto undo the Sm conversion the ability to reuse an irradiated sample to recreate the dose profile curves was examined. The illumination source was not able to completely reconvert all of the Sm^{2+}in the allotted bleaching time, meaning that the dose profile curves for the repeat exposures did not start at the same $R(t)$ value as the original curve. However the repeated curves did all start at the same $R(t)$ value and had the same increases in $R(t)$ with irradiation time. The repeat curves also saturated at the same $R(t)$ value and irradiation time as the original dose profile curve. Based on these results it would appear that photobleachinga sample could make it reusable if it has already been exposed and the total

exposure and bleaching times are kept relatively constant. However this is probably not an ideal solution to making a clinically reusable dosimeter and other methods should be examined.

The affect of photobleachingon the X-ray induced defects in the glass was also examined. Both optical absorbance and EPR measurements show a decrease in the amplitude of the Gaussians and Lorentzians simulating the POHCs and an increase in the amplitude of a Gaussian simulating an electron center. This indicates that even if photobleachingcould be used to reconvert all of the Sm^{2+}ions back to Sm^{3+}ions it could not be used to remove all of these X-ray induced effects in the glass.

The changes in the amplitudes of the functions used to simulate the induced absorbance and EPR spectra further helped with identification of the defects. The decrease in the amplitude of the Lorenztians used to simulate the POHCs mirror the decrease in amplitude of the Gaussian absorption bands G1-G3 under illumination. The increase in intensity of the Gaussian identified as PO_3 by its g_m value is very similar to the increase of absorption band G5. The steady amplitude of the PO_2 and PO_4 EPR Gaussian matches the unchanging amplitude of the absorption band G4 which indicates that the band is likely a combination of the absorption of these electron centers.

The following points are suggested as possible future experiments related to this project:

1. Perform dose profile experiments using the Biomedical Imaging and Therapy Insertion Device (BMIT-ID) beamline at the CLS. The insertion device beamline has much higher energy X-rays and a greater X-ray flux than the bend magnet beamline. It is the beamline which MRT would actually be performed with in the future and it would be beneficial to know how effective the samples are as a dosimeter when they are exposed to very large doses in a very short time.

2. Perform these experiments on samples with very high concentrations of samar-

ium to determine if the $Sm^{3+} \rightarrow Sm^{2+}$conversion saturation limit is determined by the concentration of samarium or the amount of POHCs available in the glass.

3. Examine the affect of annealing irradiated samples both above and below the glass transition temperature.

4. Perform high precision dose profile measurements of the samples using a modified confocal microscope to determine just how accurately doses can be determined.

5. Use X-ray fluorescent mapping to determine the distribution of the samarium ions across the surface of the samples to ensure it is consistent when reading PVDRs after irradiation through a collimator.

A. Term symbol

In this thesis the electronic transitions between energy levels of samarium ions are represented with Term symbols. These Term symbols are a shorthand representation of the angular momentum quantum numbers for a multi-electron atom. The use of these Term symbols assumes Russell-Saunders coupling, also know as LS-coupling. LS-coupling usually occurs in light atoms and is the result of the electron spins s_i interacting with each other to form a total spin angular momentum **S**. Similarly, the orbital angular momentum l_i of the electrons couple together to give the total orbital angular momentum **L**. **L** and **S** also couple together to form the total angular momentum **J**. This coupling or angular momentum is represented with vectors in Figure A.1.

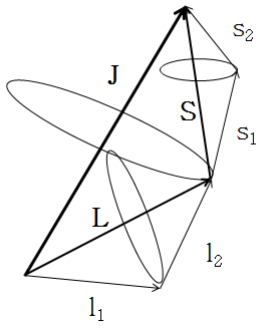

Figure A.1: A vector representation of the LS-coupling scheme of angular momentum for a two electron system. **L** and **S** precess around **J** at a slower rate than l_1 and l_2 precess around **L** and s_1 and s_2 precess around **S**.

The Russell-Saunders Term symbol takes the form:

$$^{2\mathbf{S}+1}\mathbf{L_J} \tag{A.1}$$

where **S** is the total spin angular momentum and 2**S**+1 is called the spin multiplicity which represents the maximum number of different states of **J** that are possible for that **LS** combination. **L** is the total orbital angular momentum and is expressed in spectroscopic notation where 0, 1, 2, 3...=S, P, D, F... and **J** is the total angular momentum which has the values of **J**=$|L-S|$, $|L-S|+1$, ..., $L+S$ [71].

For the special case of ground configurations of equivalent electrons the orbital and spin angular momentum of the lowest-energy Term follows some empirical rules, called Hund's Rules [72]. However, in the case of $Sm^{3+}$and $Sm^{2+}$the electrons are not in a ground state configuration and there is no empirical method for determining the placement of the electrons within their orbitals. Figure A.2 and Figure A.3 show possible electron configurations that have Term symbols matching the $^4G_{5/2} \rightarrow ^6H_{5/2}$ transition in $Sm^{3+}$and the $^5D_0 \rightarrow ^7F_0$ transition in Sm^{2+}.

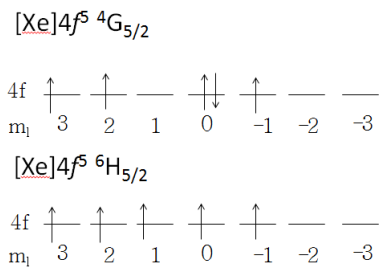

Figure A.2: A possible electron configuration that results in Term symbols that match the $^4G_{5/2} \rightarrow ^6H_{5/2}$ transition in Sm^{3+}.

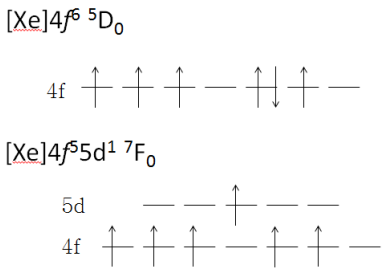

Figure A.3: A possible electron configuration that results in Term symbols that match the $^5D_0 \rightarrow ^7F_0$ transition in Sm^{2+}.

References

[1] W. C. Röntgen, "On a new kind of rays," *Science*, vol. 3, no. 59, pp. pp. 227–231, 1896.

[2] E. B. Podgorsak, *Radiation Physics for Medical Physicists*. Berlin Heidelberg: Springer-Verlag, 2006.

[3] D. N. Slatkin, P. Spanne, F. A. Dilmanian, and M. Sandborg, "Microbeam radiation therapy," *Medical Physics*, vol. 19, no. 6, pp. 1395–1400, 1992.

[4] J. C. Crosbie, I. Svalbe, S. M. Midgley, N. Yagi, P. A. W. Rogers, and R. A. Lewis, "A method of dosimetry for synchrotron microbeam radiation therapy using radiochromic films of different sensitivity," *Physics in Medicine and Biology*, vol. 53, no. 23, p. 6861, 2008.

[5] E. Brauer-Krisch, A. Rosenfeld, M. Lerch, M. Petasecca, M. Akselrod, J. Sykora, J. Bartz, M. Ptaszkiewicz, P. Olko, A. Berg, M. Wieland, S. Doran, T. Brochard, A. Kamlowski, G. Cellere, A. Paccagnella, E. A. Siegbahn, Y. Prezado, I. Martinez-Rovira, A. Bravin, L. Dusseau, and P. Berkvens, "Potential high resolution dosimeters for mrt," *AIP Conference Proceedings*, vol. 1266, no. 1, pp. 89–97, 2010.

[6] C. Kennedy and A. Dilmanian, "Prospects for microbeam radiation therapy of brain tumours in children," *Developmental Medicine & Child Neurology*, vol. 49, no. 8, pp. 566–566, 2007.

[7] Y. Prezado, I. Martinez-Rovira, and M. Sanchez, "Scatter factors assessment in microbeam radiation therapy," *Medical Physics*, vol. 39, no. 3, pp. 1234–1238, 2012.

[8] D. Slatkin, H. Blattmann, H. Wagner, M. Glotzer, and J. Laissue, "Prospects

for microbeam radiation therapy of brain tumours in children," *Developmental Medicine & Child Neurology*, vol. 51, no. 2, pp. 163–163, 2009.

[9] E. Brauer-Krisch, H. Requardt, T. Brochard, G. Berruyer, M. Renier, J. A. Laissue, and A. Bravin, "New technology enables high precision multislit collimators for microbeam radiation therapy," *Review of Scientific Instruments*, vol. 80, no. 7, p. 074301, 2009.

[10] P. Suortti and W. Thomlinson, "Medical applications of synchrotron radiation," *Physics in Medicine and Biology*, vol. 48, no. 13, p. R1, 2003.

[11] G. Belev, G. Okada, D. Tonchev, C. Koughia, C. Varoy, A. Edgar, T. Wysokinski, D. Chapman, and S. Kasap, "Valency conversion of samarium ions under high dose synchrotron generated x-ray radiation," *physica status solidi (c)*, vol. 8, no. 9, pp. 2822–2825, 2011.

[12] M. Torikoshi, Y. Ohno, N. Yagi, K. Umetani, and Y. Furusawa, "Dosimetry for a microbeam array generated by synchrotron radiation at spring-8," *European Journal of Radiology*, vol. 68, pp. S114 – S117, 2008.

[13] J. A. Laissue, H. Blattmann, M. D. Michiel, D. N. Slatkin, N. Lyubimova, R. Guzman, W. Zimmermann, S. Birrer, T. Bley, P. Kircher, R. Stettler, R. Fatzer, A. Jaggy, H. Smilowitz, E. Brauer, A. Bravin, G. L. Duc, C. Nemoz, M. Renier, W. C. Thomlinson, J. Stepanek, and H.-P. Wagner, "Weanling piglet cerebellum: a surrogate for tolerance to mrt (microbeam radiation therapy) in pediatric neuro-oncology," vol. 4508, pp. 65–73, SPIE, 2001.

[14] F. A. Dilmanian, P. Romanelli, Z. Zhong, R. Wang, M. E. Wagshul, J. Kalef-Ezra, M. J. Maryanski, E. M. Rosen, and D. J. Anschel, "Microbeam radiation therapy: Tissue dose penetration and bang-gel dosimetry of thick-beams' array interlacing," *European Journal of Radiology*, vol. 68, pp. S129 – S136, 2008.

[15] J. A. Laissue, G. Geiser, P. O. Spanne, F. A. Dilmanian, J.-O. Gebbers, M. Geiser, X.-Y. Wu, M. S. Makar, P. L. Micca, M. M. Nawrocky, D. D. Joel,

and D. N. Slatkin, "Neuropathology of ablation of rat gliosarcomas and contiguous brain tissues using a microplanar beam of synchrotron-wiggler-generated x rays," *International Journal of Cancer*, vol. 78, no. 5, pp. 654–660, 1998.

[16] F. Dilmanian, Y. Qu, S. Liu, C. Cool, J. Gilbert, J. Hainfeld, C. Kruse, J. Laterra, D. Lenihan, M. Nawrocky, G. Pappas, C.-I. Sze, T. Yuasa, N. Zhong, Z. Zhong, and J. McDonald, "X-ray microbeams: Tumor therapy and central nervous system research," *Nuclear Instruments and Methods in Physics Research Section A: Accelerators, Spectrometers, Detectors and Associated Equipment*, vol. 548, pp. 30 – 37, 2005.

[17] J. C. Crosbie, R. L. Anderson, K. Rothkamm, C. M. Restall, L. Cann, S. Ruwanpura, S. Meachem, N. Yagi, I. Svalbe, R. A. Lewis, B. R. Williams, and P. A. Rogers, "Tumor cell response to synchrotron microbeam radiation therapy differs markedly from cells in normal tissues," *International Journal of Radiation Oncology*Biology*Physics*, vol. 77, no. 3, pp. 886 – 894, 2010.

[18] S. D. Oves, K. R. Hogstrom, K. Ham, E. Sajo, and J. P. Dugas, "Dosimetry intercomparison using a 35-kev x-ray synchrotron beam," *European Journal of Radiology*, vol. 68, pp. S121 – S125, 2008.

[19] A. N.-R. Chair, C. R. Blackwell, B. M. Coursey, K. P. Gall, J. M. Galvin, W. L. McLaughlin, A. S. Meigooni, R. Nath, J. E. Rodgers, and C. G. Soares, "Radiochromic film dosimetry: Recommendations of aapm radiation therapy committee task group 55," *Medical Physics*, vol. 25, no. 11, pp. 2093–2115, 1998.

[20] N. Nariyama, T. Ohigashi, K. Umetani, K. Shinohara, H. Tanaka, A. Maruhashi, G. Kashino, A. Kurihara, T. Kondob, M. Fukumoto, and K. Ono, "Spectromicroscopic film dosimetry for high-energy microbeam from synchrotron radiation," *Applied Radiation and Isotopes*, vol. 67, no. 1, pp. 155 – 159, 2009.

[21] J. Bartz, G. Sykora, E. Bruer-Krisch, and M. Akselrod, "Imaging and dosimetry of synchrotron microbeam with aluminum oxide fluorescent detectors," *Radiation Measurements*, vol. 46, no. 12, pp. 1936 – 1939, 2011.

[22] T. Ackerly, J. C. Crosbie, A. Fouras, G. J. Sheard, S. Higgins, and R. A. Lewis, "High resolution optical calorimetry for synchrotron microbeam radiation therapy," *Journal of Instrumentation*, vol. 6, no. 03, p. P03003, 2011.

[23] A. A. Rahman, D. Bradley, S. Doran, B. Thierry, E. Bruer-Krisch, and A. Bravin, "The thermoluminescence response of ge-doped silica fibres for synchrotron microbeam radiation therapy dosimetry," *Nuclear Instruments and Methods in Physics Research Section A: Accelerators, Spectrometers, Detectors and Associated Equipment*, vol. 619, pp. 167 – 170, 2010.

[24] K. Son, H. Jung, S. H. Shin, H.-H. Lee, M.-S. Kim, Y. H. Ji, and K. B. Kim, "Evaluation of the dosimetric characteristics of a radiophotoluminescent glass dosimeter for high-energy photon and electron beams in the field of radiotherapy," *Radiation Measurements*, vol. 46, no. 10, pp. 1117 – 1122, 2011.

[25] Z. Liu, T. Massil, and H. Riesen, "Spectral hole-burning properties of sm2+ ions generated by x-rays in bafcl: Sm3+ nanocrystals," *Physics Procedia*, vol. 3, no. 4, pp. 1539 – 1545, 2010.

[26] C. Koughia, A. Edgar, C. R. Varoy, G. Okada, H. von Seggern, G. Belev, C.-Y. Kim, R. Sammynaiken, and S. Kasap, "Samarium-doped fluorochlorozirconate glass-ceramics as red-emitting x-ray phosphors," *Journal of the American Ceramic Society*, vol. 94, no. 2, pp. 543–550, 2011.

[27] A. Edgar, C. Varoy, C. Koughia, D. Tonchev, G. Belev, G. Okada, S. Kasap, H. von Seggern, and M. Ryan, "Optical properties of divalent samarium-doped fluorochlorozirconate glasses and glass ceramics," *Optical Materials*, vol. 31, no. 10, pp. 1459 – 1466, 2009.

[28] C. Koughia, G. Okada, D. Tonchev, S. Kasap, A. Edgar, C. R. Varoy, and H. von Seggern, "Optical and selected thermal properties of samarium-doped fluorochlorozirconate (fcz) glass-ceramics: Formation and growth of bacl2 nanocrystals in fcz glass-ceramics," *Journal of Non-Crystalline Solids*, vol. 357, pp. 2272 – 2277, 2011.

[29] S. O. Kasap, *Optoelectronics and Photonics: Principles and Practices*. Upper Saddle River, New Jersey: Prentice-Hall, 2001.

[30] Y. Huang, C. Jiang, K. Jang, H. S. Lee, E. Cho, M. Jayasimhadri, and S.-S. Yi, "Luminescence and microstructure of sm2+ ions reduced by x-ray irradiation in li2o-sro-b2o3 glass," *Journal of Applied Physics*, vol. 103, no. 11, pp. 113519 –113519–7, 2008.

[31] B. Lei, Y. Liu, G. Tang, Z. Ye, and C. Shi, "Spectra and long-lasting properties of sm3+-doped yttrium oxysulfide phosphor," *Materials Chemistry and Physics*, vol. 87, no. 1, pp. 227 – 232, 2004.

[32] P. Nachimuthu, R. Jagannathan, V. N. Kumar, and D. N. Rao, "Absorption and emission spectral studies of sm3+ and dy3+ ions in pbo-pbf2 glasses," *Journal of Non-Crystalline Solids*, vol. 217, pp. 215 – 223, 1997.

[33] C. Qin, Y. Huang, W. Zhao, L. Shi, and H. J. Seo, "Luminescence spectroscopy and crystallographic sites of sm2+ doped in sr6bp5o20," *Materials Chemistry and Physics*, vol. 121, pp. 286 – 290, 2010.

[34] M. Nogami, Y. Abe, K. Hirao, and D. H. Cho, "Room temperature persistent spectra hole burning in sm[sup 2 +]-doped silicate glasses prepared by the sol-gel process," *Applied Physics Letters*, vol. 66, no. 22, pp. 2952–2954, 1995.

[35] Y. Huang, W. Zhao, L. Shi, and H. J. Seo, "Structural defects and luminescence properties of sm2+ ions doped in babpo5 phosphor by x-ray irradiation," *Journal of Alloys and Compounds*, vol. 477, pp. 936 – 940, 2009.

[36] J. Qiu, Y. Shimizugawa, Y. Iwabuchi, and K. Hirao, "Photostimulated luminescence in eu2+ -doped fluoroaluminate glasses," *Applied Physics Letters*, vol. 71, no. 6, pp. 759–761, 1997.

[37] Y. Huang, W. Kai, K. Jang, H. S. Lee, X. Wang, Y. Zhang, D. Qin, and C. Jiang, "The luminescence properties of sm2+ doped sodium barium strontium phosphate," *Materials Letters*, vol. 62, pp. 1913 – 1915, 2008.

[38] J. Lim, M. Lee, and E. Kim, "Three-dimensional optical memory using photoluminescence change in sm-doped sodium borate glass," *Applied Physics Letters*, vol. 86, no. 19, p. 191105, 2005.

[39] E. Malchukova, B. Boizot, G. Petite, and D. Ghaleb, "Optical properties and valence state of sm ions in aluminoborosilicate glass under -irradiation," *Journal of Non-Crystalline Solids*, vol. 353, pp. 2397 – 2402, 2007.

[40] M. Nogami and K. Suzuki, "Formation of sm2+ ions and spectral hole burning in x-ray irradiated glasses," *The Journal of Physical Chemistry B*, vol. 106, no. 21, pp. 5395–5399, 2002.

[41] M. Nogami and K. Suzuki, "Fast spectral hole burning in sm2+-doped al2o3-sio2 glasses," *Advanced Materials*, vol. 14, no. 12, pp. 923–926, 2002.

[42] K. Miura, J. Qiu, S. Fujiwara, S. Sakaguchi, and K. Hirao, "Three-dimensional optical memory with rewriteable and ultrahigh density using the valence-state change of samarium ions," *Applied Physics Letters*, vol. 80, no. 13, pp. 2263–2265, 2002.

[43] D. Maki, T. Ishii, F. Sato, Y. Kato, T. Yamamoto, and T. Iida, "Development of confocal laser microscope system for examination of microscopic characteristics of radiophotoluminescence glass dosemeters," *Radiation Protection Dosimetry*, vol. 144, pp. 222–225, 2011.

[44] W. Qin, K. Jang, S. Park, Y. ill Lee, and C. Kim, "The mechanism of photobleaching in sm2+-doped alkaline-earth fluorohalides," *Journal of Luminescence*, vol. 113, pp. 9 – 16, 2005.

[45] H. Riesen and W. A. Kaczmarek, "Efficient x-ray generation of sm2+ in nanocrystalline bafcl/sm3+: a photoluminescent x-ray storage phosphor," *Inorganic Chemistry*, vol. 46, no. 18, pp. 7235–7237, 2007.

[46] H. Ebendorff-Heidepriem and D. Ehrt, "Effect of tb3+ ions on x-ray-induced

defect formation in phosphate containing glasses," *Optical Materials*, vol. 18, no. 4, pp. 419 – 430, 2002.

[47] D. Ehrt, P. Ebeling, and U. Natura, "Uv transmission and radiation-induced defects in phosphate and fluoride-phosphate glasses," *Journal of Non-Crystalline Solids*, vol. 263&264, pp. 240 – 250, 2000.

[48] P. Ebeling, D. Ehrt, and M. Friedrich, "X-ray induced effects in phosphate glasses," *Optical Materials*, vol. 20, no. 2, pp. 101 – 111, 2002.

[49] D. L. Griscom, E. J. Friebele, K. J. Long, and J. W. Fleming, "Fundamental defect centers in glass: Electron spin resonance and optical absorption studies of irradiated phosphorus-doped silica glass and optical fibers," *Journal of Applied Physics*, vol. 54, no. 7, pp. 3743 –3762, 1983.

[50] D. Möncke and D. Ehrt, "Irradiation induced defects in glasses resulting in the photoionization of polyvalent dopants," *Optical Materials*, vol. 25, no. 4, pp. 425 – 437, 2004.

[51] K. Tanimura, W. A. Sibley, M. Suscavage, and M. Drexhage, "Radiation effects in fluoride glasses," *Journal of Applied Physics*, vol. 58, no. 12, pp. 4544–4552, 1985.

[52] T. V. Bocharova, G. O. Karapetyan, A. M. Mironov, N. O. Tagil'tseva, and V. D. Khalilev, "Specific features of the induced absorption spectra of fluoroaluminate glasses doped with samarium ions," *Glass Physics and Chemistry*, vol. 29, pp. 7–10, 2003.

[53] G. Okada, B. Morrell, C. Koughia, A. Edgar, C. Varoy, G. Belev, T. Wysokinski, D. Chapman, and S. Kasap, "Spatially resolved measurement of high doses in microbeam radiation therapy using samarium doped fluorophosphate glasses," *Applied Physics Letters*, vol. 99, no. 12, p. 121105, 2011.

[54] D. Ehrt and T. Töpfer, "Preparation, structure and properties of yb^{3+} fp laser

glass." Institute of Optics and Quantum Electronics, Max-Wien-Platz 1, D-07743 Jena, Germany.

[55] G. Poludniowski, G. Landry, F. DeBlois, P. M. Evans, and F. Verhaegen, "Spekcalc : a program to calculate photon spectra from tungsten anode x-ray tubes," *Physics in Medicine and Biology*, vol. 54, no. 19, p. N433, 2009.

[56] G. G. Poludniowski and P. M. Evans, "Calculation of x-ray spectra emerging from an x-ray tube. part i. electron penetration characteristics in x-ray targets," *Medical Physics*, vol. 34, no. 6, pp. 2164–2174, 2007.

[57] G. G. Poludniowski, "Calculation of x-ray spectra emerging from an x-ray tube. part ii. x-ray production and filtration in x-ray targets," *Medical Physics*, vol. 34, no. 6, pp. 2175–2186, 2007.

[58] Faxitron X-Ray LLC, 575 Bond St. Lincolnshire, IL 60069, *Faxitron Cabinet X-ray Systems Technical Manual Models 43855C, 43855D, 43855E and 43855F*, rev. 5 ed., May 2009.

[59] D. Chapman, "Biomedical imaging and therapy beamline conceptual design report," tech. rep., Canadian Light Source Inc, January 2005.

[60] D. Chapman, "Shielding estimate for the biomedical imaging and therapy beamline," tech. rep., Canadian Light Source Inc, February 2007.

[61] W. Thomlinson, P. Suortti, and D. Chapman, "Recent advances in synchrotron radiation medical research," *Nuclear Instruments and Methods in Physics Research Section A: Accelerators, Spectrometers, Detectors and Associated Equipment*, vol. 543, no. 1, pp. 288 – 296, 2005.

[62] G. Okada, "Optical properties of rare-earth doped fluorozirconate glass-ceramics for x-ray detector applications," Master's thesis, University of Saskatchewan, 2010.

[63] G. Soundararjan, "Optical characterization of rare earth doped glasses," Master's thesis, University of Saskatchewan, 2009.

[64] PerkinElmer, *Lambda 800/900 User's Guide*, September 2000.

[65] PerkinElmer, *UV WinLab Software User's Guide*, October 2000.

[66] Bruker Instruments EPR Division, Bruker Intruments Inc, 19 Fortune Drive, Manning Park, Billerica, MA, 01821, *EMX EPR Spectrometer*, 2.0 ed., 1998.

[67] I. I. Ezhik, S. I. Berul', and N. M. Kotelevskii, "Investigation of luminescence and esr spectra of samarium and neodymium in sodium metaphosphate," *Russian Physics Journal*, vol. 13, pp. 1665–1667, 1970.

[68] T. Altshuler and M. Bresler, "Jahn-teller effect on sm3+ ions in mixed-valence compound smb6," *Czechoslovak Journal of Physics*, vol. 46, pp. 1985–1986, 1996.

[69] M. Brustolon and E. Giamello, eds., *Electron Paramagnetic Resonance: A Practitioner's Toolkit*. Hoboken, New Jersey: John Wiley & Sons, 2009.

[70] A. Thompson, "X-ray data booklet," Lawerance Berkeley National Laboratory, University of California, Berkeley, CA, October 2009.

[71] C. Nordling and J. Österman, *Physics Handbook for Science and Engineering*. Studentlitteratur, 2006.

[72] C. J. Foot, *Atomic Physics*. Oxford University Press, 2005.